Université Libre de Bruxelles
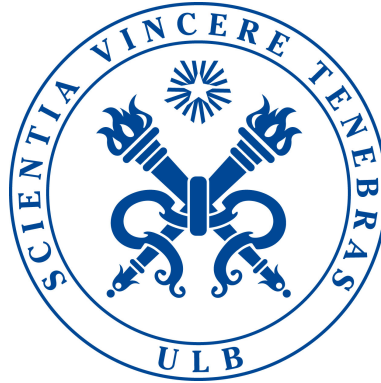
Service de Physique des Particules
Interuniversity Institute for High Energies

The IceCube Neutrino Observatory:
search for extended sources of neutrinos and
preliminary study of a communication protocol
for its future upgrade

Elisa Pinat

Supervisor   Juan Antonio Aguilar Sánchez
Co-supervisor   Kael Hanson

June 2017

PhD thesis jury members:

Juan Antonio AGUILAR SÁNCHEZ (ULB, Supervisor)

Barbara CLERBAUX (ULB, President)

Catherine DE CLERCQ (VUB)

Gilles DE LENTDECKER (ULB, Secretary)

Chad FINLEY (Stockholm University)

Kael HANSON (University of Wisconsin, Co-supervisor)

Juan de Dios ZORNOZA (IFIC, Valencia)

To Valeria Solesin,
Giulio Regeni,
and the best of youth

Abstract

When humans started looking out at a starry night, astronomy was born. Photons emitted by stars travel up to sometimes billions of light years to reach our eyes, and by studying the properties of this photon flux we are able to infer properties of the star itself. Instead of photons, the IceCube Observatory, located at South Pole, aims at detecting neutrinos and hopes to shed some light on the still unsolved mystery of cosmic-ray acceleration and production mechanisms, and on the most energetic phenomena of the Universe.

At the time of this writing, IceCube has proven the existence of an astrophysical neutrino flux with a significance exceeding seven sigmas. Nevertheless, the observed astrophysical neutrino flux shows no significant directional clustering nor a clear association with any known source class so far. Also the latest results given by IceCube's point source analysis show no significant clustering as well. It is therefore important to widen the search to different source topologies to maximize the discovery potential. In the first part of this work we present an extended source analysis with seven years of IceCube data, adding three years of data to the previous published work and implementing a novel likelihood formulation. Since the extensions of any potential sources are not known a priori, five different extensions have been considered, from $1°$ to $5°$. No significant clustering is observed in any of the maps.

The ability of IceCube to establish neutrino astronomy by finding neutrino sources is limited by the number of cosmic neutrinos measured. Despite the aforementioned discovery of an astrophysical flux, detailed spectral studies and searches for specific source locations in this signal remain a challenge with the event sample sizes available from the IceCube instrument. Therefore, a considerable expansion of the current detector, IceCube Gen2, is promoted, which includes the instrumentation of a 10 km^3 volume, able to deliver substantial increases in the astrophysical neutrino sample for all flavors. Not only the hardware will be upgraded, but many systems will undergo improvements, such as communications and timing infrastructures. A new communication system has been investigated and is presented in the second part of this document. Binary Phase Shift Keying (BPSK), the simplest digital modulation technique, has been studied as possible communication technique for IceCube Gen2.

Résumé

Quand les humains ont commencé à regarder le ciel étoilé, l'astronomie est née. Les photons émis par les étoiles voyagent parfois des milliards d'années lumière avant d'atteindre nos yeux, et c'est grâce à l'étude de ce flux de photons que l'on peut déduire les propriétés des étoiles mêmes. Au lieu des photons, l'Observatoire IceCube, situé au Pôle Sud, a pour but de détecter des neutrinos : il espère éclairer le mystère encore non résolu de l'accélération et des mécanismes de production des rayons cosmiques, ainsi que des phénomènes les plus énergétiques de l'Univers.

Au moment où ce document a été rédigé, IceCube a démontré l'existence d'un flux de neutrinos astrophysiques avec une signification statistique excédant sept sigmas. Cependant, le flux de neutrinos astrophysiques observé ne montre aucun regroupement directionnel significatif ni une évidence d'association avec aucune source connue à l'heure actuelle. De plus, les derniers résultats fournis par les analyses de sources ponctuelles de la collaboration IceCube ne montrent non plus aucun regroupement. Il est donc important d'étendre ces recherches vers des typologies de sources différentes pour maximiser le potentiel de son découverte. Dans la première partie de ce travail nous présentons une analyse de source étendue basée sur sept années de données d'IceCube, ce qui rajoute trois ans de données au travail précédemment publié tout en mettant en oeuvre une nouvelle formulation de maximum de vraisemblance. Comme les extensions de sources potentielles ne sont pas connues à priori, cinq extensions différentes ont été considérées, de $1°$ à $5°$. Aucun regroupement significatif n'a été observé sur aucune des cartes.

La capacité d'IceCube de consolider l'astronomie neutrino en découvrant des sources de neutrinos est limitée par le nombre de neutrinos cosmiques mesuré. Malgré la découverte susmentionnée d'un flux astrophysique, les études détaillées de spectre ainsi que les recherches de sources spécifiques pour ce type de signal demeurent un défi, à cause de la limitation de taille disponible des échantillons avec l'instrument IceCube. Par conséquent, une expansion considérable du détecteur actuel, IceCube Gen2, est promue : elle inclut l'instrumentation d'un volume de 10 km^3, apte à fournir une augmentation importante des échantillons de neutrinos de toutes les saveurs. Non seulement le hardware sera mis à niveau, mais de nombreux autres systèmes subiront des améliorations, comme les infrastructures de communication et de timing. Un nouveau système de communication a été étudié et est présenté dans la deuxième partie de ce document. Le Binary Phase Shift Keying (BPSK), la technique de modulation numérique la plus simple, a été étudiée comme technique potentielle pour IceCube Gen2.

Contents

About this Thesis

This thesis is divided into three parts. The aim of the first part is to give an overview of the multi-messenger high-energy astrophysics, as well as a short history of neutrino telescopes. We also present the principles of neutrino interactions and the IceCube Neutrino Observatory. In Chapter 1 we introduce Cosmic Rays and their connection with gamma rays and neutrinos, underlying how powerful neutrinos are as astrophysical messengers. Combining information from these different messengers should help solving the long-lasting mystery of cosmic ray production and acceleration. Indeed, after more than 100 years, the origin of cosmic rays is still an unresolved question. We review the possible neutrino sources, presenting the latest results from gamma-ray and neutrino astronomy. We limit ourselves to neutrino fluxes that are related to the cosmic-ray spectrum, neglecting exotic physics as magnetic monopoles or dark matter annihilation. Finally, we present possible candidates with a spatial extension, and extended sources seen in the γ-sky and cosmic-ray sky that are relevant for this thesis. Chapter 2 continues with a description of the principles of neutrino interactions: we describe the fundamental interactions and the typical signatures these leave in the IceCube detector. We briefly present the effect the detector is based on, that is the Cherenkov effect. At the end of the chapter we introduce for the first time the backgrounds of the analysis. Their important role is described more in detail later in the text, in the second part. Chapter 3 is instead dedicated to a detailed description of the IceCube detector, and to a short description of the offline processing tools used to reconstruct particle directions and energies, which represent the two most important variables for the analysis.

The second part of this work is dedicated to the main analysis conducted during this PhD: the search for extended sources with 7 years IceCube through-going muon data. In Chapter 4 we recall what are the motivations that support a dedicated search for extended sources of neutrinos, and we present the point source samples used in this analysis, from IC40 to IC86-IV, highlighting important properties as angular resolution and effective area. Few words are spent on simulation. A thorough description of the analysis method used is given in Chapter 6. The likelihood method is introduced, together with the probability density functions for signal and background. The modifications to the standard point source method are presented: the extension of a possible neutrino source enters as a parameter in the spatial part of

the signal probability density function. Because the extensions are not always known *a priori*, five different extensions have been considered, from $1°$ to $5°$. Moreover, the likelihood method has been improved by accounting for signal contamination in the background estimation. The results of the analysis are presented in Chapter 7: five different skymaps, one for each extension considered, have been produced, to test whether data are better described by a background-only hypothesis or by a mixture of signal plus background. All the five maps are consistent with the background-only hypothesis.

The third part is dedicated to the feasibility study of a new communication system for the IceCube-Gen2 upgrade. With the discovery of a high-energy astrophysical neutrino flux, IceCube has fulfilled one if its major scientific goals, but the size of the sample, limited to roughly a hundred events, is not sufficient to find any significant directional point source clustering, nor a clear association with any know astrophysical source. IceCube-Gen2, a considerable expansion of the current detector, would be able to deliver substantial increase in the astrophysical neutrino sample for all flavors. The upgrade would need not only new hardware to be deployed in ice, but also an overhaul of the communication system. In Chapter 8 we give an overview of the current baseline of the IceCube-Gen2 detector, presenting all the sub-detectors in the facility. The aim of Chapter 9 is to give a brief overview of the current communication scheme adopted in IceCube, describing the entities involved in the communication, the cable system and the protocol. Finally, in Chapter 10, a preliminary study on the simplest form of digital modulation (Binary Phase Shift Keying) is presented. This simulation only study aims to prove the feasibility of the protocol as possible signaling method for IceCube-Gen2.

Author's contribution

The work done over this PhD has been performed here in Brussels at the IIHE, Interuniversity Institute for High Energies (ULB-VUB), under the supervision of my mentors, Juan Antonio Aguilar Sánchez and Kael Hanson, and has been carried out within the IceCube collaboration, consisting of hundreds of skilled people. This makes a major part of my achievements the result of a teamwork. Since I joined the collaboration in 2013, I've originally contributed with:

- Extended Sources analysis with 7 years of data and implementation of the extended source code using a novel signal-subtracted likelihood applied to extended regions.
- Binary Phase Shift Keying simulations, PCB design and construction of a filter board to reproduce the IceCube filter box, presented in [1].

- Studies on triggers and bug fix for the Furthermore DAQ release (not described in this work but presented in [2]).
- Quadrature Amplitude Modulation techniques study, and first attempts of firmware implementation for FPGA (not described in this work).

Part I

Cosmic Rays, Neutrinos and IceCube

Overview of Part I

The first part of this work introduces high-energy neutrino and multi-messenger astronomy, presents the underlying physics of neutrino interactions in the ice and the IceCube detector. In the first chapter, after a short historical overview on neutrino telescopes, we present the connection between neutrinos, cosmic rays and gamma rays. In 2013 IceCube has announced the detection of an high-energy astrophysical neutrino flux, marking the onset of neutrino astronomy: by studying these events we hope to shed some light on the unsolved mechanisms of cosmic ray production and acceleration. Potential neutrino sources are introduced, and recent results from gamma-ray and neutrino telescope are presented. In the second chapter we describe the fundamental interactions and the typical signatures neutrino events leave in the IceCube detector. We present the Cherenkov effect, and the backgrounds of the analysis which will be described in more detail later in the text. We dedicate the third chapter to a detailed description of the IceCube detector, and to a short overview of the offline processing tools used later in the analysis to reconstruct particle directions and energies.

Multi-messenger High-Energy Astrophysics

During the 20th century, astronomy has undergone a major revolution: from the traditional observations based on optical photons we have progressively moved to a multi-wavelength astronomy, where multiple parts of the spectrum are used. And every time we have looked at our Universe in a different way, we have discovered something that was not expected and that revolutionized our understanding: Gamma-Ray Bursts were discovered by looking at possible thermonuclear explosions emitting gamma rays, while pulsars and the Cosmic Microwave Background (CMB) were discovered using radio and micro waves.

Exciting times are ahead of us: in 2013, the IceCube collaboration has announced the detection of an astrophysical neutrino flux [3], whose significance exceeds nowadays seven sigmas. Neutrinos are ideal messengers, and their use in astronomy was imagined already in the 1960s [4]: stars, Active Galactic Nuclei (AGNs) and astrophysical engines are opaque to photons, while neutrinos can easily escape, carrying information from the most dense regions of the Universe. Interaction with the Cosmic Microwave Background imposes strong limits on the propagation of high energy photons, protons, and nuclei, while neutrinos allow us to look farther back in space, almost until the edge of the Universe. These properties make neutrinos great astrophysical messengers but have an important drawback: cosmic neutrinos are very difficult to detect, and require immense particle detectors to collect statistically significant event numbers.

While we are waiting to overcome these difficulties by constructing even bigger detectors, like the IceCube Gen2 facility [5], coincident experiments with earth- and space-based gamma-ray observatories, cosmic-ray observatories and now also gravitational wave detectors are constantly trying to push the frontiers of astronomy a bit further. The hope is to finally solve the mystery of cosmic ray production and acceleration more than 100 years after their discovery. The *multi-messenger approach* is not only a tool to extend the understanding of an object by combining information from different probes, but also to increase the statistical significance of an observation by coincident detection and the use of time-correlation. If this represents the most effective way to obtain a complete knowledge of astrophysical sources and their emission engines, providing complementary insight into the physics

of the progenitors and their environment, neutrinos remain however the exclusive messenger unambiguously associated to weak decay of hadrons.

1.1 Brief history of neutrino telescopes

In December 1930, Pauli introduced the concept of neutrino (originally called neutron) as "a desperate remedy" to explain the observed continuous spectrum of electrons in beta decay, until then thought to be a two body decay: *The continuous beta spectrum would then make sense with the assumption that in beta decay, in addition to the electron, a neutron is emitted such that the sum of the energies of neutron and electron is constant.*". When the actual neutron was discovered by Chadwick in 1932, Fermi proposed to call Pauli's neutral particle *neutrino*: little neutral one. About twenty years were needed to prove the existence of this particle. It was 1956 when Cowan and Reines [6] performed their experiment using a reactor as source of neutrinos and measured the neutrino cross section for the first time, results that earned Reines the Nobel prize in 1995.

While the interest of probing the Sun interior and its nuclear reactions with neutrinos was growing, in 1960 Kenneth Greisen proposed to build a 3000 tons underground neutrino detector to observe the Crab Nebula. Despite admitting that the rate of cosmic neutrino events would have been low, he was optimistic that "neutrino detection will become one of the tools of both physics and astronomy" [7]. Later on, the soviet physicist Markov proposed "to install detectors deep in a lake or in the sea to determine the direction of charged particles with the help of Cherenkov radiation" [4]. In the same article another key feature of neutrino telescopes is described, i.e. using the Earth as a shield to isolate the neutrinos from cosmic-ray backgrounds since "all known particles with the exception of neutrinos are absorbed by scores of kilometers of the substance and thus are entirely screened by the planet". The last missing piece came some years later, when it became clear that to collect a statistically significant number of events cubic kilometers detectors were needed. Given the detector's required size, early efforts concentrated on transforming large volumes of natural water into Cherenkov detectors.

The Deep Underwater Muon and Neutrino Detector (DUMAND) has been the first and heroic tentative to construct such a detector at 4800 m depth in the Pacific Ocean off the Big Island of Hawaii. The same Frederick Reines of the 1956 experiment was one of the physicists who conceived and named the DUMAND experiment. The project started informally in 1973, intentionally dedicated to the study of cosmic rays it was only afterwards converted into a neutrino detector. The ambitious early design was to instrument a volume of 1.22 km^3 with $20\,000$ photomultipliers, arranged in

1261 strings. After twenty years and multiple changes in the detector geometry and configuration, in December 1993 the first string of the DUMAND detector was finally deployed successfully. Unfortunately the detector broke down after only 10 hours of operation, due to a leak in one of the electrical connectors that caused a short circuit. The string was successfully recovered one month later, but in mid 1996 the US Department of Energy terminated further support.

Despite its tragic end, DUMAND is considered a pioneer for many of the technologies in use today, and inspired the deployment of underwater neutrino telescopes such as the Lake Baikal detector in Siberia [8] and the neutrino telescope ANTARES in the Mediterranean. Though having a smaller scale than the proposed DUMAND one, the ANTARES telescope, completed in 2008, finally proves that such an underwater instrument is now within technological reach. The detector, located 40 km offshore of Toulon, in the south of France, at 2475 m depth, consists of an octagonal array of 12 lines (also called strings) separated by a distance of ∼ 74 m. These lines are anchored to the seabed and maintained vertical by buoys. Each line has 25 *storeys* holding a triplet of photomultiplier tubes (PMTs) [9]. Since the deployment of the first line in 2006, data taking has proceeded essentially continuously. Thanks to its location and to the excellent angular resolution, it extends the reach of neutrino astronomy in a complementary region of the Universe to the South Pole experiments, in particular the central region of the local galaxy, yielding diffuse neutrino flux sensitivity and the best limits in the world for many galactic sources in the southern hemisphere. More competitive results are expected in the future as ANTARES will continue taking data at least until the end of 2017, when it will give way to the next-generation detector KM3NeT.

Current Mediterranean efforts in the neutrino research field are that three experiments, ANTARES [10], NEMO [11] and NESTOR [12] are joining their efforts to participate in the KM3NeT project. KM3NeT, which was awarded a 3.8 M grant in the context of the Horizon2020 European programme, will be a pan-European facility with three deployment sites each dedicated to a targeted area of research, in Italy, France and Greece. KM3NeT Phase 1 has been already funded with 31 millions, and in 2012, the first phase of the implementation of the KM3NeT research facility started with the construction of the seabed infrastructure at the KM3NeT-Fr and KM3NeT-It sites. ARCA (Astroparticle Research with Cosmics in the Abyss) will be built at the Capo Passero site in Sicily, and while ORCA (Oscillation Research with Cosmics in the Abyss) will be constructed at the Toulon site in France. The ultimate goal is to fully develop the KM3NeT research infrastructure to comprise a distributed installation at the three foreseen sites including the one off the coast of Pylos, Greece, and operate it for ten years or more.

The first telescope on the scale envisaged by the DUMAND collaboration was realized instead by transforming a large volume of another extremely transparent, natural medium: ice. The 3 km-thick Antarctic ice sheet below the Amundsen-Scott South Pole Station was chosen as location for the Antarctic Muon and Neutrino Detector Array (AMANDA). In the Austral summer 93-94, the AMANDA A detector of 80 optical modules (OMs) was deployed on 4 strings positioned between 810 m and 1000 m. A deeper and redesigned array, AMANDA B or AMANDA-II, in operation from 1996 to 2009, represented a proof of concept for the kilometer-scale IceCube neutrino observatory. The AMANDA B detector was deployed in four South Pole campaigns between November 1995 and February 2000, and took data in different configurations, with 4 (year 1996), 10 (year 1997) and 13 strings (year 1998). The final detector configuration completed in 2000, AMANDA-II, consisted of 677 OMs arranged on 19 vertical strings deployed at depths between 1300 to 2400 meters. The used instrumented volume ranged between 1500 to 2000 meters in depth, and covered a cylinder of 200 meters diameter [13]. The science performed with AMANDA-II ranged from the study of a diffuse neutrino flux, point sources and exotic physics such as dark matter and monopoles in the northern hemisphere. IceCube, the successor of the AMANDA detector and subject of this work, will be thoroughly described in the following Chapters.

1.2 Multi-messenger Astrophysics

On September 14, 2015, the first observations of gravitational waves (GW) from the merging of a binary black-hole system by the LIGO interferometers marked the onset of gravitational-wave astronomy [14]. Despite being far from using gravitational waves as exclusive messenger in astronomy, this event highlights the importance of the so-called multi-messenger approach, adding a new fundamental messenger to explore the Universe and probe its most energetic events. Combining the information coming from high-energy photons, neutrinos, charged cosmic-ray particles and now also from gravitational waves promises to help solve the still unanswered questions on cosmic-ray sources and acceleration mechanisms. The multi-messenger approach is depicted in Figure 1.1. Multi-messenger searches can be summarized in three main approaches:

- the use of information of one messenger detection or candidate in the data analysis of another messenger to improve its search;
- the search for coincidence or correlation among separate lists of candidate events from different messengers to increase their significance or to identify common astrophysical sources; the combined sensitivity can also be enhanced
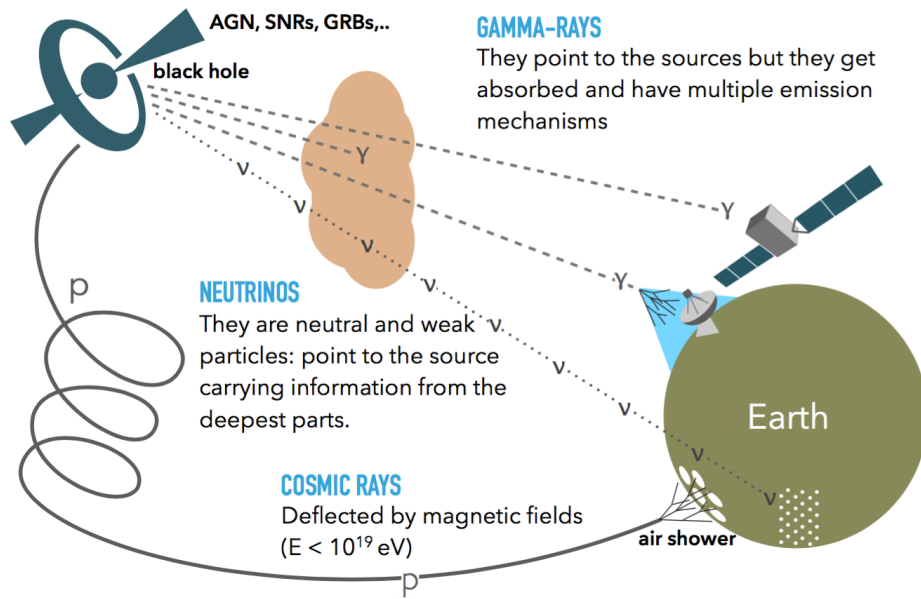
Fig. 1.1.: Diagram of multi-messenger astronomy. Sources can emit cosmic rays (CRs), photons and neutrinos (gravitational waves are not included). Cosmic rays are deflected by magnetic fields before reaching Earth and being observed by air shower arrays. High energy photons are detected by space- and ground-based telescopes, but can be absorbed by dust or low-energy background photons. Neutrinos travel straight from the source to Earth without absorption (Image credit: J.A. Aguilar Sánchez).

by searching for coincidences in the sub-threshold data streams for multiple messengers;

- the use of GW/neutrino candidates to set up observational strategies to point electromagnetic (EM) observatories and search for the EM signatures of the astrophysical sources (follow-ups).

Neutrinos play an important role in this emerging field. IceCube takes part in the global effort by using a Real Time Alert System. Several analyses selecting neutrinos of astrophysical origin are operating in realtime in Antarctica, producing alerts to enable rapid follow-up observations. The goal of these observations is to locate the astrophysical objects responsible for these neutrino signals [15]. IceCube is also part of the Astrophysical Multimessenger Observatory Network (AMON), a program currently under development at The Pennsylvania State University [16]. AMON seeks to perform a real-time correlation analysis of the high-energy signals across all the so-far known astronomical messengers photons, neutrinos, cosmic rays, and gravitational waves. Among other members of the AMON Network we find ANTARES, The Pierre Auger Observatory, one of the largest operating ground-based cosmic-ray detector, Fermi, a space-based satellite dedicated to the study of GeV photons, High Altitude Water Cherenkov (HAWC) designed to observe gamma rays and cosmic rays between 100 GeV and 100 TeV, and the Laser Interferometer Gravitational-Wave Observatory (LIGO).

Before focusing on neutrinos and describe the possible sources we expect them from, we will give a short overview of the two other most important messengers in astronomy, cosmic and gamma rays.

1.2.1 Cosmic Rays

In 1912 Victor Hess performed a series of high-altitude balloon flights that lead to the discovery of ionizing radiation coming from space [17]. These particles, restlessly hitting the earth, were known as *cosmic rays*, and their existence was discussed rather contentiously at that time. It was only with the results of Kolhörster's high balloon flights in 1913 and 1914 that finally Hess' results were confirmed [18]. However, only Hess received the Nobel prize in Physics in 1936 for this discovery, and this missed prize might be one of the reasons that makes Kolhörster comparatively unknown to the broader physics community. Since then, hundreds of experiments have studied the subject of cosmic rays intensively, measuring their energy spectrum over many orders of magnitude. These efforts are summarized in Figure 1.2 and, among many achievements, have allowed us to conclude that cosmic rays are atomic nuclei, their flux is almost isotropic and their spectrum is close to being a power law over a vast range in energies, from 10^9 to 10^{20} eV. Generally there are two ways to detect and measure cosmic rays. The first one is the direct detection method, usually obtained from balloon or satellite experiments by raising them above the height where cosmic rays first interact with the atmosphere. The advantage is that one measures the cosmic rays directly, giving immediate information about their composition and energy. On the other hand, the disadvantage is the limited energy range this can be done for. The energy limit for direct detection is up to a few 10^{14} eV, since at higher energies the cosmic-ray flux drops significantly and the low flux becomes the main obstacle to overcome [20]. The AMS-02 [21] and PAMELA [22] spectrometers are two such experiments. The required collecting areas become so large that indirect detection must be used in order to obtain a useful number of events, penalising the individual event knowledge. The indirect measurements are obtained from observing the particle cascades, or the so-called air showers created by cosmic-ray interactions in our atmosphere. After the detection of a representative part of the shower, one can try to infer the properties of the primary cosmic-ray particle. Since it is hard to measure the air shower in detail, inferring the properties of cosmic rays via indirect techniques is challenging. The Pierre Auger Observatory [23] and the Telescope Array [24] are currently the largest operating ground based cosmic-ray experiments. Given their size, these experiments are often referred to as Extensive Air Showers Arrays (EAS).

The most prominent features of the CR energy spectrum fall into the energy range covered by EAS experiments. The first one, known as the *knee* at an energy of about
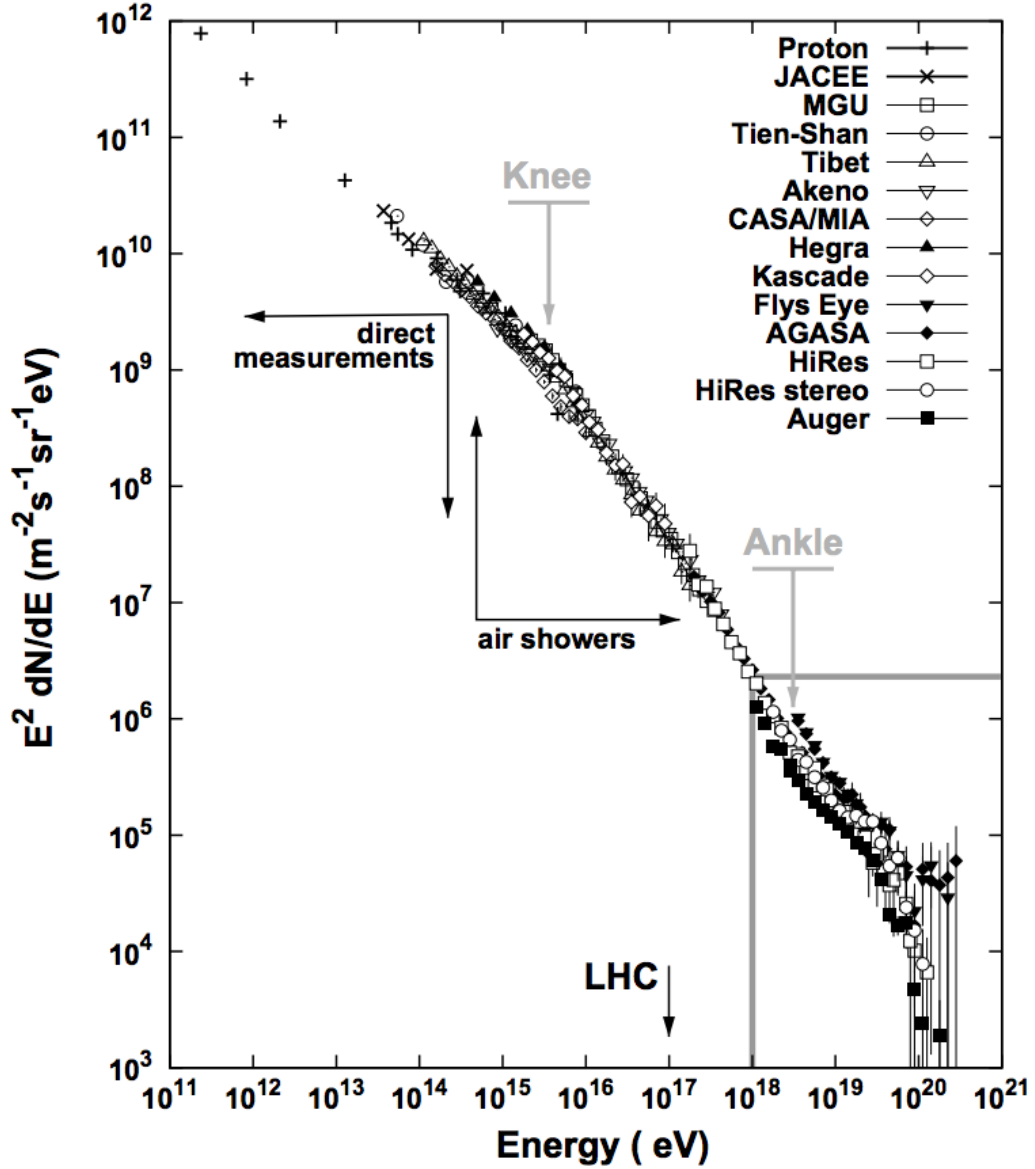
Fig. 1.2.: Differential energy spectrum of cosmic rays with energies above 10^{11} eV multiplied by E^2. The position of the cosmic-ray knee and ankle is indicated by gray arrows. The equivalent laboratory energy of the Large Hadron Collider is also shown [19].

$\sim 3 \times 10^{15}$ eV and the second one, the *ankle*, at $\sim 10^{18}$ eV are visible as changes in the power law index (Figure 1.2). Below the knee the flux of cosmic rays can be described by a spectral index of $\gamma \sim 2.7$. Above the knee the spectrum steepens to a spectral index of $\gamma \approx 3$ and above the ankle the spectrum hardens again. The cosmic-ray spectrum spans not only many orders of magnitude in energy but its flux varies as well over more than thirty orders of magnitude, from one particle per m^2 per second at 100 GeV to one particle per m^2 per year in the knee region, and further down to a very low flux of one particle per km^2 per year at the ankle. In terms of composition, H and He form respectively 85% and 12% of all CRs, with contributions from heavier elements only at about $\sim 3\%$ [19]. These percentages however are strongly energy dependent, and this global picture is dominated by the low energy component.

The knee is commonly understood as marking the limiting energy of galactic proton accelerators and/or the onset of increasing outflow of particles from the Galaxy. Hence, either the cosmic-ray sources are running out of steam, or the galactic magnetic field is not strong enough to contain the particles and the probability of their arrival on earth becomes smaller. The current state of knowledge assumes that charged particles are accelerated in strong turbulent magnetic fields by a stochastic and iterative process. Magnetic fields keep particles within a confined region, which enables charged particles to run through the acceleration process multiple times and reach very high energies. The confinement region is constrained by the gyroradius of the accelerated particles. As the energy of the particle increases, so does the gyroradius, becoming so large that eventually particles escape from the acceleration site and do not gain energy anymore. At energies above the knee the gyroradius of the proton becomes larger than the size of the Galaxy, creating a softer spectrum because higher energy particles are more likely to escape [25]. Focusing on the required power, the dominant acceleration sites of CRs at the knee region are generally believed to be shocks associated with supernova remnants (SNR). In-depth examinations suggest that this process is however limited to $E_{max} \sim Z \times 10^{14}$ eV [26] for standard galactic SNRs. More recent estimates give a maximum energy up to one order of magnitude larger for some types of supernovae $E_{max} \sim Z \times 5 \times 10^{15}$ eV [27].

It is generally accepted that the ankle represents the transition to particles from extra-galactic sources [28]. The Larmor radius of a proton of 10^{20} eV in the galactic magnetic field is ≈ 36 kpc, almost comparable to the diameter of the Galaxy. This emphasizes that such high-energy particles are of extragalactic origin. The transition region from galactic to extragalactic CRs is of particular interest. Before encountering the hardening of the spectrum of the ankle feature in the decade belonging to the ultra-high energy regime (UHE), which is $E > 10^{18}$ eV, a softening of the spectrum is seen at $\sim 4 \times 10^{17}$ eV, feature called the *second knee*: the dependence of the

maximal energy to the atomic number leads to consecutive cut-offs of the energy spectra for individual elements proportional to their charge Z, starting with the proton component, responsible therefore of the knee feature. Heavier nuclei are thus responsible for the further cut-offs in the spectrum, up to the iron knee, at $\sim 4 \times 10^{17}$ eV [29]. The origin of CRs above the ankle is generally considered to be of extragalactic nature because of the large scales and magnetic fields required to accelerate and confine charged particles above 10^{18} eV. The need of an extra, higher energy galactic component to fill the gap between the population accelerated by SNRs and the onset of the extragalactic population has been widely discussed [30], but the portion of the spectrum between the second knee and the ankle is still somehow uncharted territory and subject of debate.

The Auger Observatory has established unambiguously the suppression of the cosmic-ray flux at E$\sim 4 \times 10^{19}$ eV [31], confirming the first observation made by HiRes [32] and the Telescope Array results [33]. Despite its origin still being mysterious, this cutoff may be the evidence of the suppression predicted by Greisen, Zatsepin and Kuz'min in 1966 [34, 35]. Cosmic rays lose part of their energy interacting with the CMB photons:

$$p + \gamma_{CMB} \to \Delta^+ \to p + \pi^0, n + \pi^+ \,. \qquad (1.1)$$

The proton loses about 20% of its energy in the process, limiting its travel distance to ~50 Mpc, the so called GZK horizon. The presence of a suppression in the cosmic-ray flux does however not imply that the GZK process exists, and the *disappointing model*, aimed at explaining the Auger detector observational data, offers an alternative scenario where the suppression is due to the maximal energy reached in the acceleration sites [36]. TA and Auger results are compared in Figure 1.3. The energy spectra of the two observatories clearly exhibit the ankle at $\sim 5 \times 10^{18}$ eV and a flux suppression above $\sim 4 \times 10^{19}$ eV. For TA, the flux suppression at the highest energies is in accordance with the energy loss processes of the GZK-effect (solid blue curve). In the case of Auger, however, the suppression starts at lower energies, and this region of the spectrum can be described by assuming pure iron emission from the sources (solid black line). In this case the ankle would require another component of cosmic rays to contribute to the flux at lower energies (dotted black line). Models like the *disappointing model* foresee that the flux suppression is primarily caused by the limiting acceleration energy at the sources rather than by the GZK-effect. This interpretation leads to an increasingly heavier composition towards the suppression region (solid colored lines).

The different interpretations of the Auger and TA energy spectra demonstrate the ambiguity left and underline the importance of understanding the absolute cosmic-ray energy scales to a high level of precision [37]. The detection of cosmogenic neutrinos and photons of very high energy, guaranteed from Equation 1.1, would
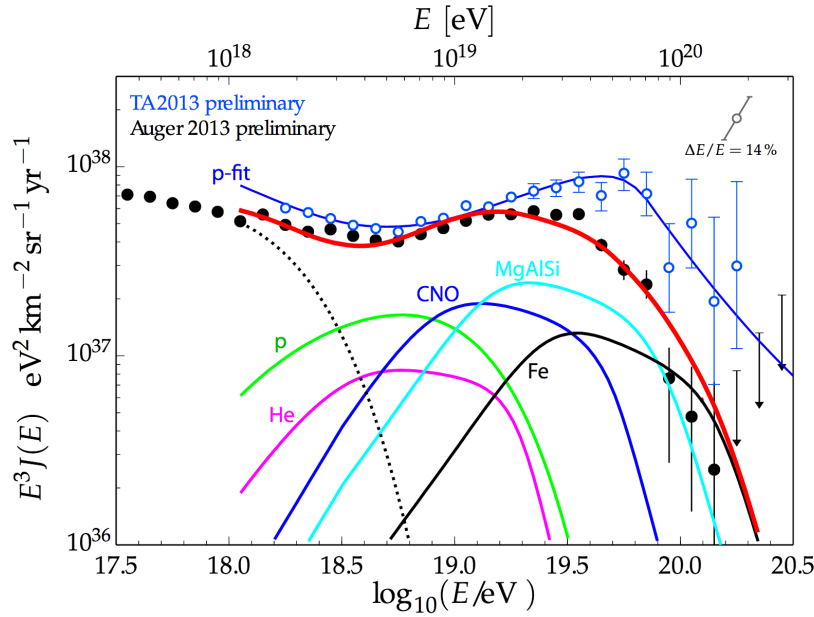
Fig. 1.3.: Measurements of the flux of CRs at the highest energies by the Auger and TA collaboration [37].

help shed some light both on the sources capable to accelerate cosmic rays, on their composition and on the existence of the GZK process itself. If however the *disappointing model* would turn out to be true, no very-high-energy neutrinos are expected in this case [36]. IceCube searches for cosmogenic neutrinos have been so far fruitless [38], and the origin of the flux suppression remains one of the most important open questions of cosmic-ray physics.

Origin of Cosmic Rays

After more than 100 years of research, the source and origin of the highest-energy cosmic rays remain one of the most challenging open questions in astrophysics: only for particles of kinetic energy below 100 MeV we are sure that they have to come from the Sun. For higher energies, conventional models used to explain how particles are accelerated are dubbed bottom-up scenarios. These scenarios assume that the energetic cosmic-ray protons and nuclei are accelerated within regions of intense magnetic fields [39]. The mechanism responsible for the particle acceleration is widely assumed to be the Fermi Mechanism [40]. Fermi acceleration happens in shock environments, which are known to occur in violent phenomena such as supernovae. By continuously crossing the shock, particles are capable of reaching very high energies in a reasonable amount of time. The proof of concept was given by the Earth's bow shock studies performed by the AMPTE spacecraft in the early '90s. The shock, given by the collision of the solar wind with the Earth's magnetic
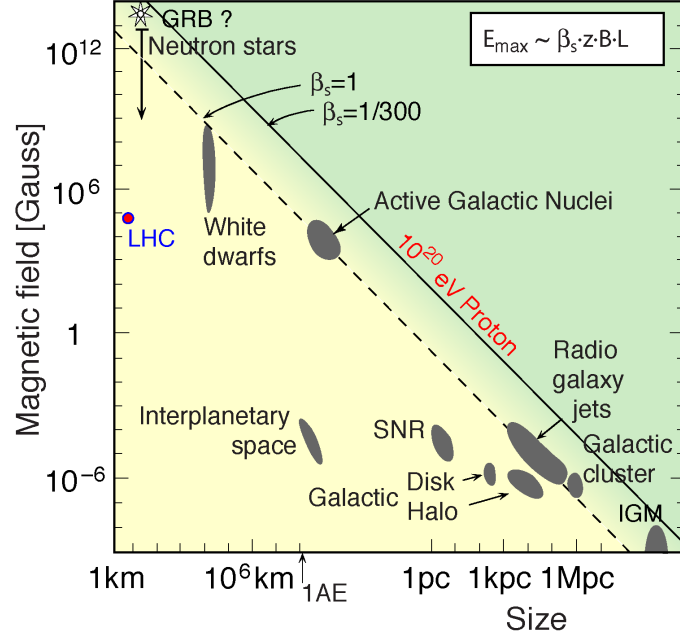
Fig. 1.4.: In 1984 Hillas did a back-of-an-envelope assumption that in order for it to accelerate CR particles to high energies, the size of the acceleration region must be at least twice the gyroradius. Objects below the solid diagonal line cannot accelerate protons to 10^{20} eV. Figure revisited from [41].

field, is accompanied by highly energetic particles. This acceleration process is a very appealing scheme for the origin of CRs, since it explains the power law behavior in the CR spectrum. Independently of the acceleration mechanism, whenever a particle escapes an acceleration site, it will stop gaining energy, imposing a limit on its maximum energy. The maximum energy attainable, E_{max}, for a particle of charge Ze accelerated by a magnetic field B in an object of size R can be expressed as:

$$E_{max} = k\beta Ze \left(\frac{B}{\mu G}\right)\left(\frac{R}{kpc}\right) \text{EeV} \qquad (1.2)$$

where β is the shock speed in units of c and $k < 1$ the efficiency of the process. This geometrical criterion is known as the Hillas criterion. It relates the maximum energy of accelerated particles to the size and magnetic field of the acceleration site, both observationally accessible. The different astrophysical objects that satisfy this condition are represented in the so called Hillas plot, shown in Figure 1.4. While there is no guarantee that the particles are able to reach the maximum energy, nor that the source can generate enough particles to explain all cosmic rays, the Hillas plot helps to easily rule out certain sources as viable candidates: it leaves only AGNs, Gamma-Ray Bursts, neutron stars and radio galaxies as candidates for UHECRs acceleration.

Low Energy, LE	MeV range	0.1 - 100 MeV
High Energy, HE	GeV range	0.1 - 100 GeV
Very High Energy, VHE	TeV range	0.1 - 100 TeV
Ultra High Energy, UHE	PeV range	0.1 - 100 PeV
Extremely High Energy, EHE	EeV range	0.1 - 100 EeV

Tab. 1.1.: The conventional energy windows of gamma-ray astronomy.

1.2.2 Gamma Rays

The principal reason why CRs fail to reveal the origin of the particles is undoubtedly that their directions have been scrambled by galactic magnetic fields. At EeV energies "proton astronomy" may however be possible because the arrival directions of electrically charged cosmic rays are no longer scrambled by the ambient magnetic field of our own galaxy [42]. Deflections are charge and energy dependent and typical values for protons with energy above 40 EeV are $\leq 1°$ [43]. Photons on the contrary, being stable and electrically neutral, have many advantages as cosmic messengers: they can point back to their source, they are easy to detect over a wide energy range since they easily interact electromagnetically with charged particles, and their spectrum carries detailed information about the chemical and physical properties of the source. Astronomy conventionally divides the wide energy range of photons, which spans more than 15 decades in energy, into several windows, listed on Table 1.1. Open windows are in the MeV, GeV and TeV bands: the LE and HE ones are domain of space-based astronomy, while the VHE and above are domain of ground-based astronomy. Spectral and morphological γ-ray studies are conducted in the GeV range with the Large Area Telescope [44] on board the Fermi gamma-ray satellite, and in the TeV range using ground-based Imaging Air Cherenkov Telescopes (IACTs) such as VERITAS [45], H.E.S.S. [46], or MAGIC [47]. Although gamma-ray astronomy has provided very exciting results, it has some limitations: the hot, dense and dusty regions which from the central engines of stars, active galactic nuclei and other astrophysical energy sources are however completely opaque to photons, and therefore cannot be directly investigated using this messenger. At last, Figure 1.5 shows the mean free path traveled by photons as a function of the energy. During their propagation, VHE photons interact with background photons producing electron-positron pairs. This is the main source of opacity of the Universe, and it occurs whenever the corresponding photon mean free path is smaller, or of the order, of the source distance. For photon energies 10^{10} eV $\leq E_\gamma \leq 10^{14}$ eV the Extragalactic Background Light (EBL) in the infrared wavelength range, represents the main opacity source. For 10^{14} eV $\leq E_\gamma \leq 10^{19}$ eV the interaction with the CMB is
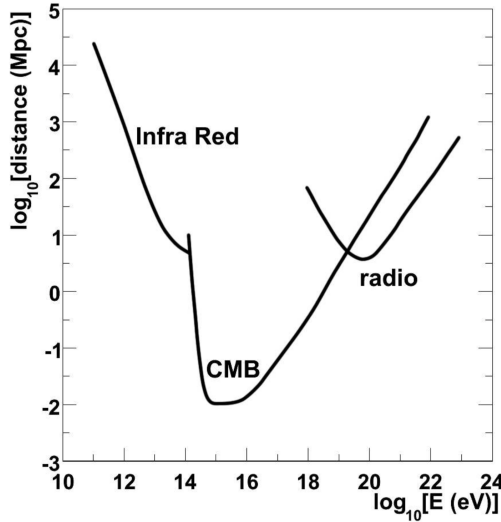
Fig. 1.5.: Mean free paths photons as a function of their energy. During their propagation, VHE photons interact with background photons producing electron-positron pairs. This is the main source of opacity of the Universe, and it occurs whenever the corresponding photon mean free path is smaller, or of the order, of the source distance. As a reference, the galactic center is located at $\log_{10}[\text{distance(Mpc)}] = -2$ [48].

the main dominant contribution, while for $E_\gamma \geq 10^{19}$ eV the radio background plays the leading role [48]. As a reference, in Figure 1.5 the Galactic Center is located at $\log_{10}[\text{distance(Mpc)}] = -2$. Therefore, when photons above 100 TeV are detected at earth, they must have been produced within 10 kpc from the Earth.

The main challenge to interpret gamma-ray observation is that γ-rays can be accelerated both in leptonic and hadronic scenarios. In the leptonic scenario, the acceleration of photons is based on the inverse Compton (IC) effect. IC γ-rays are produced in the interactions of energetic particles with the ambient background fields, the CMB and the diffuse Galactic light. When high-energy hadrons interact with matter or photons near the source, charged and neutral pions are produced. In the case of neutral pions, they generally decay before interacting, producing gamma rays. By studying the spectral characteristics of the gamma-ray emission from known sources it might be possible to determine if pion decays (and hence, hadron acceleration) is taking place at the source, but determining whether the observed γ-rays are associated with a leptonic, hadronic or mixed hadro-leptonic production mechanism is still unresolved for most of the sources detected. In 2013 the Fermi LAT collaboration has found a compelling evidence for hadronic interactions using gamma rays at 100 MeV from only two supernova remnants interacting with molecular clouds [49]. Proton-proton, or more generally nuclear-nuclear collisions create π^0 mesons which usually quickly decay into two gamma rays, each having an energy of $m_{\pi^0}c^2/2 = 67.5$ MeV in the rest frame of the pion (where m_{π^0} is the pion rest mass and c is the speed of light). The resulting gamma-ray number spectrum,
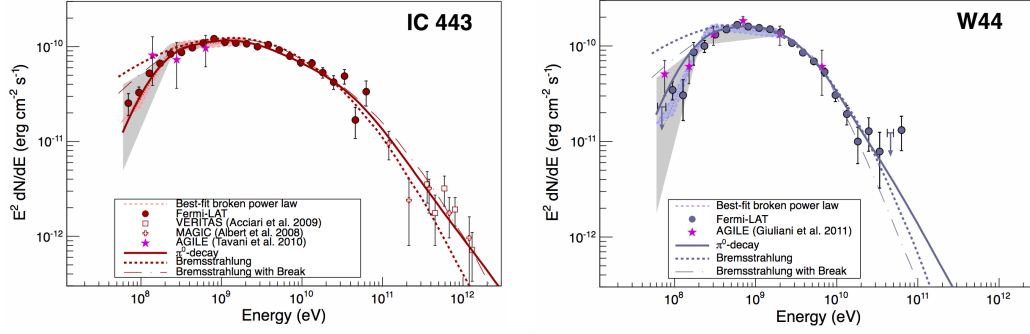
Fig. 1.6.: The steep rise below ~ 200 MeV in the gamma-ray emission of SNRs IC 443 and W44, as measured by Fermi-LAT. This characteristic signature, often referred to as "pion bump", uniquely identifies π^0-decay gamma rays and thereby high-energy protons [49].

$F(\epsilon)$, is symmetric about 67.5 MeV in a log-log representation. However, in the usual $\epsilon^2 F(\epsilon)$ representation, the characteristic of this π^0-decay spectrum is a steeply rise below ~ 200 MeV, as seen in Figure 1.6. SNR W44 and IC443 are the first SNR clearly showing this characteristic spectral feature, referred to as the "pion bump", which uniquely identifies π^0-decay gamma rays and thereby high-energy protons [49]. The steep gamma ray spectrum at high energies suggests however that the acceleration process is no longer very active, as one may qualitatively have expected for old SNRs [50].

1.2.3 The CR-γ-Neutrino Connection: Neutrino Astronomy

The bottom-up scenarios are only valid for the acceleration of charged particles, but not neutral ones. Neutral particles such as photons and neutrinos result from interactions of accelerated charged particles with the surroundings. Accelerated protons will interact with photons mostly via the Δ^+ resonance:

$$p\gamma(\to \Delta^+) \to \begin{cases} p + \pi^0 \\ n + \pi^+ \end{cases}$$

and with nucleons:

$$pp \to \begin{cases} p + p + \pi^0 \\ p + n + \pi^+ \end{cases}$$

$$pn \to \begin{cases} p + n + \pi^0 \\ p + p + \pi^- \end{cases}$$

Charged pions have a mean lifetime of 10^{-8} seconds, decaying into a muon and a muon neutrino, with a branching ratio of 99.98% of the decays. The muon will then

also decay producing other neutrinos, while neutral pions decay into two gamma rays:

$$
\begin{aligned}
\pi^+ &\to \mu^+ + \nu_\mu \\
&\mu^+ \to e^+ + \nu_e + \overline{\nu}_\mu \\
\pi^- &\to \mu^- + \overline{\nu}_\mu \\
&\mu^- \to e^- + \overline{\nu}_e + \nu_\mu \\
\pi^0 &\to \gamma\gamma
\end{aligned}
\tag{1.3}
$$

Therefore, the energy escaping the accelerating source is distributed between CRs, γ-rays and neutrinos, imposing a limit on the neutrino energy generation that can never exceed the generation rate of high-energy protons. The calculated upper bound of $E^2\Phi^2 < 4.5 \times 10^{-8}$ GeV cm^2 s^{-1} sr^{-1} is often referred to as the Waxman-Bahcall flux [51]. Contrary to gamma rays, the observation of an astrophysical neutrino flux unambiguously associated to its source is always a smoking gun of the presence of a hadronic component. The most prominent production of astrophysical neutrinos results from Equation 1.3, where γ-rays are the decay product of neutral pions, while neutrinos arise from charged pion decays. As a rule of thumb, the typical mean neutrino energy follows $E_\nu \sim 1/4\, E_\pi \sim 1/20\, E_p$, meaning that protons at the knee (few PeV) will produce ~ 100 TeV neutrinos [52]. Such a TeV-EeV neutrino flux can also be linked to a GeV-TeV gamma-ray flux, given that gamma rays with energies above the TeV will interact with the CMB or with the EBL and cascade down to lower energies.

To summarize, the neutrino is the only known astrophysical probe which:

- is electrically neutral, so that its trajectory will not be affected by magnetic fields,
- is stable, so that it will reach us from distant sources,
- it is weakly interacting, so that it will penetrate regions opaque to photons.

Neutrinos allow to observe the inner workings of the astrophysical objects and to obtain a description of the Universe over a larger range of energies. Multi-messenger campaigns that include neutrino observations are the key to solve long lasting and outstanding problems of high energy astronomy.

1.3 High-Energy Neutrino sources

In this section we will review the candidate sources of high-energy neutrinos, dividing them into galactic and extragalactic ones. The only difference between galactic neutrinos and extragalactic neutrinos is related to the energy thresholds of the

primary cosmic rays that the acceleration sites can reach. Models that predict neutrino fluxes at Earth are however uncertain, and predictions can vary by many orders of magnitude. For each source presented we will also report the latest gamma-ray and neutrino astronomy results.

1.3.1 Galactic Sources

The simplest conventional belief is to assume that the maximum energy a proton can reach from being accelerated in galactic sources is $< 10^{15}$ eV (up to the *knee*). Therefore the highest energy neutrinos produced in local galactic sources can reach ~ 100 TeV [53]. Their proximity to Earth (d$\sim$ 1-10 kpc) and the resulting geometrical effect on the solid angle, imply that to produce the same event rate, a galactic source requires a luminosity orders of magnitude smaller than an extragalactic one.

Supernova Remnants (SNRs): SNRs are expanding shells of matter left over after a supernova explosion. With their strong shock environments, SNRs are considered to be the best candidate sites for CR acceleration in our Galaxy, up to the "knee" energies of $E = 10^{15}$ eV. In the last years, the three major arrays of atmospheric Cherenkov telescopes, H.E.S.S., MAGIC and VERITAS, have been key players in establishing SNRs as sources of VHE γ-ray emission allowing direct investigation of the SNR population as source of cosmic rays, combining both spectral and morphological measurements. However, whether SNRs are the powerhouses for galactic cosmic-ray acceleration all the way up to the knee region, still remains an unsolved question. Two long-sought fundamental signatures were believed to finally close this debate: the first one being the detection of a clear gamma-ray signature of π^0 decay, and the second one the identification of a photon spectrum up to PeV energies. In 2013 the gamma-ray mission Fermi Large Area Telescope established, for the first time for a SNR, the spectral continuum below 200 MeV, which can be unambiguously attributed to neutral pion decay [49]. The leptonic scenario is therefore excluded as the main contribution to the gamma-ray emission of SNRs IC 443 and W44. However, as reported in Figure 1.6, the gamma spectrum falls steeply at higher energies, due to the fact that these supernovae are old and not capable anymore to accelerate particles up to the knee. The detection of a PeV photon spectrum has been announced in 2016 by the H.E.S.S. collaboration, being associated however to the supermassive black hole Sagittarius A* at the center of the Galaxy. It is therefore still not possible to unambiguously attribute the galactic cosmic-ray acceleration to SNRs. When consulting the TevCat catalog for SNR, about 60 gamma-ray spectra from SNRs have been detected with around 15 shell-type SNR detections at TeV energies [54]. For most of the cases, unambiguous signatures of hadronic or leptonic acceleration are missing, but the spectral behavior up to 10 TeV gamma-ray energy is known. This corresponds to cosmic-ray proton energies of around 100 TeV, reaching

to a factor of 10 below the knee. Hence, these spectra can be used to try to estimate a possible contribution of SNRs to the total Galactic cosmic ray spectrum and energy budget [55]. The main future challenge for IACTs is to detect gamma rays above 100 TeV. This is one of the main science goals of the future Cherenkov Telescope Array (CTA), the next generation ground-based gamma-ray facility, with more than 100 telescopes located in the northern and southern hemispheres [56].

Unfortunately for IceCube, the brightest SNRs are located in the Southern Sky, where the detector is overwhelmed by the atmospheric muon background. The iconic γ-ray SNR RX J1713.7-3946 for example is one of the brightest Galactic SNRs both in X-ray and TeV emission, is located at a declination (usually indicated as DEC or δ, see Figure 2.6) of $\delta \sim$ -40°. RX J1713.7-3946 has been the subject of endless debate about the nature of its photon acceleration [57]. In 2002 the CANGAROO collaboration was the first to produce evidence of hadronic acceleration of gamma rays in RX J1713.7-3946 [58]. The energy spectrum of the γ-ray emission from the supernova remnant matches that expected if the γ-rays are the product of π^0 decays generated in pp collisions. Gamma rays of energies up to $\sim$ 10 TeV have been observed, indicating that protons are accelerated up to $E_p^{max} \sim$ 100 TeV. The associated neutrino energy is $E_\nu^{max} \sim$ 10 TeV [59]. The associated neutrino flux has been calculated to be 40 muon-type neutrinos per kilometer-squared per year, making RX J1713.7-3946 only accesible to a northern hemisphere neutrino telescope as ANTARES or KM3NeT [59].

Pulsars and Pulsar Wind Nebulae (PWNe): pulsars are fast-rotating, highly magnetized neutron stars. Their emission is collimated, and the emission region is located near the pole of the star along the spin axis. Pulsars have been observed in different wavelengths, mostly radio, optical and X-ray. Most of the rotational energy lost by such a star powers highly relativistic magnetized winds of leptons which produce the so called pulsar wind nebulae. PWNe are also often called Crab-like SNRs, in honor of the most studied of them, the Crab Nebula, located in the northern sky and often used as a standard candle in gamma-ray astronomy. Several PWNe have been detected in the TeV band in the last decade, thanks to IACTs the TeVCat catalog contains nowadays 34 PWNe. The TeV emission is typically interpreted in a purely leptonic scenario, but the possibility that also relativistic hadrons are present in these nebulae is often considered [60]. IceCube's sensitivity to the Crab neutrino emission is presented in Figure 1.7, using the latest 7 years of data [61], with respect to two models. The same IceCube paper quotes as the most significant source in a catalog search the PWN H.E.S.S. J1616-508, with a post-trial p-value of 9.3%. Another important pulsar, not regarding the fact it may or may not be the location of cosmic-ray acceleration but with respect to the search for extended sources conducted in this work, is Geminga.
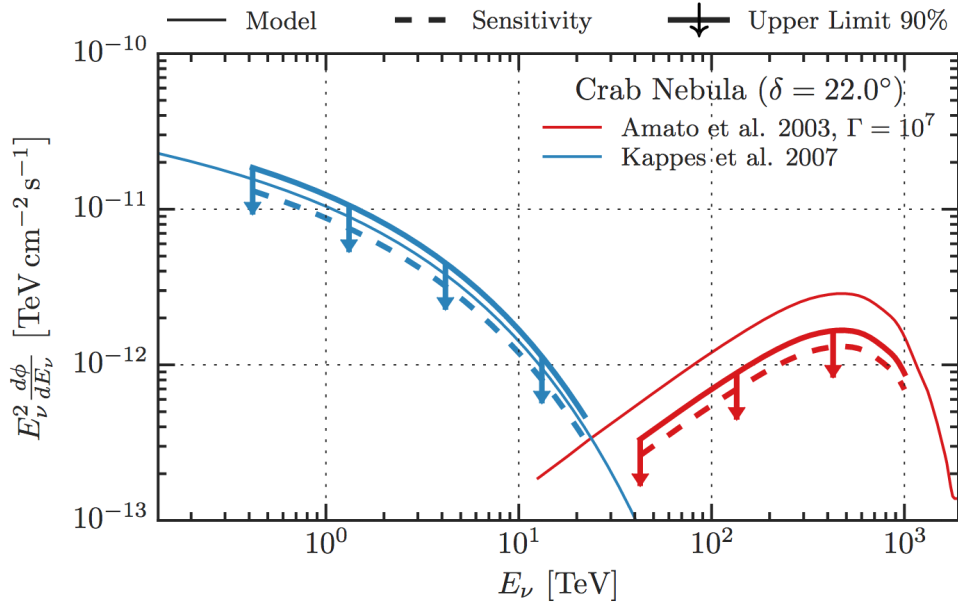
Fig. 1.7.: Blue lines represent the conversion of the observed gamma-ray flux of the Crab nebula to neutrinos [62], while red lines represent a simulation of inelastic p-p scattering at the source. Thick lines correspond to the 90% upper-limit of the 7 years point source analysis, while thin lines represent the models. The sensitivity of the same analysis is shown as dashed line [61].

Binaries/Microquasars: microquasars are binary systems in which a compact object (usually a neutron star or a black hole up to a few solar masses) receives matter from a donor star. They might show relativistic jets, observed in the radio band [63], and some show a periodic TeV photon signal [64]. Internal shocks might accelerate protons up to 10^{16} eV, and the resulting $p\gamma$ interactions might therefore produce neutrinos. The detection of TeV gamma rays from LS 5039 by H.E.S.S. has been one of the most exciting discoveries of observational gamma-ray astronomy in the very high energy regime. This result demonstrates that X-ray binaries with relativistic jets are sites of effective acceleration of particles (electrons and/or protons) to multi-TeV energies. However, the usual dilemma that follows TeV gamma detections arises again: are these photons produced in a hadronic or leptonic environment? Neutrino fluxes are described for example in [65, 66]. For the particular case of LS 5039, the minimum neutrino flux above 1 TeV has been calculated to be at the level of 10^{-12} per cm^2 per second, however, it could be up to a factor of 100 larger [67]. A time-correlated search for neutrinos from microquasars has been conducted by the ANTARES Collaboration [68]. The results, shown in Figure 1.8, are above the expectations for all the sources and cannot constrain the model parameters from [69]. After IceCube's discovery of an astrophysical neutrino flux, new attempts to associate these neutrinos to microquasars were perfomed: if LS 5039 has a compact object powering jets, it could accelerate protons up to above about 30 PeV. These highly relativistic protons could subsequently interact with the plasma producing a
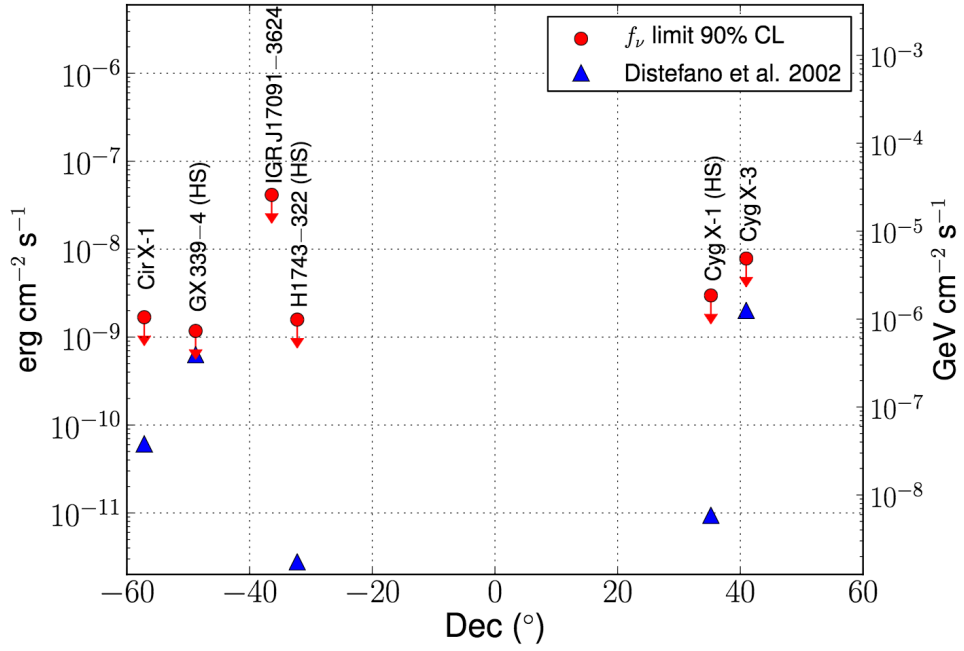
Fig. 1.8.: ANTARES results of a time-correlated search for neutrinos from microquasars. Feldman-Cousins 90% confidence level upper limits (circles) are compared with the expectations by [69] (triangles). All the results are above the expectations and no constraints can be put on the model parameters for any of the sources.

neutrino beam that could reach the maximum observed energies, $E_\nu \geq$ PeV and a neutrino flux of $\mathcal{O}(10^{-8}\ \text{GeV}^{-1}\ \text{cm}^{-2}\ \text{s}^{-1})$ [70]. LS 5039 is located in the southern sky at a declination $\delta \sim$ -14°: IceCube latest upper limits at this declination are well below $\mathcal{O}(10^{-9}\ \text{GeV}^{-1}\ \text{cm}^{-2}\ \text{s}^{-1})$ [61].

Galactic Center, Molecular Clouds and Diffuse Galactic TeV emission: with the term Central Molecular Zone (CMZ) we refer to the inner ~ 200 pc of our Galaxy, a star-forming environment with very extreme physical properties, which contains gas with densities of the order of several $10^3\ \text{cm}^{-3}$ and a total mass of $\sim 10^7\ M_\odot$ (molecular clouds). Being an excellent laboratory for fundamental astrophysics, the inner part of our Galaxy has been subject of intense studies in many wavelengths since decades, from radio to γ-rays. The galactic center compact radio source Sagittarius A* for example was discovered already in 1974, and is now known to be a supermassive black hole of about $4.4 \times 10^6\ M_\odot$ [71]. Early H.E.S.S. observations of the Galactic Center region led to the detection of a point-like source of VHE γ-rays at the gravitational center of the Galaxy (H.E.S.S. J1745-290) [72], compatible with the positions of the supermassive black hole Sagittarius A*, the SNR Sgr A East. A more sensitive exposure of the region in 2004 revealed a second source: the supernova remnant/pulsar wind nebula G 0.9+0.1 [73]. After the subsequent removal of these two bright sources, the H.E.S.S. collaboration reports in 2006 the
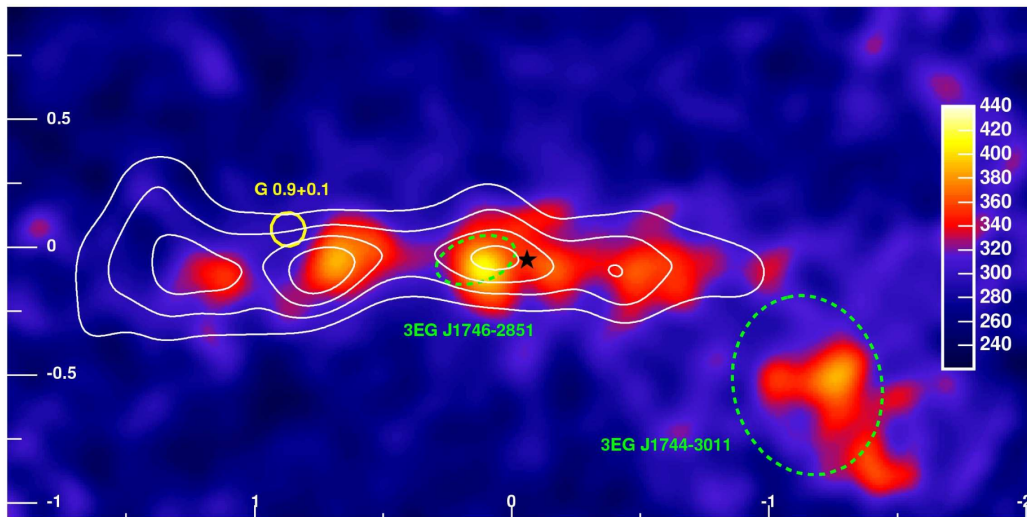
Fig. 1.9.: H.E.S.S. skymap of the Central Molecular Zone of the Galaxy. After the removal of two bright sources in the region, G 0.9+0.1 shown with a yellow circle and Sagittarius A* marked with a black star, the skymap shows a broad distribution of very high energy gamma rays. White contour lines indicate the density of molecular gas, traced by its CS emission. The 95% confidence region for the positions of two unidentified EGRET sources in the region are shown as dashed green ellipses [74].

discovery of a broad distribution of very high energy (VHE, $E > 100$ GeV) gamma rays in the Central Molecular Zone (CMZ) of the Galaxy. The skymap of the band after the subtraction of G 0.9+0.1 and Sagittarius A* is reported in Figure 1.9. The correlation of this emission with the integrated intensity of the carbon sulfur compound CS emission from the molecular cloud allows to infer a hadronic origin for the gamma rays [75]. In addition, the most recent results from H.E.S.S. report tracers of the presence of PeV particles within the central 10 parsec of the Galaxy [76]. Although its current rate of particle acceleration is not sufficient to provide a substantial contribution to Galactic cosmic rays, Sagittarius A* could have plausibly been more active over the last $\geq 10^{6-7}$ years, and should be considered as a viable alternative to SNRs as a source of PeV Galactic cosmic rays [76]. This long-sought achievement triggered a renewed interest in the estimation of the neutrino flux coming from this region of the sky. The corresponding maximum signal calculated is of a few muon events per year in the upcoming KM3NeT detector. In [77] the authors conclude that the KM3NeT detector has the best chances to observe neutrinos from Sagittarius A*, even if, in order to accumulate a large sample of signal events, several years of exposure are necessary. On the contrary the expected signal in IceCube is smaller and unlikely to be observed in view of the larger background rate caused by the atmospheric muons [77].

Two of the most exciting discoveries of the last years result from Fermi LAT observations: the discovery of the so called Fermi Bubbles and the discovery of a GeV

excess of gamma rays from the Galactic Center. The Fermi Bubbles (FB) are two giant γ-ray structures extending 50 degrees above and below the Galactic center, and about 40 degrees wide in longitude [78]. The gamma-ray emission associated with these bubbles has a significantly harder spectrum ($dN/dE \propto E^{-2}$) than the inverse Compton emission electrons in the Galactic disk, or the gamma rays proton-interstellar medium collisions. The origin is not yet fully understood, but it is possible that these Galactic gamma-ray bubbles were created by some large episode of energy injection in the Galactic center, such as past accretion events onto the central massive black hole, or a nuclear starburst in the last 10 Myr [78]. The GeV excess in gamma-ray observations of the Galactic Center has been found by several groups using Fermi LAT public datasets [79, 80]. Despite being welcomed by the dark matter community as the so long-awaited proof of WIMP annihilation, further investigations show that the excess photons are not smoothly distributed as expected for dark-matter annihilation. Their clustering reveals instead a population of unresolved point sources, likely millisecond pulsars [81].

The three years IceCube high-energy starting event (HESE) dataset, which lead to a clear detection of cosmic neutrinos at the level of 5.7σ [82], is a public dataset of 37 track- and shower-like events, now enriched with one additional year of data [83]. Despite their energy suggesting an extragalactic origin (E > 10 TeV), the significance skymap, reported in Figure 1.10, shows a tantalizing clustering close to the Galactic Center. This cluster is however not statistically significant [83]. For this dataset, information on the deposited energy (all above 20 TeV), the MJD time, the right ascension and declination of the event and the associated angular uncertainty were released, allowing its use outside the IceCube community. Among others, also an analysis to prove its origin in the Fermi Bubbles was performed using this dataset [84].

1.3.2 Extragalactic Sources

The cosmic-ray spectrum above the ankle in the region of ultra-high energies $E \geq 10^{18}$ eV, is generally assumed to have an extragalactic origin. When checking the Hillas plot in Figure 1.4, two classes of objects, Gamma-Ray Bursts (GRBs) and Active Galactic Nuclei (AGNs) are left as most likely source candidates of UHECRs.

Gamma-Ray Bursts (GRBs): GRBs are the brightest electromagnetic explosions in the universe and are observed by dedicated spacecraft detectors at an average rate of about one per day [85]. They are bright emitters of keV-MeV photons, but only on time scales of 10^{-3}-10^3 s, and the emission is highly beamed. GRB progenitors are unknown, but could be associated with black hole creation in supernovae and binary mergers. GRBs have been among the most plausible candidates to explain the
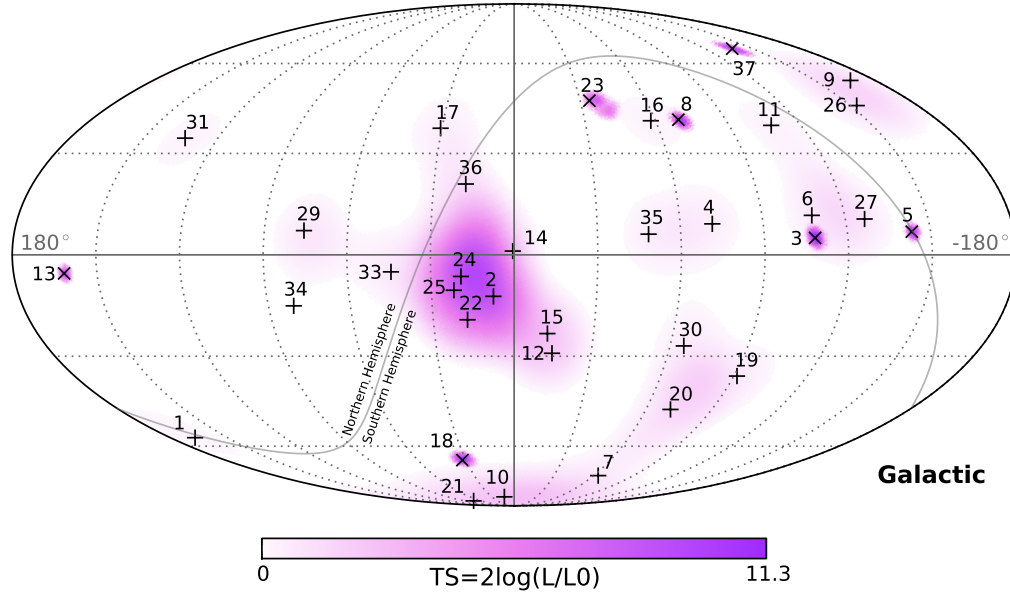
Fig. 1.10.: Arrival directions of the events belonging to the three years IceCube high-energy starting event (HESE) sample, in galactic coordinates. Shower-like events are marked with + and those containing tracks with ×. Colors show the test statistics (TS) for the point-source clustering test at each location. No significant clustering was found [82].

origin of cosmic rays with energies above the *ankle* at 10^{18} eV. There are however a few drawbacks: if the composition near the GZK cutoff is heavy (as the Auger data seems to indicate [86]), it is very unlikely that these cosmic rays could have come from GRBs. GRBs produce a huge number of MeV gamma rays, and any atomic nucleus that could remain in its vicinity long enough to be accelerated to ultra-high energies will most likely photo-disintegrate into its constituent protons and neutrons before escaping [87]. On the other hand, if UHECRs consist mostly of protons, $p\gamma$ interactions in the GRB should produce TeV neutrinos detectable by neutrino telescopes such as IceCube. As already remarked, detection of high energy neutrinos correlated with gamma-ray photons from a GRB would provide evidence of hadronic interaction in these powerful phenomena and confirm their role in UHECR production.

The quest for neutrinos from GRBs in IceCube is long-lasting. Being transient sources, a GRB search is basically background free since neutrino events coming from GRB have to be correlated in time and direction with γ-rays. To date, no neutrino signal has been detected in searches for muon neutrinos from GRBs in multiple years of data from AMANDA, the partially instrumented IceCube, and the completed IceCube detector [88, 89, 90] nor in four years of data by the ANTARES collaboration [91, 92]. But scientists are known not to give up easily: if the search for a signal of neutrinos coincident with the emission of high-energy photons (prompt neutrino

flux) is the most common yet unfruitful assumption, many other models are now being investigated, which predict time-shifted neutrino emissions, as precursors or afterglows. ANTARES results for time-shifted neutrino emission found the neutrino flux to be less than one event in the detector per hundred gamma-ray bursts at the 90% confidence level [93].

Active Galactic Nuclei (AGNs): Active Galaxies are galaxies with an accretion disk surrounding a supermassive black hole at their center, with a mass up to 10^{10} $M_\odot$. Their nucleus is so bright that it outshines the rest of the galaxy, and is therefore called AGN. It is commonly believed that the central engine, a spinning black hole surrounded by an accretion disk, and its jets parallel to the spin axis are powered by the gravitational energy released in it. Astronomers name AGNs differently, depending on the relative orientation of the jets with respect to Earth. CRs are hypothesized to be accelerated up to EeV energies in shocks formed either by matter flowing near the AGN core, or by colliding matter inside the jets. Although TeV photons are often observed from AGNs [54], the ubiquitous problem associated with their detection strikes again: it is unknown whether these are from inverse Compton scattering of the photons on the same electron population (synchrotron self-Compton, thus a leptonic process) or from hadronic processes.

A recent analysis of plausible astrophysical counterparts located within the error circles of IceCube events showed that, for nine of the IceCube neutrino events, likely counterparts include mostly BL Lacs, among which Mrk 421 [94], renewing the interest in AGNs. However, the IceCube collaboration has investigated the contribution of the 862 Fermi-LAT 2LAC blazars catalog to the astrophysical neutrino flux using three years of data. No significant spatial correlation has been found, and the maximal contribution from all 2LAC blazars to this flux has to be at most 27% in the energy range between 10 TeV and 2 PeV [95].

Starburst Galaxies: refer to galaxies with an elevated rate of star-forming regions. Galaxies undergoing a starburst phase frequently show tidal tails [96], an indication of a close encounter with another galaxy, or are in the midst of a merger. During such events stellar deaths through supernovae can be expected to rise along with the birth of massive short lived stars, and the activity of the central black holes may increase as well due to additional material available for accretion. In 2006 Loeb and Waxman [97] suggested that, because of their properties, starburst galaxies could be an important source of high-energy neutrinos. Moreover, they estimated that the level of the neutrino flux would be comparable to the Waxman-Bahcall limit [51]. Since the IceCube discovery of an unresolved flux of astrophysical neutrinos at this level, this possibility has received renewed attention.

GZK neutrinos: also called cosmogenic neutrinos, should originate from photo-hadronic interactions of cosmic-ray protons with the cosmic microwave background (CMB). UHECRs lose energy via $p\gamma$ interactions, suppressing the cosmic-ray flux at energies $\geq 5 \times 10^{19}$ eV, the so-called GZK cutoff. This cutoff has now been measured with high significance both by the Auger and TA collaborations, but the mechanism responbile for it is far from being established. Several models propose alternative scenarios where no GZK effect is needed [36]. However, if the GZK mechanism is the right tool to explain the last portion of the cosmic ray spectrum, a cosmogenic neutrino flux is guaranteed, generated through the decay of secondary charged pions [98]. Due to the low cosmic-ray flux at the energy scales involved in the GZK mechanism ($E_{CR} > 10^{19.5}$ eV), the expected neutrino flux is very low, of about one event per km^2 per century, requiring detectors of ~ 100 km^2. IceCube is not optimized for the detection of cosmogenic neutrinos, and scale up the detector to reach the required area is prohibitively expensive. For this reason the GZK neutrino detection is based on the Askaryan effect: a coherent radio emission from neutrino induced cascades, which can propagate through a radio transparent medium as the ice. The Askaryan Radio Array (ARA), currently being built at South Pole, is dedicated to such a radio detection [99].

1.4 Extended Sources

In astronomy, the definition of a spatially extended source is somehow ambiguous, since it depends on the point spread function of the instrument in use, that represents how a point source is seen. Therefore, a source is called extended when its angular size exceeds the resolution of the instrument used to observe it. Extended sources could be extended in nature, such as Supernova Remnants, or perceived as extended due to the lack of resolution that would allow to disentangle the contributions of the several point sources located close by.

1.4.1 Extended Sources in the High-Energy Gamma-Ray Sky

The H.E.S.S. survey of the inner part of the Galactic Plane [100] has revealed a number of bright extended γ-ray sources: if part of the γ-ray acceleration arises from hadronic processes, the same extended sources should be seen by means of neutrino detection. At lower energies, the Fermi-LAT satellite sees most of the same sources above 100 GeV [101]. The Milagro gamma-ray detector observed as well a significant number of extended gamma-ray emission regions along the Galactic Plane, specially in the direction of the constellation Cygnus, see Figure 1.11 [102].
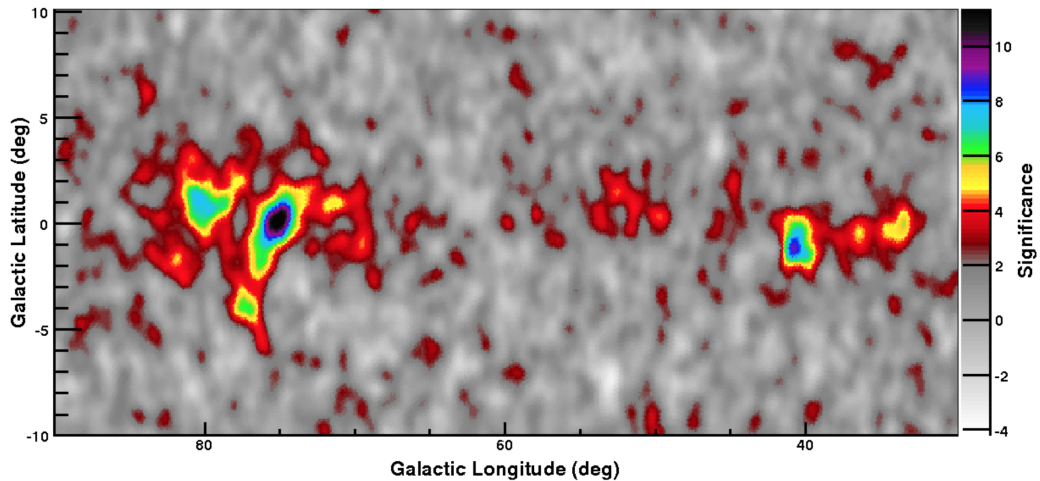
Fig. 1.11.: TeV gamma-ray image of the Inner Galaxy from Milagro [102]. MGRO 1908+06 is the source at about $40°$ longitude. The set of sources at $70° - 80°$ longitude coincides with the Cygnus region.

Despite it generally being believed that the radio quiet pulsar Geminga and its associated PWN are leptonic accelerators, Milagro reports a TeV emission from an extended area of $\sim 3°$ spacially consistent with the pulsar, with a significance of approximately 7σ [103]. HAWC observes a similarly extended source [104]. Due to the higher angular resolution, most of the objects in the latest 2FHL catalog flagged as extended are actually point sources for IceCube, with the most extended source being the Cygnus Cocoon, which reaches and extent of $\sim 2°$.

1.4.2 Extended Sources in the High-Energy Cosmic-Ray Sky

Until now we have mostly described results originating from the study of photons, for energies in the galactic and extragalactic domain. Charged particles are deflected by galactic magnetic fields, but at EeV energies cosmic-ray protons point back at their origin. For small-enough magnetic deflections, the distribution of the arrival directions of UHECRs with energies $E > 4 \times 10^{19}$ eV could mirror the inhomogeneous distribution of the nearby extragalactic matter. The search for anisotropy at small and intermediate angular scale at the highest energies is thus potentially the most powerful way to infer the sources of UHECRs. The Pierre Auger Observatory has carried out comprehensive anisotropy searches for different energy thresholds between 40 and 80 EeV and within different angular windows, between $1°$ and $30°$. Searches for significant excesses anywhere in the sky have been performed, as well as searches for correlations with known astrophysical structures and with objects that are considered plausible candidates for UHECR sources. None of the analyses provides any statistically significant evidence of anisotropy. The most significant

excess (4.3σ pre-trial) corresponds to a region close to the super-Galactic plane and to the direction of Centaurus A, the closest radio-loud AGN at an energy threshold of 54 EeV and angular scale of 12° [105]. Also the Telescope Array collaboration has performed similar searches for anisotropies above 57 EeV. Using data collected over a 5-year period, a cluster of events has been found by oversampling the sky map using 12°-radius circles [106]. In the search for small scale cosmic-ray anisotropies, which could possibly lead to the detection of gamma-ray point sources, the KASCADE experiment [107] has reported the detection of an excess of 5.5σ observed at an area around 77.75° RA, 70.85° DEC. Despite the angular scale of the excess is not always compatible with the neutrino searches described in this work in Chapter 4, all these examples are important hints that motivate the search of extended sources in the neutrino channel.

Principles of Neutrino Detection | 2

In this chapter, we present the fundamental neutrino interactions and describe the characteristic signatures these events leave in the IceCube detector. We will also introduce the coordinate systems needed and the backgrounds of the analysis, described later in Chapter 6. "We made the impossible seem easy" states a quote at the IceCube headquarters in Madison, Wisconsin. IceCube's important achievements shall not deceive anyone: catching such a ghost particle is not an easy task, and we will now discover how extremely elusive neutrinos are.

2.1 Neutrino-nucleon Interaction

Neutrinos interact exclusively via the weak nuclear force, and it is possible to detect them only via secondary particles produced in the interaction. Because of the electron's small mass and its impact on the cross section, neutrino-electron interactions can generally be neglected with respect to neutrino-nucleon interactions [108]. There is one exceptional case, the resonant formation of the intermediate boson W^- in $\overline{\nu}_e e^-$ interactions at 6.3 PeV. At the resonance, the cross section is larger than the νN cross section at any energy up to 10^{12} GeV (Figure 2.1).

For neutrinos above $\mathcal{O}$(TeV) energies, deep inelastic scattering (DIS) is the dominant process for neutrino-nucleon interaction. Neutrinos interact with nucleons by either the charged current (CC) or neutral current (NC) interactions. The CC interaction is mediated by a $W^{\pm}$ boson, while the NC interaction is mediated by the Z^0 boson, as sketched in the Feynman diagrams on Fig. 2.2.

The CC interaction

$$\nu_l(\overline{\nu}_l) + N \rightarrow l^-(l^+) + X \tag{2.1}$$

has a cross section shown in Figure 2.1. Here l is any lepton flavour (e, μ or τ) and X is the nuclear remnant. On average, the produced lepton carries from 50% (for $E_\nu \sim$10 GeV) to 80% (at higher energies) of the neutrino energy. The remainder of the energy is transferred to the nuclear target and released in the form of hadronic showers. In NC interactions, no charged lepton is present in the final state. Hence, the only way to observe them is through the shower from the nuclear remnant.
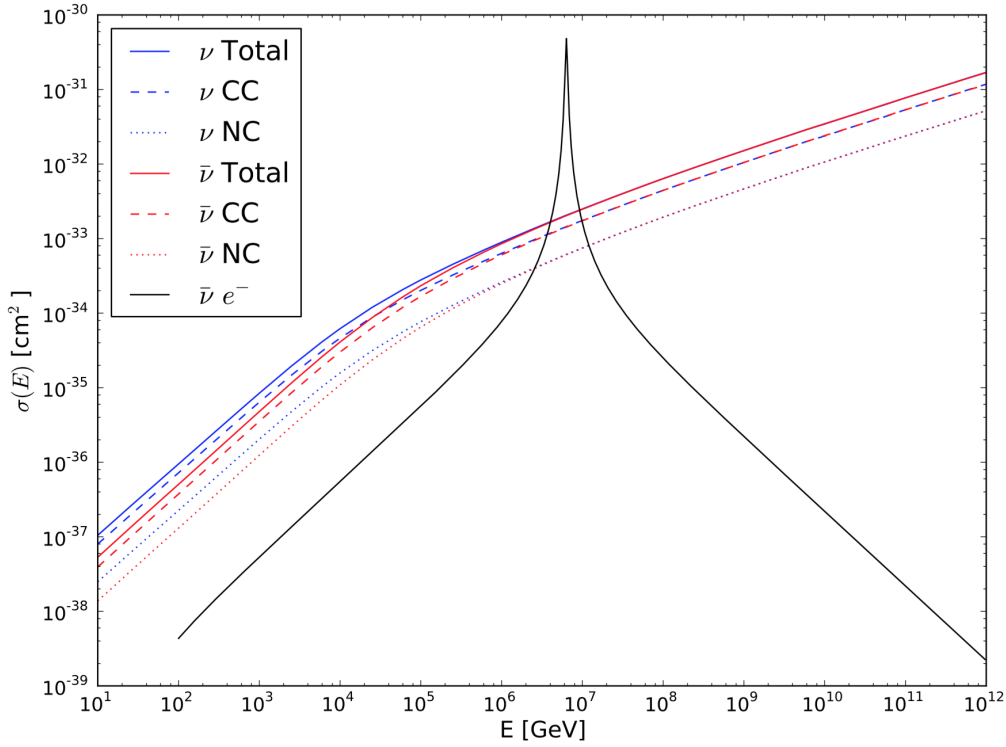
Fig. 2.1.: Neutrino-nucleon and antineutrino-electron scattering cross-sections as a function of neutrino energy from [109] based on data from [108]. From bottom to top at low energy, the cross-sections are for $\overline{\nu}$ NC, ν NC, $\overline{\nu}$ CC, $\overline{\nu}$ total, ν CC, and ν total. The resonance peaked at 6.3 PeV is the antineutrino-electron resonance (Glashow resonance).
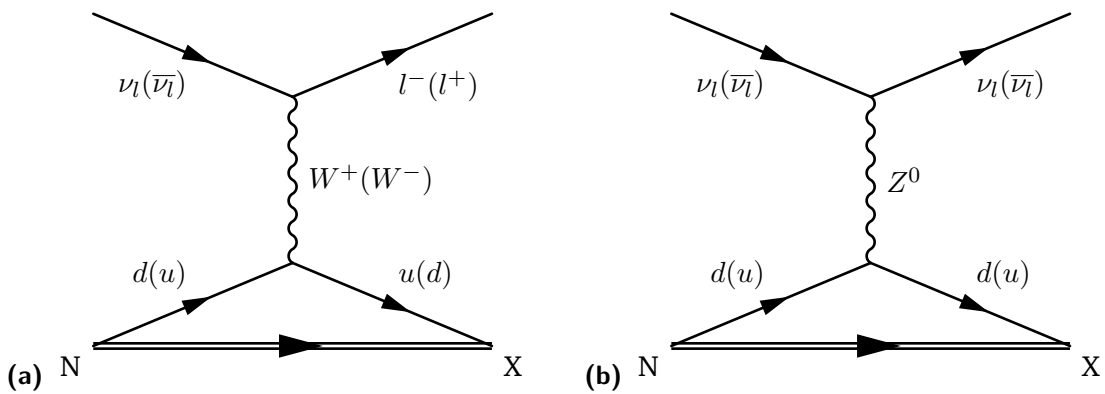
Fig. 2.2.: Feynman diagrams of the charged current (a) and the neutral current (b) interactions of a neutrino on a nucleon N. Charged-current interactions create charged leptons accompanied by a hadronic cascade, while neutral-current interactions only create the hadronic component

Both CC and NC cross sections are energy dependent and increase with the neutrino energy. At low energies ($E_\nu \ll M_w^2/2M_N$) the cross section is proportional to E_ν, while at higher energies ($E_\nu \gg M_w^2/2M_N$) the cross section becomes proportional to $E_\nu^{0.363}$ [110].

2.2 Particle Interactions and Event Topologies in IceCube

IceCube bases its detection principle on the Cherenkov light emitted by the secondary particles induced by neutrino-nucleon DIS interactions. These particles include muons, electrons and hadrons, which produce distinctive light patterns in the instrumented array. Two major classes can be distinguished, track-like and cascade-like events. Cascade signatures are the results of short ranged energy deposits caused by electromagnetic or hadronic cascades in the final state of the neutrino interaction. The maximum of a 100 TeV electromagnetic cascade occurs 5 m from the neutrino interaction vertex. This is approximately a point source of light with respect to the dimensions of the detector. On the other hand, in case of a so called track-like event, a high energetic muon is present in the final state, which can travel large distances before decaying. If the muon is crossing the detector volume, it is possible to detect muon neutrinos that interacted far away from the detector. The energy loss along the path and the muon itself produce Cherenkov light. The typical event signature in this case is a track of light propagating through the detector.

Summarizing the possible neutrino interactions and resulting event topologies in IceCube:

- all NC interactions have hadronic cascades in the final state, thus appearing as cascade-like events (Figure 2.3a).

- CC electron neutrino events have a hadronic and an electromagnetic cascade in the finale state. They appear as cascade-like events (Figure 2.3a).

- CC muon neutrino events have a muon and a hadronic cascade in the final state. Most of the time, despite the hadronic cascade, the track nature of the muon dominates this event topology (Figure 2.3b). If, however, the ν_μ interaction vertex is inside the detector volume, light can also be observed from the hadronic cascade.

(a) Cascade, ν_e CC, ν_x NC, low energy ν_τ **(b)** Track, ν_μ CC

(c) High energy ν_τ (*double-bang*)
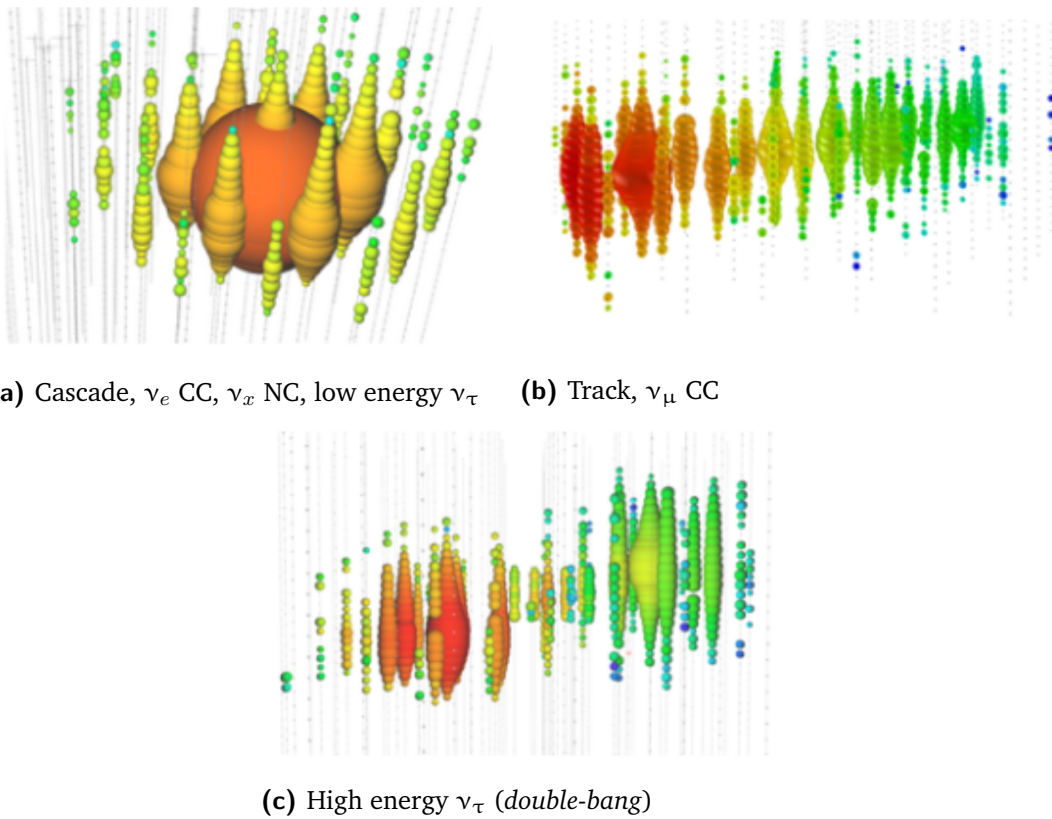
Fig. 2.3.: Different signatures of data (2.3a, 2.3b) and simulated (2.3c) events in the IceCube detector. The colors indicate the photon arrival time from red (early) to green (late) and the size of the sphere the amount of measured charge.

- CC tau neutrino events will have a tau and a hadronic cascade in the final state. As the tau decays in 18% of the cases into a muon, some events might appear as tracks. When the tau decays into electrons or hadrons the event would appear as a cascade. At energies above 1 PeV, a ν_τ undergoing CC interaction in IceCube produces a hadronic cascade and a τ lepton that can penetrate tens of meters through the ice before decaying. The branching ratios of τ decay into hadrons, electrons and muons are 64.8% , 17.8% and 17.4% of the time. Hadronic and electronic τ decays will produce a second cascade. These two subsequent depositions of energy would form the distinctive pattern of a "double bang" signature for ν_τ in IceCube (Figure 2.3c). To date, this peculiar signature has not been observed.

It should be mentioned, that it is very difficult to distinguish between hadronic and electromagnetic cascades, because they appear very similar in terms of Cherenkov light production, which will be described below. Attempts to distinguish between a CC electron neutrino event and a NC event of any flavor are currently under investigation, and exploit neutron thermalization.

2.2.1 Cherenkov Radiation

Cherenkov radiation arises when a charged particle travels in a medium and its speed $v = \beta c$ exceeds the phase velocity of light c/n in the medium, where n is the index of refraction of the medium. Given an index of refraction of n = 1.31 for ice, the corresponding threshold energies of electrons and muons are $E_{th} \sim 0.8$ MeV and $E_{th} \sim 160$ MeV respectively. Cherenkov photons are emitted coherently at a well-defined angle $\cos\theta_C = \frac{1}{\beta n(\lambda)}$, where $\theta_C \sim 41°$ in ice. The number of photons N emitted per track length dx is given by the Frank-Tamm formula [111]:

$$\frac{d^2N}{dxd\lambda} = \frac{2\pi z^2 \alpha}{\lambda^2}\left(1 - \frac{1}{\beta^2 n^2(\lambda)}\right) \tag{2.2}$$

where $\alpha \approx 1/137$ is the fine structure constant and λ the wavelength. The total number of Cherenkov photons induced as a result of the energy deposition in the ice is a function of the total track length of relativistic charged particles in the event. In the wavelength range relevant for water-based neutrino telescopes of about 300 nm to 600 nm, the number of photons per track length is approximately

$$\frac{dN}{dx} = 3.4 \cdot 10^4 \text{ m}^{-1} . \tag{2.3}$$

2.2.2 CC ν_μ interactions

Charged-current ν_μ interactions produce muons via:

$$\nu_\mu(\bar\nu_\mu) + q \rightarrow \mu^-(\mu^+) + q' . \tag{2.4}$$

These muons have sufficient energy to travel unperturbed by Earth's magnetic field. They lose energy via continuous (ionization) or stochastic mechanisms (bremsstrahlung, photo-nuclear interactions, pair production), Figure 2.4. The classical way to describe the average muon energy loss is:

$$\frac{dE_\mu}{dx} = -a - bE_\mu \tag{2.5}$$

where a accounts for ionization losses and $b = b_{br} + b_{pair} + b_{ph}$ accounts for the stochastic part. A very rough estimate gives values for $a \approx 2$ MeV$(g/cm^2)^{-1}$ and $b \approx 4 \times 10^{-6}$ $(g/cm^2)^{-1}$. With this energy loss rate, muons are able to travel through many kilometers of ice before dropping below the Cherenkov threshold. This can be seen in Figure 2.5, where the ranges of all CC interaction product particles are shown. The long range of product muons provides a good lever arm for angular reconstruction and IceCube effective volume is increased, given the ability to detect
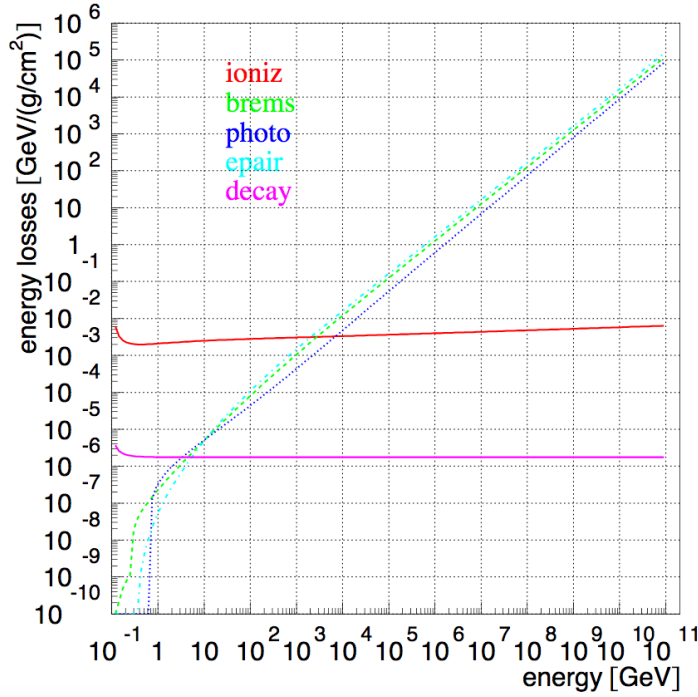
Fig. 2.4.: Muon energy losses in the ice as a funtion of energy: ionization (red), bremsstrahlung (green), photonuclear interactions (blue), pair production (cyan) and decay (pink) [112].

muons that originated from interactions outside the detector. An example of the signature left by a muon crossing the IceCube detector is shown in Figure 2.3b.

2.2.3 CC ν_e interactions

In a charged-current electron neutrino interaction, the final state presents a free electron (or positron), that initiates an electromagnetic cascade in the ice. Energy losses for electrons are similar to the muon ones, except for the fact that electrons are much lighter, and will thus lose energy much faster and stop more quickly in matter. Gammas are created via bremsstrahlung, which create an e^+e^- pair. Bremsstrahlung dominates the energy loss processes for high-energy electrons. The average energy loss is described this time by:

$$\left(\frac{dE}{dx}\right)_{rad} = -\frac{E}{X_0} \tag{2.6}$$

where X_0 is the electron radiation length ($X_0 \approx 39$ cm in ice [114]) representing the average distance after which an electron has reduced its energy of a factor 1/e. The critical energy, above which bremsstrahlung dominates over ionization, is $E_c \sim 72$ MeV for an electron in the ice. The shower process continues until all the particles fall below E_c. Electromagnetic cascades lose all their energy over 10 m,
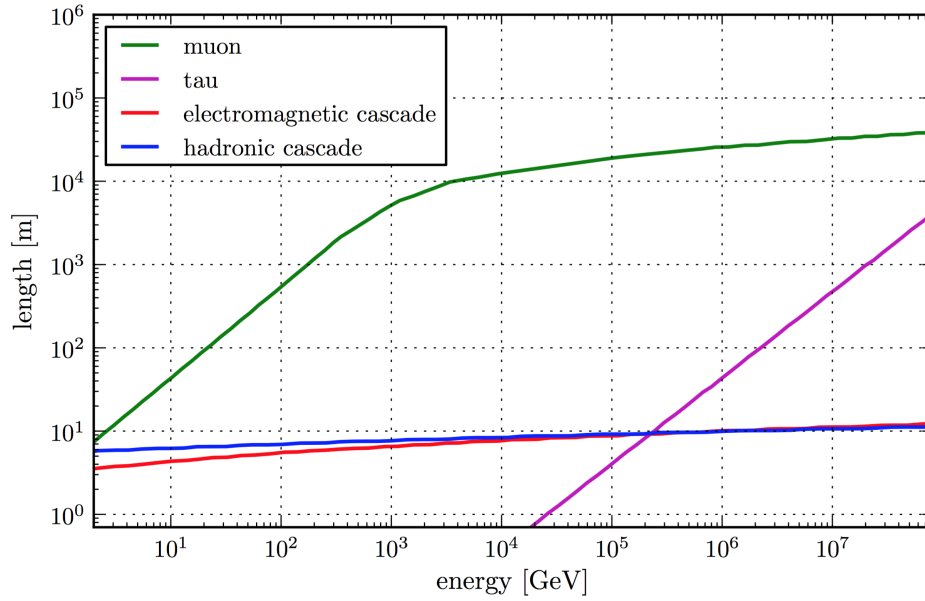
Fig. 2.5.: Range of neutrino interaction products in ice as a function of primary neutrino energy. For all interactions, the range increases with energy; however, this dependence is much stronger for muons and taus than for the other channels. Muons travel the farthest for most of IceCube's sensitive energy range. Image from [113].

as can be seen in Figure 2.5. The characteristic cascade signature in the IceCube detector is shown in Figure 2.3a.

2.2.4 CC ν_τ interactions

Due to its very short lifetime of $\sim 3{\cdot}10^{-13}$ s, a tau lepton will only travel a short distance before decaying. Because of its high mass, it is essentially a minimum ionizing particle up to 50 PeV. Taus decay into a tau neutrino and either a quark-antiquark pair (65% ot the time) or a lepton pair (15% of the time). A PeV tau will only travel ~ 50 m before decaying, leaving a cascade signature in the detector indistinguishable from NC or ν_e interactions. The characteristic tau signature, often referred to as *double-bang*, is only achieved not only if the particle has energies of few PeV and is able to propagate a resolvable distance, but also if both the neutrino interaction and the tau decay occur inside the detector. A simulated *double-bang* is shown in Figure 2.3c. Cases when either one of the two interactions happens outside the detector, leaving a dim track preceded or followed by a cascade, are know as *lollipop* or *inverse-lollipop* signature. A *lollipop* signature is not distinguishable from a CC ν_μ interaction with the ν_μ interaction vertex is inside the detector volume.

2.3 Coordinate systems, background signals and the role of Earth

Like almost every other experiment, also neutrino telescopes try to cope with their background sources. The main one for this analysis consisting of atmospheric muons. Since background signals differentiate with respect to the hemisphere taken into account, whether the northern or the southern one, we will briefly introduce the reference systems needed to understand why events are labeled as *upgoing* or *downgoing*, and how angles as right ascension (RA) and declination (DEC) are defined.

2.3.1 Coordinate systems

In the IceCube reference system, centered on the detector, particles coming from the Southern Sky cross the detector from the top to the bottom and are therefore called *downgoing*. On the other hand, particles coming from the northern sky cross the detector in the opposite direction and are therefore called *upgoing*. There are two other important coordinate systems used in astrophysics to locate objects in the sky: equatorial and local coordinates. Astronomical objects are most commonly located in the celestial sphere by a coordinate system referred to as the equatorial coordinate system, schematically represented in Figure 2.6. This is the system in which the Universe is "at rest": aside from solar system objects and stars near the solar system, astronomical objects do not move, and their position is fixed in the celestial sphere. The celestial sphere shares the equator and poles with Earth. The coordinates in this system are Right Ascension (commonly abbreviated RA or α) and Declination (commonly abbreviated DEC or δ). Values of RA are usually reported in degrees or hours, and values range between $0°$ to $360°$ or between 0h to 24h, with $360°$ (24h) being equivalent to the full circle. Due to Earth's rotation, the celestial sphere seems to rotate around our motionless world once in (about) 24 hours. For the declination angle, values are expressed in degrees, and range from $-90° \leq \delta \leq 90°$, where the extremes are the celestial south and north pole respectively. IceCube data are however stored using the local coordinate system, which is slightly different from the standard local coordinates used in astronomy. The zenith is defined in the standard way as the point overhead of the observer, and the zenith angle θ has the origin at this point. The azimuth angle ϕ is instead defined differently. The standard definition of azimuth is North($0°$) => East($90°$) => South($180°$) => West($270°$), meaning that from the North the azimuth angle is defined clockwise. At the South Pole the North is indicated by the Prime Meridian. IceCube uses grid coordinates but the definition of azimuth starts from East and moves counterclockwise: Grid East($0°$) => Grid North($90°$) => Grid West($180°$) => Grid South($270°$).
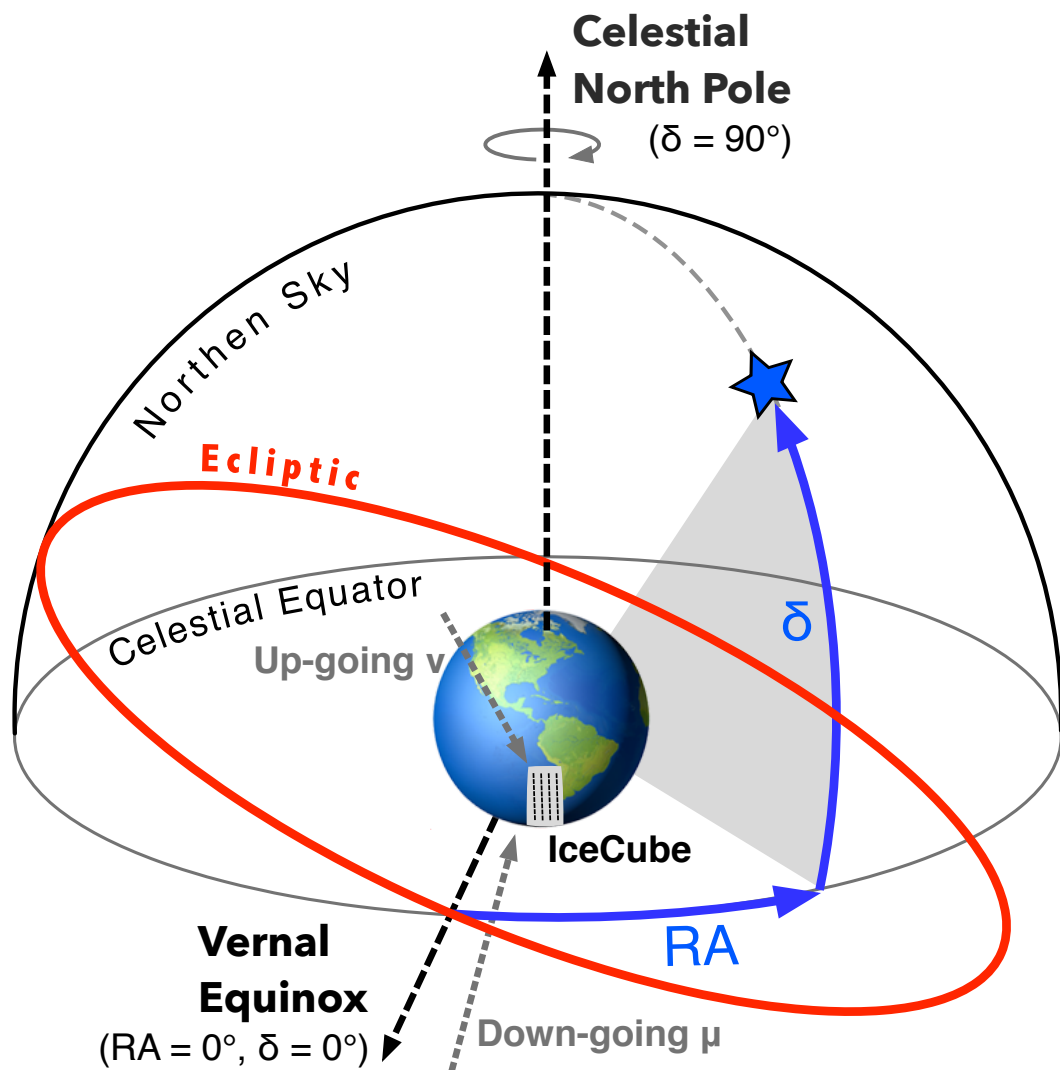
Fig. 2.6.: Schematic view of the Equatorial coordinate system with declination and right ascension. The northern sky with upgoing events is shown, as well as downgoing events from the southern sky. The ecliptic represents the apparent motion of the Sun on the celestial sphere throughout a year.

2.3.2 Background signals and the role of Earth

Cosmic rays reaching Earth's atmosphere with enough energy will produce extensive air showers that will contain a significant number of muons (Figure 2.7). The flux of these muons is significantly higher than the expected flux of muons due to neutrino interactions. As an air shower usually produces more than one muon, most of these muons arrive at the detectors in bundles. This atmospheric muon background type is the main reason to build neutrino detectors at deep sites, where the overburden above the detector acts as a shield against these muons. But, even at large depths, atmospheric muons are the most common events seen in the detector. Therefore, neutrino telescopes predominantly look at upgoing muons, using the whole planet as a muon shield and relying on robust track reconstruction algorithms to minimize the fraction of mis-reconstructed tracks. Bundles of muons or even two coincident muons from separate air showers can lead to signatures in the detector that closely resemble these of upgoing muon tracks. Looking downwards will only work up to an energy of about 1 PeV, as above this energy, the Earth starts to become opaque also to neutrinos, as the neutrino-nucleon cross section increases with energy. Mis-reconstructed muons represent the reducible background in the northern hemisphere, and we act on it by quality cuts on the reconstructed tracks. In the southern hemisphere, the current strategy to get over atmospheric muons and reduce the background rate is to cut in energy.

Atmospheric muons are accompanied by another background signal, atmospheric neutrinos. Hadronic air showers do not only produce muons (Figure 2.7). Decays of charged pions and kaons also yield a large flux of high-energetic neutrinos, which will be visible to a neutrino detector on top of the flux of cosmic neutrinos. In case of atmospheric neutrinos it is not possible to use the Earth as a shield. Atmospheric neutrinos represent an irreducible background for any cosmic neutrino signal, both for the northern and southern hemispheres. However, as can be seen from Figure 2.8, the energy spectrum of atmospheric neutrinos is softer than the signal expected from cosmic sources. Pions and kaons in showers form the so called "conventional" atmospheric neutrino flux, while charm mesons contribute to the "prompt" component. The energy dependence of the conventional flux is given by the spectrum of the parent cosmic ray, with a spectral index around 3 below 100 GeV. With rising energy the mesons travel longer distances and interact and lose energy before decaying into neutrinos. Thus, the atmospheric neutrino spectrum is steeper than the primary cosmic ray spectrum with a spectral index of $\gamma \approx 3.7$ in the energy range 1 TeV to 1 PeV [116]. Moreover, the flux shows a zenith dependence because the distance a muon has to travel before hitting the ground increases with the zenith angle.
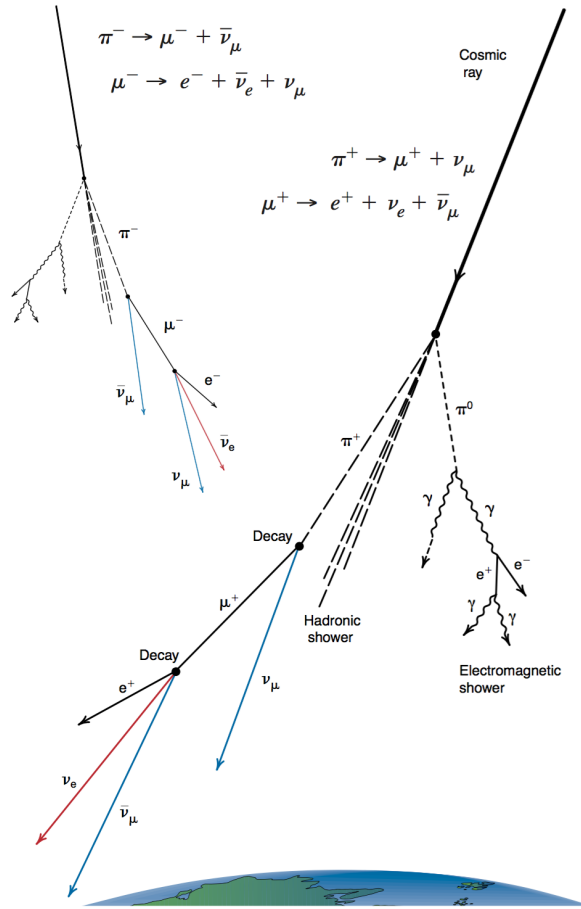
Fig. 2.7.: Diagram of a cosmic-ray air shower. The flux of muons and neutrinos from the hadronic component forms the dominant background for most astrophysical neutrino searches, this analysis included. Image from [115].
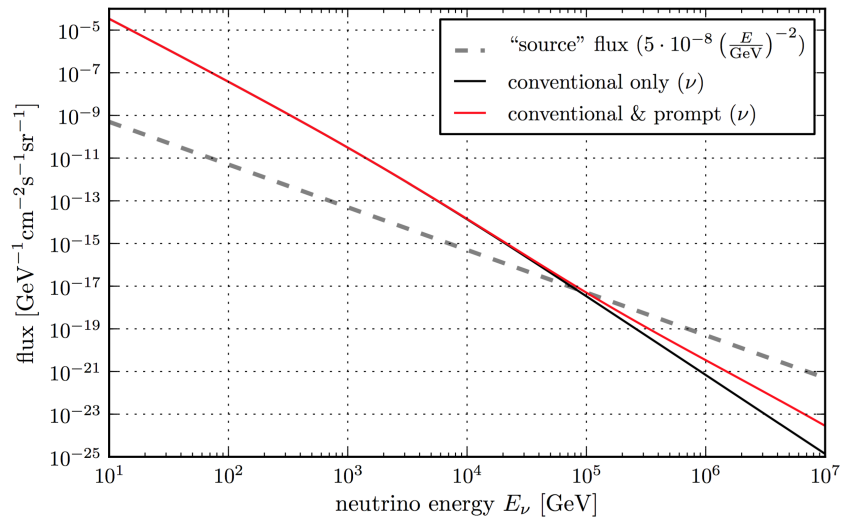
Fig. 2.8.: Atmospheric neutrino spectrum compared to an E^{-2} "source" spectrum. Image from [113].

The IceCube Neutrino Observatory

<div style="text-align: right; font-size: 3em;">3</div>

IceCube is a neutrino telescope located at the geographic South Pole. Among its scientific goals, the study of a recently discovered diffuse astrophysical neutrino flux is the main one. As seen in the previous chapter, neutrinos are observed via the optical detection of secondary particles produced in the interactions with ice nucleons. After having briefly reviewed the physics of high-energy neutrino interactions, this chapter will focus on the detector hardware and data-taking framework.

3.1 The IceCube Detector

The IceCube Neutrino Observatory consists of an array of 86 strings holding 5160 digital optical modules (DOMs) deployed between 1.45 and 2.45 km deep in the ice of the Antarctic Plateau at the geographic South Pole. It is the world's largest neutrino telescope, having instrumented about 1 km^3 of ice. The layout of IceCube is shown in Figure 3.1. Optimized to detect neutrinos above TeV energies, IceCube strings are separated by about 125 m, with DOMs vertically separated by about 17 m. IceCube's first string was deployed in the 2004–2005 season, and the full detector was completed in December of 2010, for a total construction time of seven austral summers. Physics data however was collected with each partial detector configuration (Figure 3.2). Two other components complete the observatory: *DeepCore* and *IceTop*. DeepCore is an infill of eight denser strings in the deep ice, enhancing IceCube sensitivity at neutrino energies < 100 GeV. DeepCore physics goals include searching for dark matter and studying atmospheric neutrino oscillations [117]. DeepCore string spacing is 70 m, and they are located at the bottom of the IceCube detector, where the ice is especially clear. DeepCore DOMs vertical spacing is about 7 m. IceTop on the other hand is located at the surface, and is devoted to cosmic-ray physics in the 10^{14}-10^{18} eV energy range [118]. It consists of 81 stations, each of which made by two tanks equipped with optical sensors frozen in water (the detection principle is thus analogous to the in-ice component). IceTop is also used as a calibration instrument and can be used as veto against cosmic-ray background for the in-ice detector. The IceCube building block is the DOM (Figure 3.3). A pressurized 13 mm thick glass sphere contains a downward looking 25 cm Hamamatsu
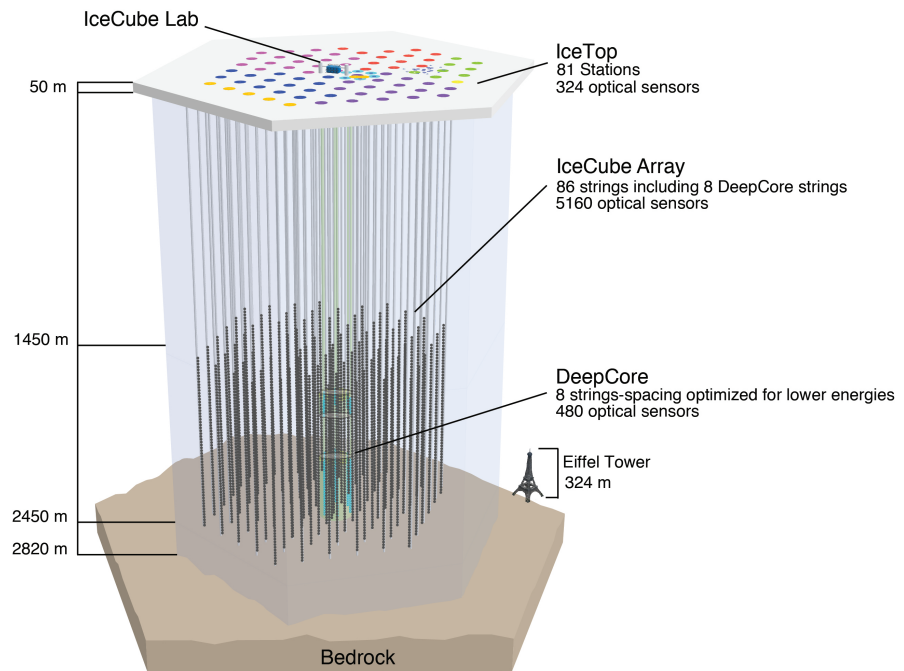
Fig. 3.1.: Sketch of the IceCube detector.
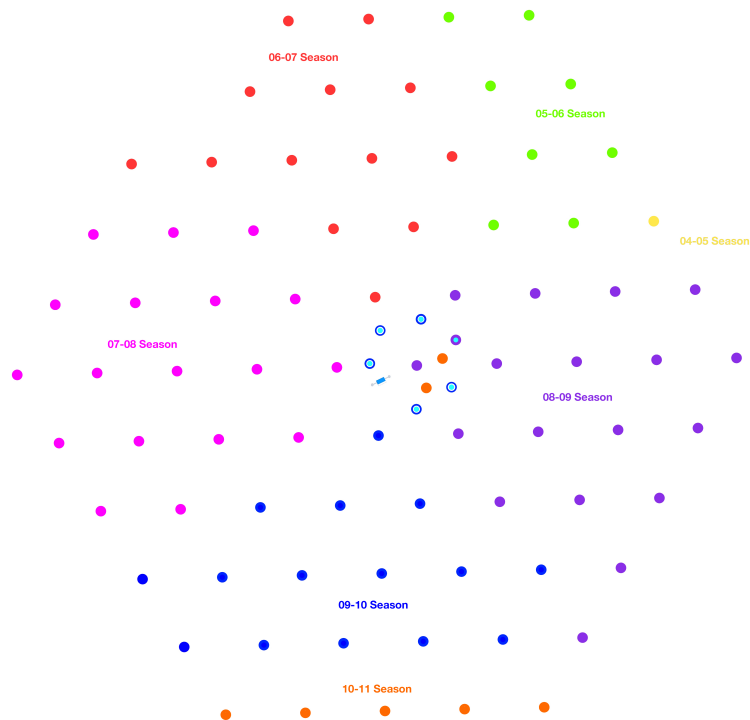
Fig. 3.2.: IceCube construction occurred over seven austral summers, and physics data was taken with each partial configuration.
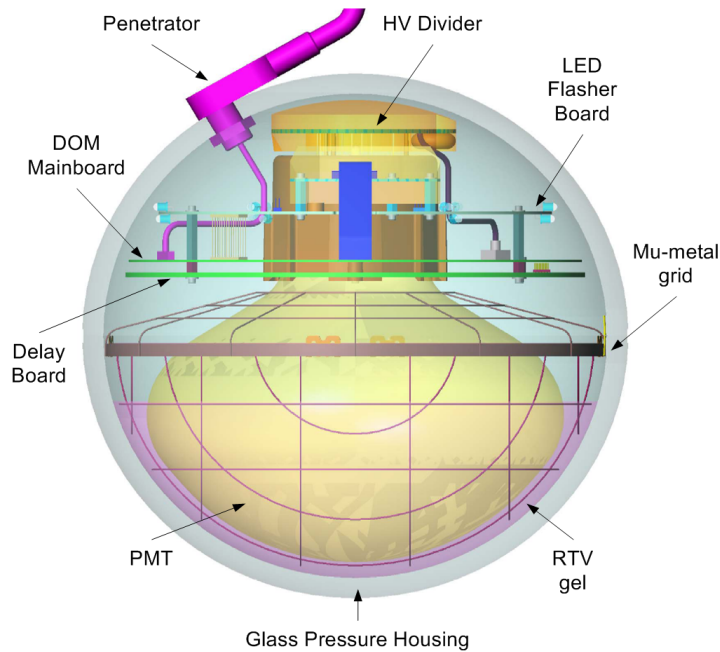
Fig. 3.3.: Schematic view of the digital optical module [119].

photomultiplier (PMT) whose main purpose is to detect the Cherenkov radiation produced by charged particles in the ice. The PMT is supported by a coupling gel and surrounded by a μ-metal grid to shield it from the terrestrial magnetic field and improve the PMT efficiency [120]. These PMTs have been selected because of their low dark noise and excellent timing and charge resolution for single photons. The dark count rate at low temperatures is close to 300 Hz in the $-40°$ C to $-20°$ C range of greatest interest for IceCube. For the in-ice detector, the PMT gain is set to 10^7 allowing the detection of individual photons with a signal amplitude of 8 mV (the photo-electron PE is defined as the resulting anode voltage level of a single photo electron after being amplified through all the dynodes in the PMT) which is well above the digitizer precision and other electronic noise levels (both ~ 0.1 mV). The quantum efficiency of a standard IceCube PMT has a value around 0.25 for wavelengths near 400 nm, while most of the modules in DeepCore have an enhanced quantum efficiency to further help in detecting low energy events. The spheres have been designed in order to stand pressures up to 650 atm, achieved during the freeze-in process after the deployment. It goes without saying that the entire detector, once deployed, is not accessible and no maintenance is possible on IceCube DOMs. The reliability requirement was set to a 90% DOM survival after 15 years of operations. As of 2016 only 87 DOMs have failed and 5397 of the 5484 deployed DOMs (98.4%) are operating [121].

While the lower part of the pressurized sphere is occupied by the PMT, the upper part houses the electronics. The main elements are:

- DOM Main Board (MB), to process, digitize locally the signal, packetize it and communicate it to the surface

- LED Flasher Board, used for calibration purposes

- Delay Board that buffers the signal up to 75 ns

- A 2 kV High Voltage (HV) supply to power the system

A single twisted copper wire-pair, through the penetrator, connects each DOM MB to a cable that runs up to surface to the IceCube Laboratory (ICL), where data are transmitted on demand.

3.2 Antarctic Ice Properties

In Chapter 2, neutrino interaction processes in the ice were described. The Antarctic Plateau offers a unique environment where to perform neutrino physics experiments: a roughly three kilometer thick ice shelf provides scientists not only with a huge quantity of medium that would have never been possible to achieve artificially, but also with an extremely high quality one. Antarctic ice properties are of critical importance for the IceCube science goals: event reconstruction and simulation heavily rely on their detailed knowledge. The combination of scattering and absorption effects in the ice contribute to the largest uncertainty in IceCube's neutrino searches.

As reported in the previous section, DOMs are equipped with a LED Board. LEDs emit light at 399 nm, wavelength chosen appropriately to mimic the natural Cherenkov radiation IceCube is interested in. In order to investigate wavelength-dependent effects, among the 5160 DOMs in the detector, 16 are equipped with 350 nm, 370 nm, 450 nm and 500 nm LEDs [122]. *Flasher runs* (Figure 3.4) are specific data taking runs when the LED light is used: by measuring the arrival time distributions of photons at different distances from the light source, it is possible to measure both the attenuation and scattering length of the light. Photons are absorbed by electron or molecule excitations, and deflected by trapped air bubbles, dust particles and ice crystal defects. Among many achievements, *flasher runs* have resulted in a detailed ice model, SpiceMie [122], where SPICE stands for South Pole Ice and Mie refers to the theory of electromagnetic radiation scattering off small particles which was first treated by Gustav Mie [123]. In this model, the ice is described by a table of depth-depended parameters $b_e(400)$ and $a(400)$ related to scattering and absorption at 400 nm respectively, together with a depth-dependent temperature and by six global parameters fitted to the flasher run data. A detailed description can be found

Fig. 3.4.: *Flasher run dataset*: a flashing DOM emits photons, which propagate through ice and are detected by other DOMs. Picture from [122].

(a) **(b)** **(c)**
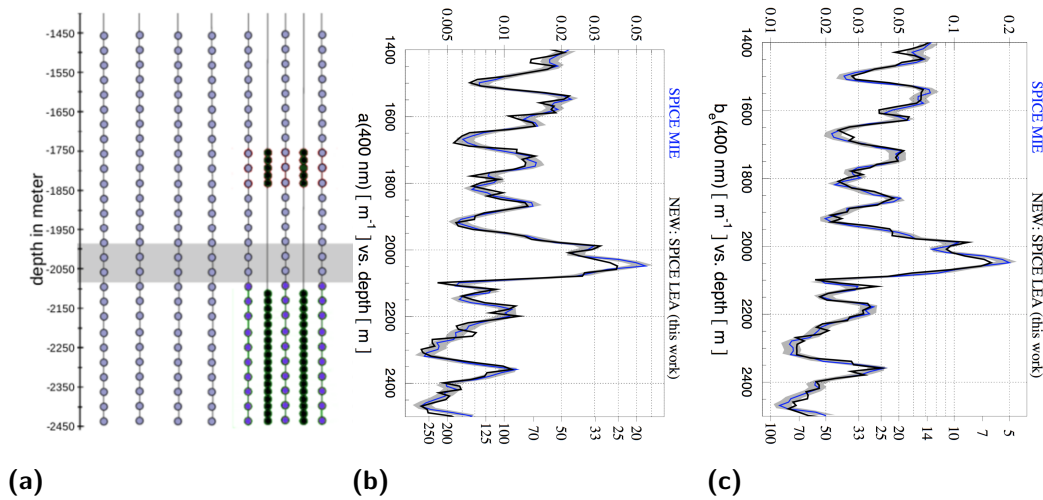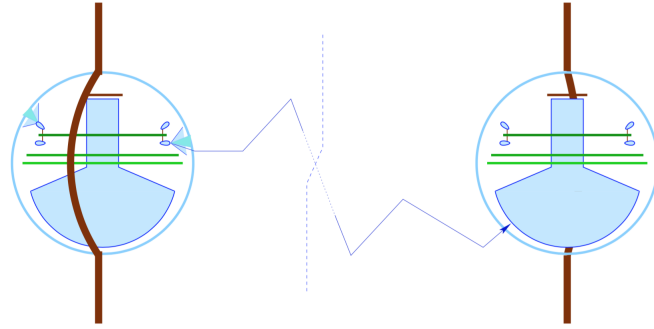
Fig. 3.5.: From the left to the right: a) side view of the IceCube detector, with the dust layer hilighted with a gray band; b) and c) the absorption and scattering coefficients (a and b_e respectively) for the SpiceMie and SpiceLea ice models [122, 124]. The grey band added to the SpiceLea ice model corresponds to $\pm 10\%$ combined statistical and systematic uncertainty [124].

in [122]. The baseline SpiceMie model assumes that the South Pole ice is isotopic in azimuth. Further studies on recent IceCube flasher data indicate however a slight azimuthal dependence of ice optical properties [124]. An updated version of the SpiceMie model accounting for the ice anisotropy was made in 2013, with the name SpiceLea [124]. Figure 3.5 shows South Pole ice optical properties from SpiceMie and SpiceLea models. By looking at the top axes of the plots, which display the absorption and the scattering at 400 nm, one notices that the ice gets clearer at the bottom of the detector. Moreover, the formation history of the glacial ice results in complex optical properties with a layer structure that causes the peaks in the absorption and scattering coefficients. The ices shelf grows at a rate of about 2.5 cm/year from the precipitation of very small ice crystals that formed due to the very low humidity. The snow density increases with depth due to pressure until it reaches its maximum at a depth of around 200 m. With increasing depth and pressure, air bubbles close off and get smaller, while at the same time the crystal size is growing. At around 1400 m and below the pressure is so high that these trapped air bubbles

turn into hydrates [125]. These air-ice clathrates have nearly the same index of refraction as the surrounding pure ice, and they do not cause Cherenkov photons to scatter as they pass through. This is the main reason why IceCube sensors are deployed at depths of 1500-2500 m. The prominent feature in correspondence with the grey band in the drawing is the so called *dust layer*, likely indicating evidence of a volcanic eruption [126]. As much as it is possible to understand from Figure 3.5 why IceCube sensors have been placed so deep in the ice, it is also possible to perceive that the horizontal string spacing of $\sim$ 125 m is motivated by the average value of the absorption length, which is indeed $\sim$ 125 m. The average scattering length is $\sim$ 20 m.

Finally, the last effect that is taken into account arises from the actual string deployment. The procedure consists in drilling a 60 cm hole in the ice down to $\sim$ 2500 m using a hot-water drill. The hole remains water-filled, being the water essential to sustain the ice pressure and avoid the column collapse. The water at the edges starts immediately to refreeze, and it takes about 30 hours until everything is frozen again, leaving however a not pure ice as the surroundings. Recent observations with a video camera deployed deep in the hole show evidence that as the hole refreezes from the outside inward, bubbles and impurities are forced into the very center. This forms a narrow column of impure ice, 5–10 cm wide, where the scattering length becomes small. This is called the *hole ice* effect [122], and it is accounted for by empirically modifying the effective angular sensitivity of the DOM, as shown in Figure 3.6.

3.3 Data Acquisition (DAQ)

Neutrino detection in ice was pioneered by the AMANDA collaboration in the late 1990s [127]. Completed in 2000, it was continuously operated until 2009 when the IceCube detector took over. Despite being a very successful experiment, its limits were clear almost from the beginning: the detector was too small, required manpower-intensive calibration efforts and, above all, the analog transmission of the signals to the surface degraded the resolution. Several approaches were tried, but the most attractive and yet most difficult was the one that solved the problem: the digitization of the signal would occur directly at the DOM level. Digitization is the first step of the IceCube signal path. After having decided if the signal is worth to be digitized, the DOM sends it to the surface, where a complex series of procedures is set up to reduce the rate: it is not possible nor desirable to read out and send all the information produced by the PMT, since it would mostly contain noise. The concepts of triggering and filtering are therefore needed and will be introduced in the following sections.
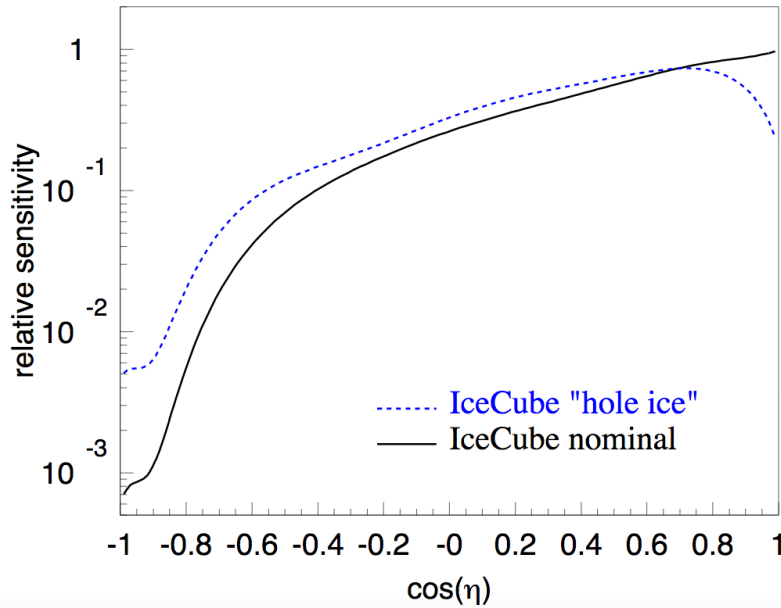
Fig. 3.6.: Angular sensitivity of an IceCube DOM where η is the photon arrival angle with respect to the PMT axis. The nominal model, based on a lab measurement, is normalized to 1.0 at $\cos\eta = 1$. The area under both curves is the same. Figure taken from [122].

3.3.1 An IceCube *hit*

Before discussing further the digitization chain in IceCube, it is important to define the most fundamental unit of the IceCube data, the *hit*. Whenever the anode voltage of the PMT exceeds the 0.25 PE threshold, one or more photons are detected and the waveform digitization is initiated. This trigger will be called a Hit or DOMLaunch. As a reminder, one photo-electron or PE is defined as the anode voltage level that a single photo-electron holds after being amplified through all the dynodes of the PMT. Considering a nominal gain of 10^7 for in-ice DOMs, this value is about 8 mV.

Without any further constraint applied, most of the hits are due to dark noise, i.e. effects that lead to the emission of an electron from the cathode of the PMT in the absence of a photon source external to the DOM. Dark noise is a complex phenomenon with numerous possible sources, including thermionic emission, electronic noise, field emission within the PMT, Cherenkov light from radioactive decays, and scintillation/luminescence in the glass of the PMT and pressure sphere [121]. Therefore, further conditions are set to reduce the data and identify only the real neutrino event signatures. Principally the data flow sent to the surface is limited by requiring neighboring channels to have coincident hits within a certain time window (given that real physics hits tend to be coincident in spacetime while random PMT noise hits are isolated) or by minimizing the waveform information contained in a hit.
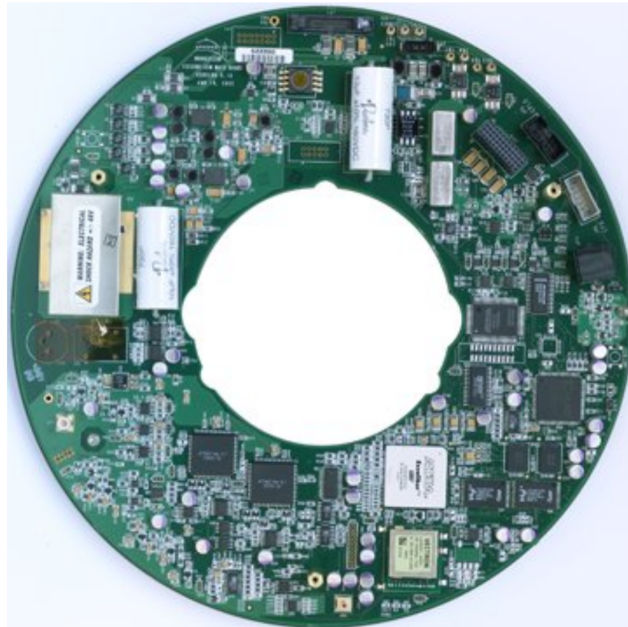
Fig. 3.7.: A photograph of the DOM MB taken from [128].

Hit information sent to the surface always contains at least a timestamp, a coarse measure of charge, and several bits defining its origin [128].

3.3.2 DOM Main Board (DOM MB)

In the broadest sense, the primary goal for IceCube DAQ is to capture and timestamp with accuracy the complex, widely varying signals over the maximum dynamic range provided by the PMT. Information such as the digitized waveforms, the timestamp, the DOM physical position in the array, are provided by the DOM MB. Indeed, the DOM MB (Figure 3.7) houses the waveform digitizers, the on-board computer, communications circuits, the high voltage supply and many other components.
There are two types of digitizers on the DOM MB. One is the "Analog Transient Waveform Digitizer" (ATWD), and the other is the "fast Analog to Digital Converter" (fADC). Two identical ATWD are placed on each MB, and are operated in a ping-pong fashion. When triggered, the ATWD quickly stores 128 samples of waveform (sampling the analog voltage at 300 MHz) then digitizes these with the internal ADC. During the digitization period, the ATWD is disabled, so a second one is provided to avoid losing additional hits and thus minimizing the deadtime. The number of capacitors storing the waveform and the sampling rate translate into a maximal waveform length of 426 ns in 3.3 ns wide bins.
The second type of digitizer, the fADC, samples at a lower rate of 40 MHz and the sampling time window is configured to be 6.4 μs, corresponding to 256 samples per acquisition. Another unit is used to indicate the quantity "samples per seconds" or SPS. The ATWD is thus running at 300 MSPS, while the fADC at 40 MSPS.

Fig. 3.8.: Block-diagram of the DOM MB components taken from [128]. The adjustable threshold of the Trigger at the upper left of the circuit determines how big has to be a signal to trigger the detector, the LC logic (described in later sections) decides if the captured ATWD samples should be transmitted to the surface. There are two ATWDs in the circuit, one acts as a backup digitizer to capture signals while the other one is busy digitising. The Field Programmable Gate Array (FPGA) initiates the actual digitization, communicates with nearby DOMs and the surface. The CPU controls the FPGA, handles data transport, tests and monitors the system.

Fig. 3.9.: ATWD and fADC digitized waveforms of a PMT hit. The ATWD provides 3 amplification channels with the bin content being either 16×, 2× or 0.25× the original.

On the upper left part of Figure 3.8 the analog signal produced by the PMT is split into different paths at the input of the MB. The upper path, with the variable discriminator, is for trigger purposes: the threshold set determines how big has to be a signal to trigger the detector. In the middle path, the signal is physically delayed for 75 ns by going through the delay board and then split again in three paths that are differently amplified (×16, ×2, ×0.25) before feeding three different channels of the two ATWDs. Since each channel of the ATWD has only 10 bit resolution, it is not capable alone to cover the entire dynamic range of the PMT, from small to large waveform, thus three different channels are needed. In the third path the signal is amplified by ×2.6 and right after by ×9 and sent to the fADC (in the block diagram labeled "PMT ADC") so that information from longer physics signals is kept (at a lower resolution of 25 ns instead of ∼ 3 ns).

Figure 3.9 shows an example of waveforms from the three ATWD channels at different gain and the fADC channel. ATWD channel 1, with a x16 amplification and good for small waveforms, is digitized first. Then channel 2 (×2) is digitized if any bin in channel 1 exceeds 768 counts. Channel 2 is good for medium waveforms. Channel 3 (×0.25) is digitized only if any sample in channel 2 exceeds 768 counts. Channel 3 is needed for large waveforms. The fADC is a slower digitizer to cover the case of longer waveforms.

Fig. 3.10.: Schematic demonstration of two HLC in the center and two SLC on the sides. Colored circles represent hit DOMs, and blue circles represent unhit DOMs. LC conditions, hard or soft, always occur between DOMs on the same string. LC conditions are met in four occasions: the hit DOM pairs being nearest or next-to-nearest to each other. If this happens within 1 μs, these hits are flagged as HLC hits, *Hard Local Coincidence*. Hits that do not satisfy this condition are called SLC, *Soft Local Coincidence*, despite no coincidence is actually present.
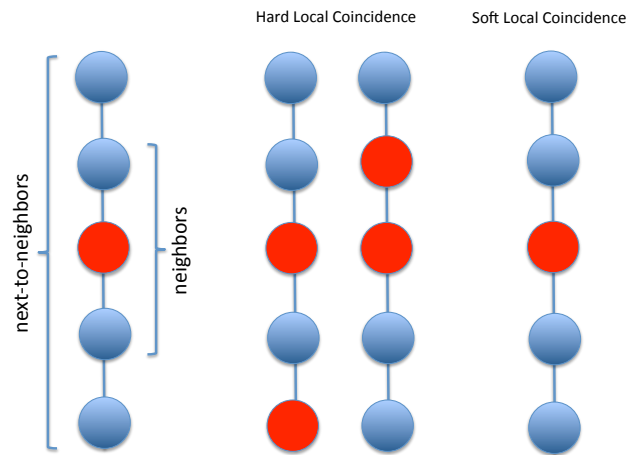
3.3.3 Local Coincidence

While each optical module is capable of detecting and recording signals independently, it is connected to its immediate neighbors on the same string, allowing communications between DOMs. This system is known as 'local coincidence' and it is used to suppress uncorrelated noise signals, avoiding the readout of noise data. As seen in Figure 3.8, the Local Coincidence (LC) logic decides if the captured ATWD samples should be transmitted to the surface or not, limiting the data flow from DOMs to the surface. Two LC modes are employed in IceCube signals: *Hard Local Coincidence* and *Soft Local Coincidence* (Figure 3.10). If the discriminator threshold is passed, digitization begins on both the high- and low-frequency digitizers (ATWD and fADC): if within a ± 1 μs window a message is received from the neighboring or next-to-neighboring DOMs, the HLC condition is met and a full waveform is stored and transmitted to the surface. If, however, no local coincidence signal is received the high-frequency digitization process is aborted, and only 16 samples of the 256 are recorder from the fADC. Of these, only the three largest ones are transmitted to the surface, and used for more sophisticated noise cleaning methods later in the data processing, giving information about the low energy events with minimal increase in the total data rate.

3.3.4 Trigger Algorithms

The DOM single photon electron (SPE) scalar rate is about 500 Hz. In comparison, the ATWD launch rate is 5-25 Hz, depending on the DOM height in the ice [129]. With more than 5000 DOMs this still represents a tremendous amount of data to be stored and transmitted. It is thus necessary to add a more sophisticated logic to
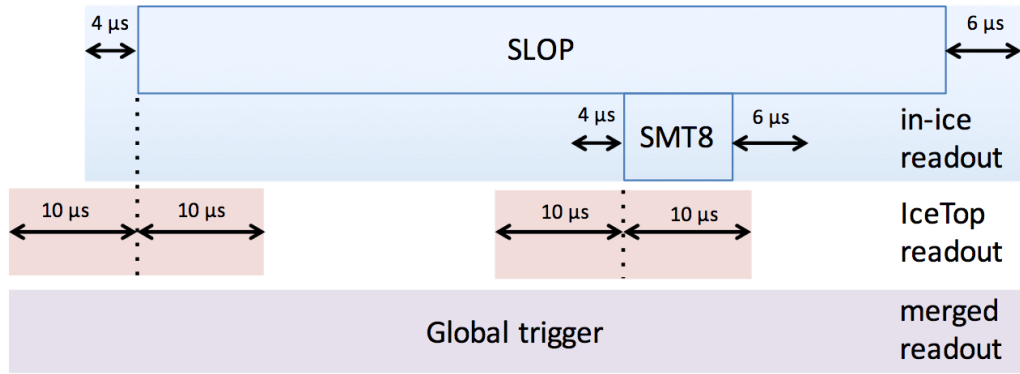
Fig. 3.11.: In-ice, IceTop, and merged readout windows for a long SLOP and SMT8 triggers [121].

establish which data are more likely to be associated with physics events. A system of 'triggers' has thus been implemented and is running on the DOMHubs (computers) at the IceCube Laboratory (ICL). The IceCube trigger algorithms generally look for a certain multiplicity of HLC hits within a given time window, where the scale of the trigger window is set by the relevant light travel time in the ice. Longer readout windows are appended before and after the trigger window to capture early or late light. Some trigger algorithms use additional requirements on the geometry of the hits. Triggers can be assigned to operate on different "DOM sets", such as all in-ice DOMs, DOMs within the DeepCore sub-array, or IceTop DOMs. Trigger algorithms run in parallel over all hits in the DOM set, and then overlapping triggers are merged [129]. The most important trigger for this analysis is the Simple Multiplicity Trigger, SMT8. The SMT looks for *N* (eight in this case) or more HLC hits within a sliding time window of several μs, depending on the different DOM set considered (in-ice, DeepCore or IceTop). The in-ice SMT trigger is an SMT8, which thus requires eight DOMs to have HLC hits within a 5 μs time window. Other triggers are running at South Pole, each aiming in finding patterns that look interesting for a specific analysis, such as the SLOP, Slow Particle trigger, developed for slow track-like particle signatures as the ones expected from magnetic monopoles [130]. During a physics event, many triggers may fire in sequence and overlap each other. Each trigger has defined readout windows around the trigger window, depending on the DOM set involved, if In-ice or IceTop DOMs; all hits (including SLC ones) from the full detector are read out and built into events. The union of overlapping readout windows defines an event; an example is shown in Figure 3.11. For the DOM set involve in the trigger, the readout windows are appended to the trigger window, while for the other DOM sets the readout window is centered on the trigger start time.

IceCube uses an internal framework called *icetray* to process detector data [131] . Events are stored in abstract digital objects, called I3Frames. There are two central
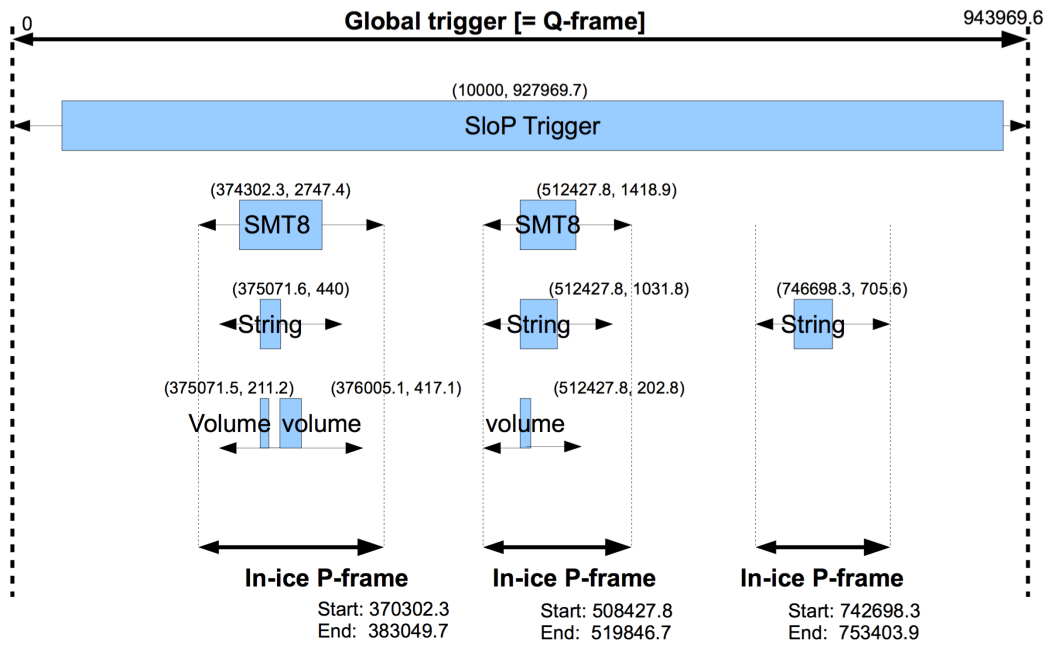
Fig. 3.12.: Schematic diagram showing how Q and P frames are handled in icetray. Image credit J. Kelley.

types of frames representing the events in IceCube: DAQ (Q) frames and Physics (P) frames. The former stores a complete detector readout during the period of a global trigger, which can consist of many subtriggers (Figure 3.12). On the other hand, P frames should contain exactly one subevent each, which has been extracted from the Q frame by an event splitter. The Q-P splitting is not the reverse procedure of the data acquisition scheme, because the splitters use the physics of track and cascade signatures to identify subevents, procedure more sophisticated than DAQ triggers.

3.4 Online and Offline Processing

Triggers described in section section 3.3.4 build up a first raw selection of data of possible events in the detector. All triggered data are stored on hard drives, but this raw output is almost 1 TB/day (the vast majority of this being cosmic-ray muons) and the satellite bandwidth allocation for IceCube is 105 GB/day. Since flying the hard drives out is not always possible, especially during the six months austral winter, it became quickly clear that an *online filtering* process was needed to look for interesting events. Online filtering is not only able to reduce the amount of data and send them over satellite, but also to trigger other experiments for near-real-time follow-up. Triggers happen at a kHz-rate, forming the detector readout and stream of events at Level 0.
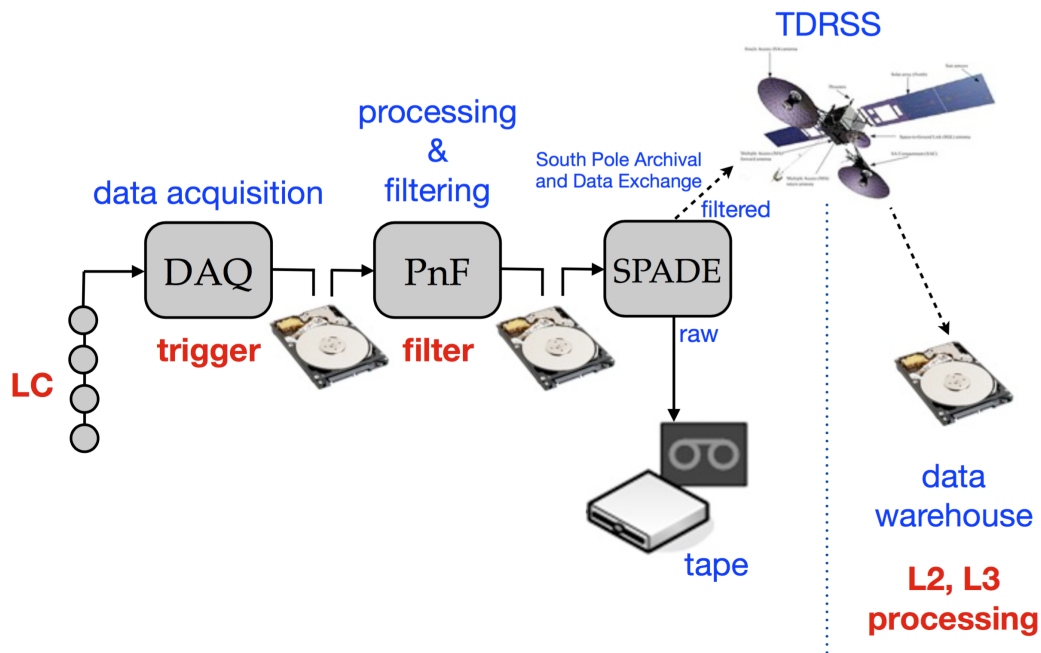
Fig. 3.13.: Schematic diagram showing the data flow from LC hits to the data warehouse up in the North. Tapes have now been substituted by hard drives. Image credit J. Kelley.

The *online processing* is also referred to as TFT: Triggers, Filters & Transmission according to the three major components data pass through before analysis. An overview of the complex flow of the data in IceCube is given in Figure 3.13. In the filtering process the triggered events are subjected to a series of operations similar to an offline physics analysis. This involves, in sequence: removal of known bad DOMs, pulse extraction, (trigger-based) event splitting, noise-cleaning and a basic set of reconstructions (online processing cannot be highly computationally expensive). The so treated events are then subjected to filters, each with a different scientific goal. Some of these are: Muon filter, Cascade filter, Low(-energy)Up(-going) filter, Extreme-High-Energy (EHE) filter, DeepCore (DC) filter, starting-event filter, IceTop filter. The most important filter for this analysis is the **Muon Filter**, that selects events compatible with a muon track-like signature. It relies on two main reconstructions, LineFit and PoleMuonLlh. LineFit assumes that a plane wave describes the light pattern, and tries to fit a line through all the DOMs that have detected light. PoleMuonLlh is a one iteration likelihood fit that uses LineFit as a seed. If an event is selected by any filter, the event itself and its Q-frame are selected for transmission via satellite. From $\sim$ 2.8 kHz of triggered events, filtered events rate is reduced to roughly 550–800 Hz. Filter level selection is referred to as Level 1.

The *offline processing* includes all further data treatment in multiple processing levels, from specific event selections up to the analysis level. Because offline processing is (almost) not limited in computational resources as the online processing is, more

complex and computationally expensive algorithms can be used. The event selection and processing of a specific analysis can involve many further levels of cuts and event treatment, reducing the event sample. For neutrino analyses the experimental data needs to be typically reduced by a factor 10^5–10^6 to reach a sample of pure neutrino events at a rate in the mHz-range.

3.4.1 Reconstructing Particle Directions and Energies

Despite the really broad spectrum of scientific goals and analyses conducted in IceCube, they all need to discriminate the signal from the vast majority of background events collected. For the particular case of the extended sources analysis treated in this work, signal represents a track-like event, signature of the interaction of an astrophysical neutrino, with specific properties: should have a high energy and an accurate angular resolution. Direction and energy are thus the two most important variables we are interested in, and the quality of their reconstruction affects strongly the analysis sensitivity. Track and energy reconstructions are required to have the highest resolution and the least systematic bias in the region relevant for the analysis. The following sections describe the reconstruction methods, which the event selections reported in Chapter 5 rely on, and final consideration on energy and angular resolution.

LineFit

LineFit is the most basic reconstruction algorithm used for muons in IceCube. Historically, this first-guess method performed a least-square fit to the location and time of each hit [132]. Using robust statistics techniques, this algorithm was modified by replacing the least-squares model with a Huber fit, improving the reconstruction accuracy by penalyzing outlying hits [133]. In this reconstruction the geometry of the Cherenkov emission is not taken into account, but considers the muon as a plane wave of light crossing the detector. Despite this large approximation being unphysical, the algorithm is extremely fast and results in a median angular resolution of few degrees. Improved LineFit serves as a seed track to the more complex reconstructions used in on site data analyses, as the likelihood ones described in the next section [133].

Fig. 3.14.: Parameters describing the DOM-track configuration [134].
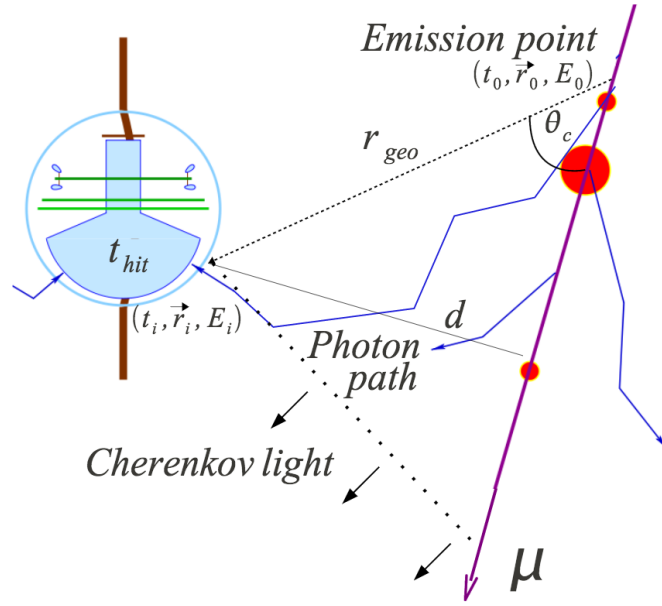
Likelihood-based reconstructions: SPE and MPE

First guess algorithms are very interesting from the computing point of view, given they are very fast (analytical solution) and can be used on large amount of data. However, more sophisticated methods are used to achieve a more accurate track reconstruction and rely on likelihood maximization (numerical solution). Two formulations of the likelihood are present in the IceCube processing chain, the single-photo-electron (SPE) and the multi-photo-electron (MPE), and both take into account the cone shaped emission of light and the absorption and scattering of photons in the ice [132]. The method of maximum likelihood is a well-known technique for estimating a set of unknown parameters $\vec{a}$ (the parameters describing the muon track, see Figure 3.14) from a set of observed experimental values $\vec{x}$ (photon arrival times and locations). Track parameters $\vec{a}$ are:

$$\vec{a} = (\vec{r}_0, \hat{p}, t_0, E_0) \text{ with} v \ \vec{r}_0 = (x_0, y_0, z_0) \text{ and } \hat{p} = (\theta, \phi) \tag{3.1}$$

Here, $\vec{r}_0$ is an arbitrary point along the track, t_0 is the time at $\vec{r}_0$, E_0 is the event energy at $\vec{r}_0$ and $\hat{p}$ is the track direction. Generally, no fit is performed directly for the energy, reducing the number of free parameters for track reconstruction to six. The LineFit algorithm uses the time of the first PE, without accounting for the effect of the DOM distance from the actual muon track, causing a spread in the PE timing distribution due to scattering. To account for this effect, SPEFit uses a Pandel Function to model the timing distributions more accurately. PMT jitter and potential negative time residuals from random noise in the detector are accounted for by convolving the Pandel function with a Gaussian [135]. SPEFit considers only the first photon in a DOM, assuming it is the least scattered and carrying the most

information. This is true by construction when only one photon is detected by each DOM. The alternate formulation called MPE uses the so called MPE-Pandel photon arrival time pdf, where the information about the number of recorded photons at each DOM is incorporated as well. The analytical expression for the photon arrival time PDF given by the Pandel function, which assumes uniform ice, fails to describe many of the ice features observed in data, including scattering and absorption lengths or the orientation and depth of the light emitting source. An improvement is reached by using a complete photon transport simulation using a depth-dependent ice model [122]. Photons are simulated for different muon-receiver configurations, and the resulting timing distributions and overall light yields are tabulated [136]. When the binning of the table is too coarse, binning related artifacts occur in the likelihood space. A finer-binned table would solve these issues, but the amount of storage and memory required for accessing the table makes the solution unfeasible. The alternative approach that has been found is to fit a multi-dimensional spline surface to the arrival time distributions from the detailed photon propagation simulation. This is done using the photospline package [137], which provides an analytical parametrization of the tabulated PDFs. These splines are now used as PDFs for the MPE likelihood (SplineMPE), and lead to an improvement of 26% in the median neutrino angular resolution at 30 TeV. Tables have been used for the event selections of IC40 and IC59, while from IC79 splines became the standard (Chapter 5). For more details on the light table production and photospline usage refer to [138].

Paraboloid fit

Whenever a track is reconstructed, it is important to associate an uncertainty to its direction. This parameter is used on one hand to help identifiying mis-reconstructed tracks, improving background rejection, and also as estimation of the point spread function of the detector, as specified in Chapter 6. The *paraboloid* reconstruction method [139] acquires such an estimate on an event-by-event basis, by analyzing the likelihood space around the minimum and fitting an elliptic paraboloid around the best fit point. The resulting one sigma confidence ellipse is represented by the axes σ_1 and σ_2, and the track uncertainty is calculated as:

$$\sigma_{paraboloid} = \sqrt{\frac{(\sigma_1^2 + \sigma_2^2)}{2}} \quad . \tag{3.2}$$

Good fits generally result in a narrow peak of the fitted paraboloid, having therefore a small $\sigma_{paraboloid}$, while bad reconstructed events present a broader minimum. The pull distribution is used to check the paraboloid performance, knowing an ideal angular accuracy estimator should be distributed around the true deviation from the Monte Carlo track. The result shows a systematic underestimation of the error

depending on the energy of the track, and thus paraboloid needs to be calibrated to correct for this effect. More details on the pull method and the paraboloid calibration are found further in the text in Chapter 6.1.

MuE and MuEX Energy Reconstructions

Up to now we have been discussing the several methods that allow to reconstruct the direction of a muon track. Direction is one of the two necessary quantities for the final level statistical analysis, and is mostly reconstructed using timing information. The other important quantity is energy, and its reconstruction relies this time on light amplitude. Two issues prevent the muon energy to be reconstructed precisely. The first one being the fact that most of the time the muon is not fully contained in the detector, leaving part of its energy unobserved. The second constraint is given by the very stochastic nature of the energy loss process, leaving possible to determine only the fraction of energy lost per path length, dE/dx (Section 2.2.2). The light yield of track-like events scales linearly with energy, allowing to compare the light yield at a certain DOM with the one expected at the same DOM under the hypothesis of a given reconstructed muon track and energy (template) [140]. The expected light intensity for a given template event can be approximated by:

$$\lambda = \Lambda E + \rho \quad ,$$

(3.3)

where Λ is the number of photons for the template, λ is the mean number of photons for an event with an energy E times the template one, and ρ is the noise hits. The likelihood for the MuE reconstruction method is constructed as follows:

$$\mathcal{L} = \prod_i \frac{\lambda_i^{k_i}}{k_i!} \cdot e^{-\lambda_i} \quad ,$$

(3.4)

where k_i is the number of photons detected at the ith DOM. This is maximized for the energy parameter E.

An improved version of the MuE algorithm is used for this work, dubbed MuEX. Here an additional function $G(\lambda_i, \lambda_j)$ is added to the probability density function in the likelihood to better model the systematic uncertainties on λ:

$$\mathcal{L} = \prod_j \int_0^{\inf} G(\lambda_i, \lambda_j) \frac{\lambda_i^{k_i}}{k_i!} \cdot e^{-\lambda_i} d\lambda_i \quad .$$

(3.5)

The definition of the $G(\lambda_i, \lambda_j)$ function can be found in [140]. The MuEX method achieves an energy resolution of 35% in $\log_{10} E$ for muon detector entry energy of 10^4 GeV, that corresponds to a 30% improvement in $\log_{10} E$ at 10^6 GeV with respect to the MuE algorithm.

Considerations on energy and angular resolution

The ultimate goal of a neutrino telescope as IceCube is to acquire information about the neutrinos that have interacted inside or in the proximity of its volume, and we have seen that the energy and the direction of the neutrino event are the two most important quantities we are interested in.

The amount of Cherenkov light in the detector is used as an energy proxy for the neutrino involved in the event, as more energetic events produce more secondary particles and more Cherenkov light. When electron neutrino cascades are fully contained within the detector, good energy resolution is possible. A less reliable energy estimation is also possible for muons. Energetic muons emit more light during stochastic energy losses, which appear as cascades along the muon track. However, few things should be kept in mind: on one hand, the muon stochasticity limits the energy resolution, as the number and intensity of stochastic losses within the detector volume is random and variable. Furthermore, the muon energy estimate is not strongly correlated to the primary neutrino energy, which is the interesting quantity. The energy estimate is instead correlated to the distance the muon has traveled before reaching the detector, which is generally unknown. Energy losses en route make the muon energy estimate a lower limit of the primary neutrino energy.

In the previous section we have learned that the angular reconstruction of the event is possible using the space-time pattern of Cherenkov light recorded by the array of optical sensors. Electron neutrino cascades are generally contained within less than 10 m (see Figure 2.5). This is short, compared to the scale of neutrino telescopes and the full Cherenkov light is created locally. Although these cascades are asymmetric, they appear rather spherical due to photon scattering, and therefore the direction of the primary neutrino is reconstructed poorly. In contrast, TeV muons typically pass through the detector, creating tracks with a large lever arm for accurate reconstruction. The muon track is offset from the primary neutrino track by a median angular deviation parametrized by [141]:

$$\Delta\psi = 0.7° \times \left(\frac{E_\nu}{TeV} \right)^{-0.7} .$$

(3.6)

Summary of Part I

The earth is constantly being bombarded by subatomic particles that can reach energies far higher than the largest man-made particle accelerator. These particles are known as cosmic rays (CRs). Almost 100 years after their discovery, their origin is still not clear. The cosmic-ray spectrum was introduced in the first Chapter of this work, and the connection between cosmic rays, gamma rays and neutrino was presented. By combining the information from all the known cosmic messengers, multi-messenger astronomy hopes to finally shed some light on the cosmic-ray production and acceleration mechanisms. The most promising sources of cosmic rays and neutrinos were presented, together with the limits on their detection from gamma-ray instruments and neutrino telescopes as ANTARES and IceCube.

The idea that neutrinos are ideal astrophysical messengers emerged soon after the particle was first detected: neutrinos are tempting cosmic messengers because they can provide crucial information about the *in situ* physical conditions of the sources, as they are unaffected by intervening scattering processes. Interactions with the Cosmic Microwave Background impose strong limits on the propagation of high energy photons, protons, and nuclei, while neutrinos allow us to look farther back in space. The second Chapter presented neutrino interactions in the ice and neutrino events signature in the IceCube detector, together with the Cherenkov radiation. Moreover, the backgrounds for astrophysical neutrino detection were introduced, with a short introduction on coordinate systems.

The first part concluded with the description of the IceCube detector. The digital optical module (DOM), the fundamental building block was introduced, together with a brief overview of the ice properties. The data acquisition system of IceCube was then presented. This included the digitization of the waveforms and the triggering logic, local coincidence and transmission of data. Finally, few offline reconstruction methods for track directions and energies were presented.

Part II

Search for Extended Sources with the
IceCube Neutrino Observatory

Overview of Part II

The second part of this work is dedicated to the search for extended sources with 7 years IceCube throughgoing muon data. After briefly recalling why such a dedicated search is important, in Chapter 5 we introduce the samples used in this analysis, highlighting their important properties as angular resolution and effective area. The analysis method, an unbinned maximum likelihood, is then introduced in Chapter 6. The building blocks of the likelihood are presented, that is the probability density functions for signal and background. Modifications to the standard point source tools are highlighted. The first one is the extension of a possible neutrino source, parameter that enters the likelihood in the spatial part of the signal probability density function. Because the extensions are not always known *a priori*, five different extensions have been considered, from $1°$ to $5°$. The second modification is related to the likelihood expression itself. After the detection of a serious issue in the background test statistic distributions, the method has been improved by accounting for signal contamination in the background estimation. The results of the analysis are finally presented in Chapter 7: five different skymaps, one for each extension considered, have been produced, to test whether data are better described by a background-only hypothesis or by a mixture of signal plus background. All the five maps are consistent with the background-only hypothesis.

Physics Case

<div style="text-align: right">4</div>

Motivations for searching for extended sources are manifold. As seen in Chapter 1, extended sources have been detected in the γ-sky. For example, the H.E.S.S. survey of the inner part of the Galactic Plane [142] revealed a number of bright extended γ-ray sources. If the observed γ-rays are produced by cosmic-ray interactions, a very-high-energy neutrino flux should be associated as well. If detected, this would represent an unambiguous proof of the hadronic nature of the sources. Despite many γ-ray sources show an extension of about $0.3° - 0.4°$, which is below IceCube's median angular resolution of about $1°$ at 1 TeV, some sources show even larger extension, thus providing a strong motivation to look for extended sources.

The high-energy cosmic-ray sky shows also clear indications for extended structures: although being at larger scales and higher energies, the Telescope Array has observed a 5.1σ pre-trial excess in cosmic rays with energies above 57 EeV in a region centered on coordinates 146.7° RA, 43.2° DEC [106], hotspot larger than the extension expected by propagation effects. The post-trial significance of this hotspot is 3.7×10^{-4} (3.4σ) [106]. In addition, the Kascade Grande experiment has observed at 5.5σ significance a $1°$ extended 300 TeV cosmic-ray hotspot in a mainly isotropic sky [143].

Finally, motivation in favor of a dedicated extended source analysis can also be found in Figure 4.1. Assuming the presence of extended sources and modeling the signal injection according to their extension, this plot shows the discovery potential for an E^{-2} flux of the regular point source analysis method that relies on an unbinned likelihood maximization, compared to the one calculated with our extended source analysis, with the spatial extension properly accounted for. In this case, the same value used to simulate the spatial extension enters the likelihood calculation, showing that, when the correct source extension is used, the improvement can be substantial. A point source analysis risks to be blind in the presence of an hypothetical extended source.
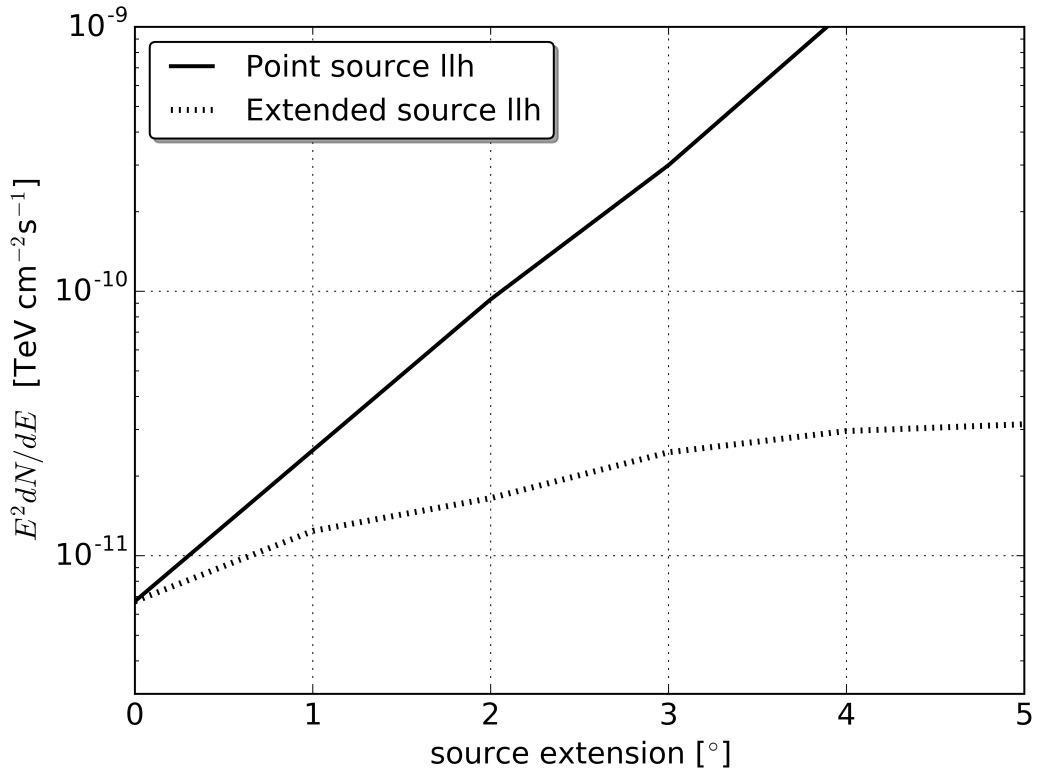
Fig. 4.1.: Discovery potential for an E^{-2} flux from an extended source at a declination of $16°$ for one year of IC86 data with no trial factor correction. The regular point source analysis (solid-line) is compared to the discovery potential of the extended source analysis using always the correct source extension (blue dots). The signal-subtracted likelihood is used (Chapter 6).

Point Source Samples

Since IceCube started taking data in 2007, the building block of a point source analysis, that is the selection of track-like events, has substantially improved. Over the years, analyzers have developed a well tested method and robust selection criteria that allow to produce a high quality sample of neutrinos from the northern and southern hemispheres. Since the first published results using the first year of data taken in partial detector configuration, IC22 [144], more years have been added and reconstruction techniques improved, both for the event energy and direction, leading to an improvement in sensitivity of more than an order of magnitude in the final published results [61]. Nevertheless, the backgrounds to consider and the main strategies applied to reduce them remain the same. From Chapter 3.4, one shall recall that the first-order background rejection of the online filter is not sufficient for high-level analyses, and other steps are required to reduce the total rate of detected events by roughly six orders of magnitude and obtain a final sample suitable for the final likelihood method. The process of building the optimal sample rejecting as much background as possible while retaining most of the signal is called event selection. The signal we are looking for is the clustering in space of those events that are believed to trace the interactions of high-energy astrophysical neutrinos. Recalling from Chapter 2, IceCube backgrounds are divided into two regions separated at a declination $\delta = -5°$. Thanks to its location deep in the ice, truly horizontal particles have to cross a substantial amount of ice before reaching the detector. In the northern sky (declination range $\delta \geq -5°$ or *upgoing* region in IceCube's coordinates), cosmic-ray muons are shielded by the Earth, and the main background is given by mis-reconstructed muons. These events originate from interactions in the atmosphere above Antarctica but appear as upgoing events due to a poor reconstruction. Being part of the reducible background, the event selection in the northern hemisphere is dedicated to the discrimination of well-reconstructed tracks from neutrino interactions against mis-reconstructed background. On the other hand, atmospheric neutrinos from the northern sky travel through the Earth without being absorbed and might interact near or inside the detector volume. For the 86-string configuration for example we expect $\sim 10^5$ atmospheric neutrinos per year, corresponding to an event rate of the order of the mHz. These events are part of the irreducible background, but follow a softer energy spectrum ($\sim E^{-3.7}$ for conventional or $E^{-2.7}$ for prompt component). In the southern sky (declination $\delta < -5°$ or *downgoing*) the Earth does not play any shielding role,

given there is only 1.5 km of ice above the detector. Many atmospheric muon events are indistinguishable from astrophysical neutrinos interacting in the ice above the detector, except for a small range of directions where the IceTop array can be used as veto. As the spectrum of atmospheric muons should follow an $E^{-2.7}$ spectrum, softer than the expected E^{-2} for astrophysical neutrino sources, an energy cut is applied to select preferentially higher energy events for the down-going sample. Quality cuts are also applied to distinguish atmospheric muon bundles form astrophysically-induced single muons. Since several muons are produced in the same shower event, atmospheric muons often enter the detector in bundles and would be reconstructed as a single track of higher energy. However, the light emission pattern for a single muon of higher energy differs from the one of a muon bundle, and the quality cuts rely on these energy deposition patterns to reduce the background. Classification of signal events from high statistics data sets is an ideal task for multivariate machine learning methods such as Boosted Decision Trees (BDTs) [145]. A BDT essentially synthesizes many cut variables with potentially complex relationships into a single, simple cut variable with very good signal/background separation, and the final sample at analysis level is thus obtained by applying a cut on this score. Starting from the IC59 sample, two different BDTs were trained (three for the IC79b sample [138]), one for each part of the sky and with different energy spectra, exploiting the substantial difference in the background of these regions. Training is performed using good quality signal events, typically with either an E^{-2} or $E^{-2.7}$ spectrum or both, while data is used for the background.

5.1 Characteristics and Performance of the Final Event Samples

The final point source samples used in this analysis are listed on table 5.1, together with the time period covered by each of them, the number of events selected and the reference to the published paper where more specific details on the event selections can be found. To compare the selection efficiency of different samples we use the *Effective Area* parameter, that can be calculated using the following event count formula:

$$N_\nu = T \int_{E_\nu} A_{eff}(E_\nu, \theta) \frac{d\Phi_\nu(E_\nu)}{dE_\nu} dE_\nu \tag{5.1}$$

where N_ν is the number of selected neutrino events in the sample, T is the livetime of the sample and $\frac{d\Phi_\nu(E_\nu)}{dE_\nu}$ is a given differential neutrino and antineutrino flux. This parameter expresses the surface area of a theoretical 100% efficient detector that would collect the same number of neutrinos as the real detector with the given event selection. The effective area depends on the detector performance and geometry and the event selection criteria. The effective area for the five different samples used

Sample	Start Date	End Date	Events	Livetime (days)	Reference
IC40	4/5/2008	20/5/2009	36 900	375.5	[146]
IC59	20/5/2009	31/5/2010	107 569	348.1	[147]
IC79b	1/6/2010	13/5/2010	93 737	315.5	[138]
IC86-I	13/5/2010	15/5/2012	137 707	332.6	[115]
IC86-II-III-IV	15/5/2012	18/5/2015	337 839	1057.5	[61]

Tab. 5.1.: Overview of the point source samples used in this analysis.

(a) Upgoing, declination range 30°, 90°

(b) Upgoing, declination range -5°, 30°

(c) Downgoing, declination range -30°, -5°

(d) Downgoing, declination range -90°, -30°
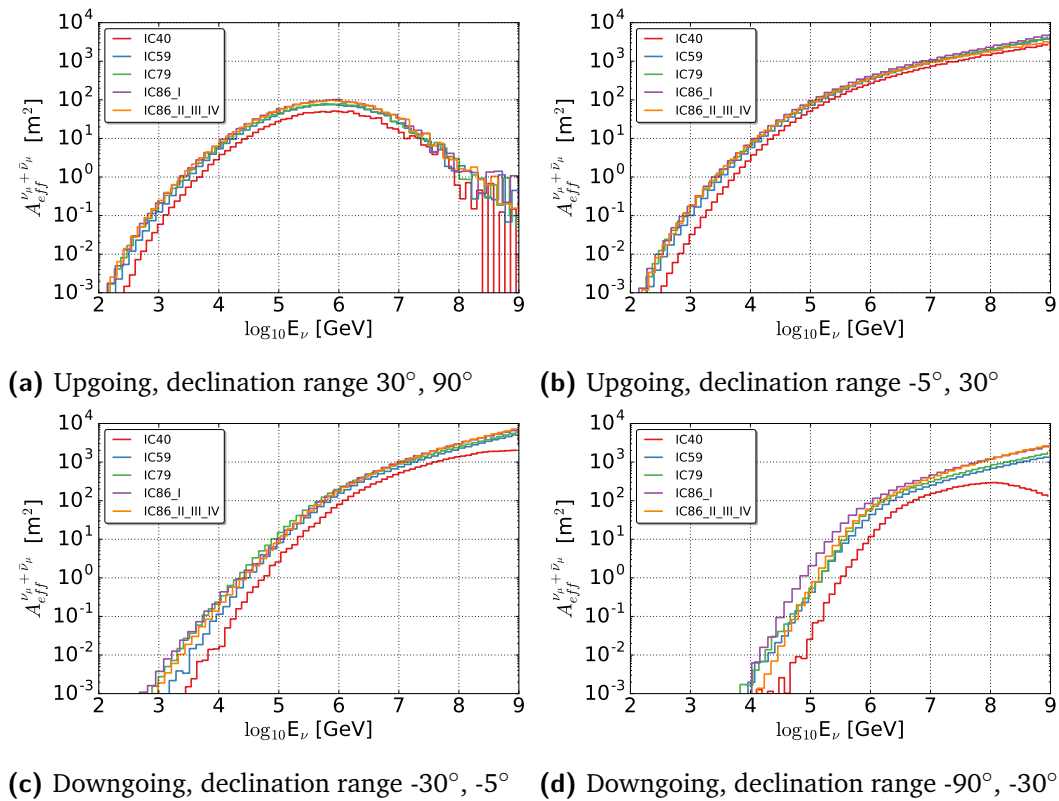
Fig. 5.1.: The average effective areas for a $\nu_\mu + \bar{\nu}_\mu$ of the point source samples as a function of the neutrino energy for different declination regions in the sky.
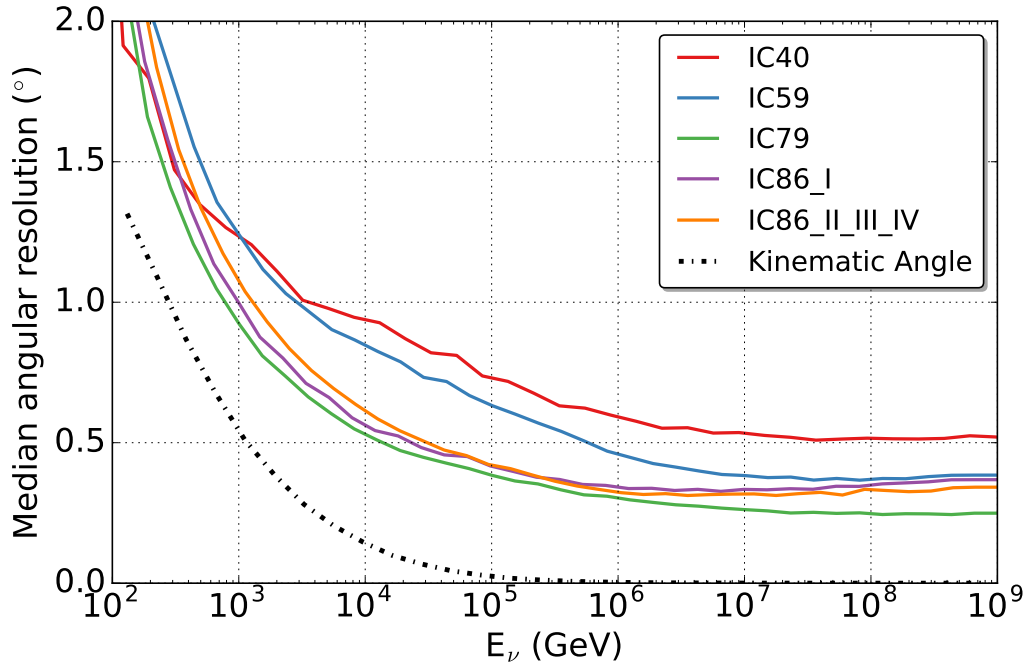
Fig. 5.2.: Median angular resolution (angle between reconstructed muon track and neutrino direction) as a function of the neutrino energy. The kinematic angle represents the angular separation between the Monte Carlo primary neutrino and muon true directions.

in this analysis is reported in Figure 5.1, for four different declination ranges. In the northern sky (Figures 5.1a, 5.1b), a lower energy threshold is achieved with respect to the south, and for nearly vertical upgoing events absorption becomes an important effect above 100 TeV (Figure 5.1a). In the southern sky (Figures 5.1c, 5.1d) the effect of the hard cuts on energy result in an effective selection only in the very high energy regime.

Effective areas however do not tell the whole story about the sample and do not give any information on how much background is included, hence on the purity and quality of the sample, nor do they reflect the point spread function of the selection. The statistical technique applied to the samples to search for extended sources relies heavily on this quantity, and the median angular resolution as a function of the energy for the five datasets is reported in Figure 5.2. Thanks to a tighter event selection, the IC79 reprocessed sample presents the best angular resolution. The slight difference between the IC86-I and IC86-II-III-IV samples is caused by differences in the simulation chain. The newer process uses different tools for noise treatment and includes coincident events, and the resulting angular resolution is worsened with respect to the previous release when using the same selection criteria. The difference between the IC79 and IC86_I samples, produced with the same IceSim release, originates from different event selection. The used datasets are sensitive to

TeV–PeV energy neutrinos in the northern sky, and primarily sensitive to neutrinos with energy greater than about 1 PeV in the southern sky.

As a final consideration on the samples performance, one should keep in mind that, despite being effective area and angular resolution important parameters for comparison, the ultimate quantity that should be compared is sensitivity, capable to include all the effects of detector, event selection and livetime and give the correct picture.

To summarize:

IC40: is the oldest sample used in this analysis, where almost half of the detector strings are missing. MPE is used as track direction reconstruction and MuE for the energy. The event selection is based on straight cuts on several variables. It is the sample with the worst angular resolution over 1 TeV [146].

IC59: few strings added with respect to the IC40 configuration, but still far from the full detector performances. Also for this dataset, the MPE and MuE track direction and energy reconstruction are used. Boosted decision trees (BDTs) [148, 149] are used for the first time for the event selection in the northern sky, while a straight cut on the reconstructed energy is used in the south.

IC79b: the reprocessed IC79 sample benefits from the SplineMPE reconstruction tool, which results in an improvement both for sensitivity and discovery potential with respect to the previous IC79 point source sample based on PandelMPE [138]. MuEx is used instead as energy estimator over the entire sky. Due to its tighter event selection, the reprocessed sample has the best median angular resolution distribution of all the samples considered in the analysis.

IC86-I: is the first sample with the detector fully completed. SplineMPE and MuEx are the reconstructions used here. Starting from the IC86-I sample, two separate BDTs were trained for the northern and southern hemisphere.

IC86-II-III-IV: during these three years no changes were made in the detector settings, simulation chain and online and offline softwares. Therefore they can be treated together as one single sample, and the MonteCarlo dataset is scaled to the livetime accordingly. Again SplineMPE and MuEx have been used. The downgoing selection is more restrictive, reducing the background by $\sim 50\%$ with respect to IC86-I, due to the better muon-bundle rejection [61]. The effective area of the sample is lower than the IC86-I one for vertical downgoing events in a declination band ($\delta = -90°$ to $\delta = -30°$) at low energies. This region was made more restrictive because of the existence of a dataset specifically

targeting the southern sky, the MESE sample [150], Medium Energy Starting Events, which covers this area more efficiently with far less background. The MESE dataset has not been included in the analysis since its impact in an extended source search is little.

5.2 Simulation

The capability of simulating the detector response both to muons and neutrinos is of vital importance for all IceCube analyses. Over the project lifetime, several scientists have build a complex chain of simulation tools that combines the knowledge of the physics process, detector hardware and calibration, and delivers Monte-Carlo simulations of possible neutrino and cosmic-ray air-shower events observed by the detector.

Neutrino Generator [151], a modification of the ANIS package [152], simulates neutrino interactions to fit possible signals, using a weighting for the primary spectrum to match the signal one, assumed to be a power law. NuGen starts by sampling the neutrino energy from this power law spectrum with a given spectral index γ, picks a random point on the Earth's surface and propagates the neutrino through the Earth and/or the ice towards the detector volume. Neutrino interactions are then modeled stepwise, accounting for the Earth's density profile and neutrino-nucleon cross-sections. After each step, the survival probability of the neutrino is calculated. Interaction is then simulated or not according to this probability. To improve the efficiency of the simulation, a weighting scheme is used that forbids charged current interactions inside the Earth, as these can cause significant losses for the events at higher energies, and allows only neutral current and Glashow-Resonance interactions. A *PropagationWeight* is needed at each step to correct for this. When reaching a predefined volume around the detector, also called "detection volume", which scales with energy to account for the increasing muon range, NuGen forces the neutrino to a final interaction. An *InteractionWeight* parameter is needed this time to correct for this feature. Finally, to obtain the correct neutrino event rate inside the detector we need to account for the *PropagationWeight*, the *InteractionWeight* and the *detection volume*. Additionally, the generation energy spectrum might not be the desired signal one. NuGen combines all these factors into a single weight called *OneWeight* which makes it possible to weight simulation and match any desired flux model without having to deal separately with all the relevant factors mentioned above. It should be kept in mind that NuGen generates an equal number of neutrino and antineutrino events of the configured flavor.

The CORSIKA [153] software package is an efficient and widely-tested implementation of air-shower physics. The secondary muons and atmospheric neutrinos simulated with CORSIKA are the main sources of background to astrophysical neutrinos in IceCube, and these simulations are used to learn how to subtract these background sources.

To summarize, both simulation chains can be split for simplicity into three steps:

Event generation Physical models predict the primary particles created at the surface of the atmosphere or at the Earth, interpolating data from direct and indirect CR measurements or hypothesized astrophysical signals.

Propagation The primary particles are tracked through various media, such as the atmosphere, the Earth or the ice near the detector. Secondary particles produced in interactions during propagation are tracked. Muon Monte Carlo (MMC, [112]) propagates the particles in the ice, simulates the energy losses and calculates the photon yields. Photons are finally propagated through the ice until they collide with a DOM. In the simplest case, lookup tables that give the probability of a photon arriving at a certain DOM given a certain position and direction are used.

Detector response The PMT and detector components response to the Cherenkov light is simulated in detail. A noise model is used to add noise hits and the full chain of coincidence and triggers is then applied as for real data.

Analysis Method

<div style="text-align:right">

6

</div>

The analysis applies an unbinned maximum likelihood method to the through-going muon dataset to look for a localized, statistically significant excess of events above the background, taking into account the possible extension of the source. This is an all-sky and time integrated search. Since source extensions are not known a priori, five different extensions have been considered, from $1°$ to $5°$. Besides few differences, the method follows that of [154]. With respect to a binned analysis, the unbinned method allows to include the detector angular resolution on an event by event basis to help discriminating between the spatial distribution of signal and background. Moreover, since background and signal have also different energy spectra, the energy is added to the probability density functions (PDFs) to increase the discrimination power. The two parameters we maximize for are the strength n_s or number of signal events and γ, the spectral index of a potential source located where the likelihood is evaluated. In this chapter we first describe the likelihood method and test statistic formulation, then discuss the observables the likelihood uses and finally the results.

6.1 Likelihood Method: the Standard Point Source Approach

For a data sample of N total events, the probability density of the ith event in the sample can be modeled as:

$$\frac{n_s}{N}\mathcal{S}_i + \left(1 - \frac{n_s}{N}\right)\mathcal{B}_i \quad , \tag{6.1}$$

where $\mathcal{S}_i$ and $\mathcal{B}_i$ are the signal and background probability density functions respectively, and n_s is the unknown number of signal events in the data sample under evaluation. As described in the previous chapter, the samples considered for this analysis are IC40, IC59, IC79, IC86-I and IC86-II-III-IV. To exploit the different spectral index between signal and background, as well as the different spatial distribution, both the signal and background PDFs contain a spatial and an energy term.
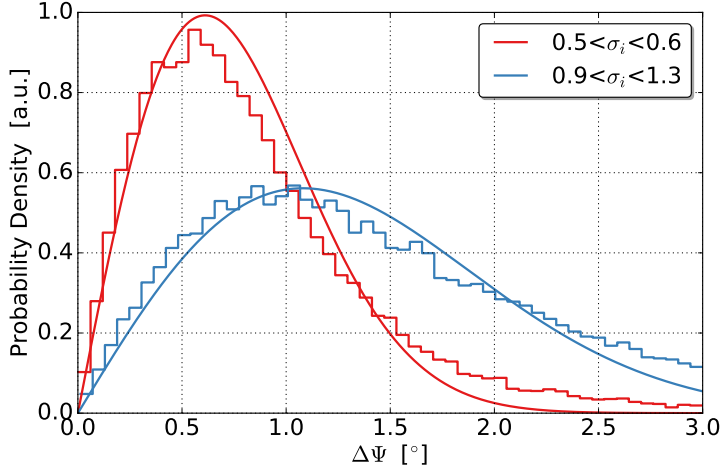
Fig. 6.1.: Angular distance between neutrino and reconstructed muon direction for different ranges of σ_i, the reconstructed angular uncertainty estimator (pull calibrated, see Section 6.1). Solid lines represents the fits of these distributions as two-dimensional Gaussians projected into $\Delta\Psi$. Results of the fits for σ_{fit} are within the expected values, namely $\sigma_{fit} = 0.58$ for the red curve and $\sigma_{fit} = 1.16$ for the blue curve. The value of σ_i is correlated to the track reconstruction error.

Signal PDF

The signal PDF is expressed as the contribution of a spatial and energy part:

$$\mathcal{S}_i = S_i(|\vec{x}_i - \vec{x}_s|, \sigma_i)\epsilon_i(E_i, \delta_i, \gamma) \quad . \tag{6.2}$$

For an event with reconstructed direction $\vec{x}_i = $ (RA, DEC), the probability of being originated from the source located at $\vec{x}_s$ is modeled with a two-dimensional Gaussian:

$$S_i = \frac{1}{2\pi\sigma_i^2} \exp\left(-\frac{|\vec{x}_i - \vec{x}_s|^2}{2\sigma_i^2}\right) \quad , \tag{6.3}$$

where σ_i is the angular uncertainty reconstructed for each event individually (Section 3.4.1, [139]), and $|\vec{x}_i - \vec{x}_s|$ is the angular difference between the reconstructed direction of the event and the source position (the point where we evaluate the likelihood).

Despite the point spread function being evaluated on an event by event basis, it is possible to show the distributions of the angular deviation of the true track with respect to the reconstructed one for different ranges of estimated angular resolutions σ_i, and the two-dimensional Gaussian used as probability density functions, as one can see in Figure 6.1. Here solid lines represent the fit to the distributions, and the resulting σ_{fit} lands within the expected range: $\sigma_{fit} = 0.58$ for $0.5 \leq \sigma_i \leq 0.6$ and $\sigma_{fit} = 1.16$ for $0.9 \leq \sigma_i \leq 1.3$. In an extended source analysis, the signal spatial PDF

is still assumed to be a 2D Gaussian but the point spread function is convoluted with the source extension σ_{src}, resulting in:

$$S_i = \frac{1}{2\pi(\sigma_i^2 + \sigma_{src}^2)} \exp\left(-\frac{|\vec{x}_i - \vec{x}_s|^2}{2(\sigma_i^2 + \sigma_{src}^2)}\right) \tag{6.4}$$

where σ_{src} varies from 1 to 5 degrees.

The signal energy $\epsilon_i(E_i|\delta_i, \gamma)$ PDF describes the probability of obtaining at a declination δ_i a reconstructed muon energy E_i for an event produced by a source that has a power law energy spectrum $E^{-\gamma}$. A typical signal benchmark is $\gamma = 2$, but other values are also possible.

Background PDF

The background B_i PDF is also a product of spatial and energy terms:

$$\mathcal{B}_i = B_i(\delta)\epsilon_i(E_i, \delta_i) \quad . \tag{6.5}$$

Given the analysis is a time integrated one and IceCube is situated at the South Pole, all the inhomogeneities in the atmospheric background event rates caused by the detector acceptance and seasonal variation average out, and due to Earth's rotation the background spatial distribution $B_i^j(\delta)$ is flat in right ascension and depends only on the declination. In Figure 6.2 the background probability density function for the IC86-I data sample is shown. In the southern sky $(-1 \leq \sin(\delta) \leq -0.09)$ this distribution is dominated by atmospheric muons, while in the northern sky $(-0.09 \leq \sin(\delta) \leq 1)$ this distribution is dominated by atmospheric neutrinos. The term $\epsilon_i(E_i, \delta_i)$ represents the probability of an event of energy E_i being atmospheric, and is calculated from the normalized energy distribution for data events at a declination δ_i. Historically, as the point source samples are background dominated, the data itself is used to estimate the background spatial and energy distributions. The same binning as for the signal energy PDF is used for the background energy PDF, and an example of background and signal energy PDFs for the IC86-II data and signal Monte Carlo E^{-2} samples are shown in Figure 6.3. Different signal energy probability density distributions ranging from E^{-4} to E^{-1} and the background energy distribution for one declination bin are shown in Figure 6.4.

The full likelihood combining all data samples is then defined as:

$$\mathcal{L}(n_s, \gamma) = \prod_j \mathcal{L}^j(n_s^j, \gamma) = \prod_j \prod_{i \in j} \left[\frac{n_s^j}{N^j}\mathcal{S}_i^j + \left(1 - \frac{n_s^j}{N^j}\right)\mathcal{B}_i^j\right] \tag{6.6}$$
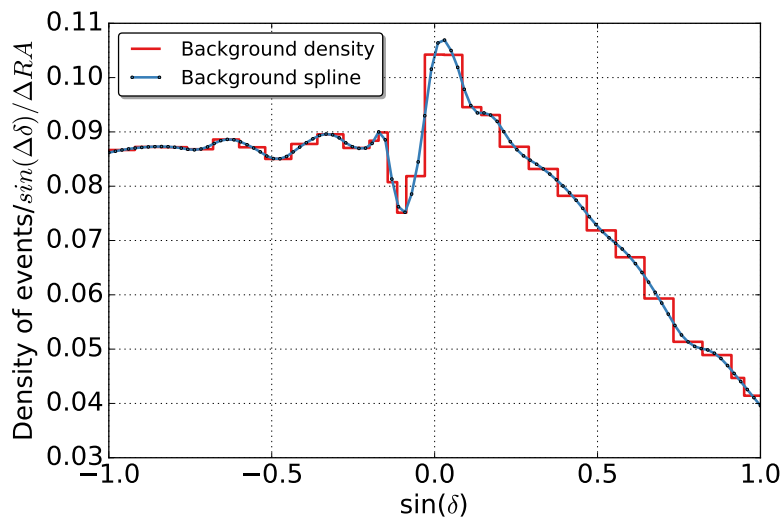
Fig. 6.2.: Background spatial PDF for the IC86-I data sample (see the Appendix A for the binning used for this sample). Within the Skylab framework, splines are used instead of histograms. Point source samples as the IC86-I are dominated in the southern sky $(-1 \leq \sin(\delta) \leq -0.09)$ by atmospheric muons, while in the northern sky $(-0.09 \leq \sin(\delta) \leq 1)$ by atmospheric neutrinos.

(a)

(b)
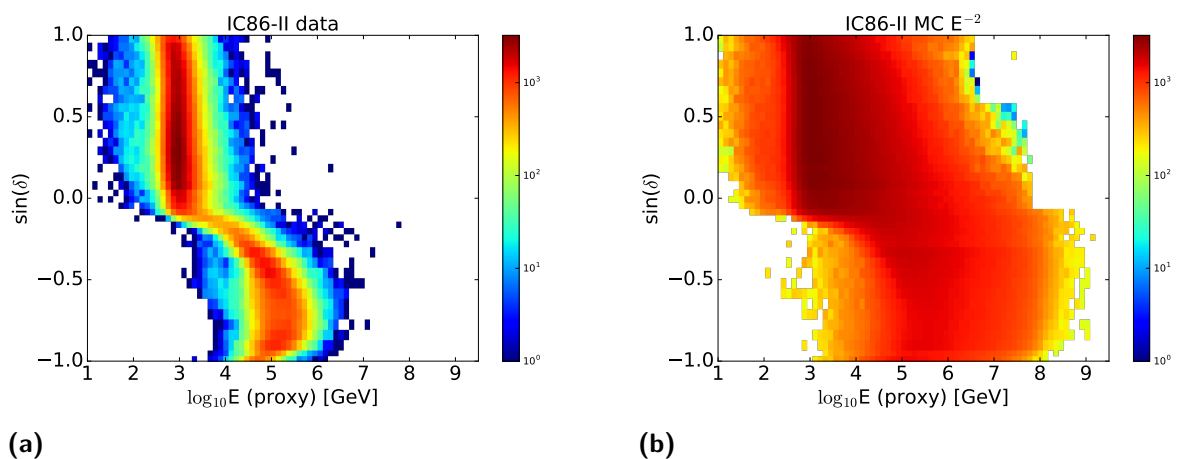
Fig. 6.3.: Energy PDFs for the IC86-II data (6.3a) and signal Monte Carlo E^{-2} (6.3b) samples.
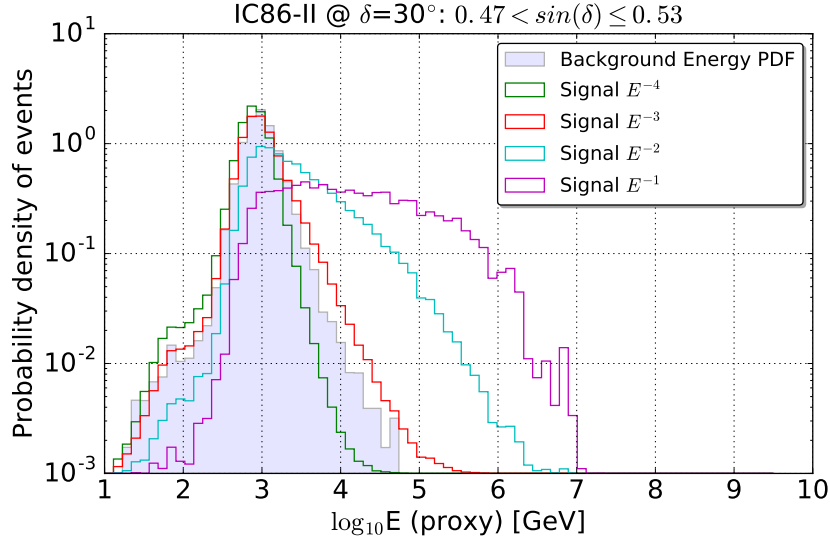
Fig. 6.4.: IC86-II background and different signal PDFs at the declination range correspond-
ing to $\delta = 30°$. This range is $28.16° \leq \delta \leq 31.67°$ in the northern sky, where
the data sample is dominated by atmospheric neutrinos. The spectral index of
conventional atmospheric neutrinos is $\gamma = -3.7$, and it is possible to notice indeed
how the background data distribution is close to the ones for E^{-4} and E^{-3} signal.

where the best fit parameters $(\hat{n}_s, \hat{\gamma})$ are determined by maximizing the likelihood
$\mathcal{L}$, done actually by minimizing the $-log\mathcal{L}$ at a specific location in the sky using
the L-BFGS minimization routine implemented in Scipy [155]. The likelihood is a
function of only a single spectral index γ and total number of signal events at each
location in the sky. Since the analysis is time independent, we do not allow the
spectral index γ to vary independently for each dataset. Analogously, the total fitted
number of signal events n_s is split divided into a contribution n_s^j for each year of
data

$$n_s = \sum_j f^j(\gamma, \delta) n_s^j \quad . \tag{6.7}$$

Figure 6.5 shows a stacked plot of the relative contribution for each detector year
given a spectral index $\gamma = 2$, an extension of $1°$ over the full declination range. As
can be seen, the realtive contribution is uniform over declination, with the smallest
detector IC40 contributing less in the southern sky than in the northern sky.

Gaussian Kernel Smoothing in the Energy PDFs

Before introducing the relative contributions of the samples used in the analysis,
the minimization of the likelihood was mentioned. Despite the name "maximum
likelihood", this method is instead based on a minimization. In our case, the fraction
of signal events n_s as well as the source spectral index γ are not known, and their
best estimate is determined by minimizing the quantity $-\log(\mathcal{L})$. However, the
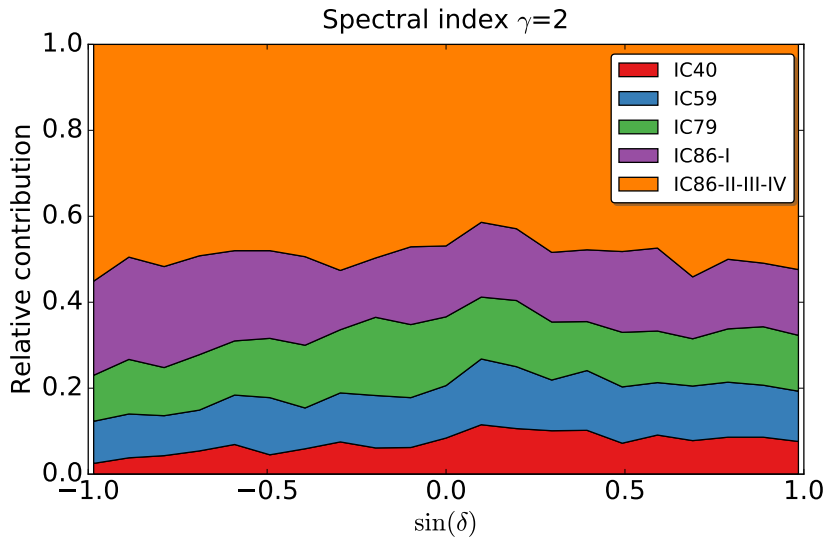
Fig. 6.5.: Stacked plot of the relative contribution of each sample for a spectral index $\gamma=2$ for a source extension of $1°$ as a function of the declination.

quantity that is actually minimized is not $\mathcal{L}$, but a likelihood ratio that will be introduced a bit further in the text (Equation 6.9). For this quantity to be calculated, the ratio of the signal and background probability density functions is needed, both for the energy and spatial parts. The Skylab package used in the analysis does not use histograms, but splines them to get a smoother and continuous distribution as PDF. This distribution however, as it can be seen in Figure 6.2 for example, follows very closely the histogram, and, if fluctuations are present and no precaution measurements are taken, the spline will fluctuate as well. In Figure 6.6 an example of the signal to background ratio for the energy PDFs for the IC86-II sample in the declination band - $0.22 \leq \sin(\delta) <$ -0.18 is shown. The solid lines represent the value of the ratio evaluated at the center of the band, while the points represent the actual events as they distribute inside the band. This unforeseen bumpy behavior, resulting from fluctuations within the histograms, is not optimal, as it affects the fitted spectral index that minimizes the likelihood. A Gaussian kernel smoothing is therefore introduced for the signal to background ratio energy PDF. By convoluting the signal and the background separately with a Gaussian of a given width before proceeding with the ratio, the resulting histogram is smoothed out. For comparison, the effect of this Gaussian kernel is shown in Figure 6.7. The effect of the smoothing is clearly visible in the signal to background ratio. The energy range of the data present in that declination band is shown, however if while sampling events from the Monte Carlo set an event ends up having an energy outside the data range it will be assigned the most signal-like weight.
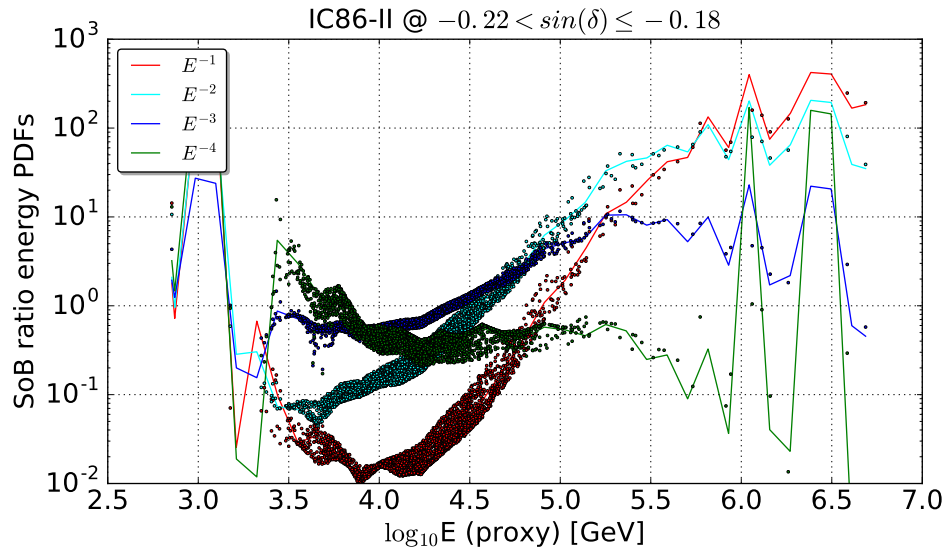
Fig. 6.6.: Signal to background ratio of the energy PDFs for four different spectral indexes for events within a declination band (dots). Lines represent the value calculated at the center of the declination band.
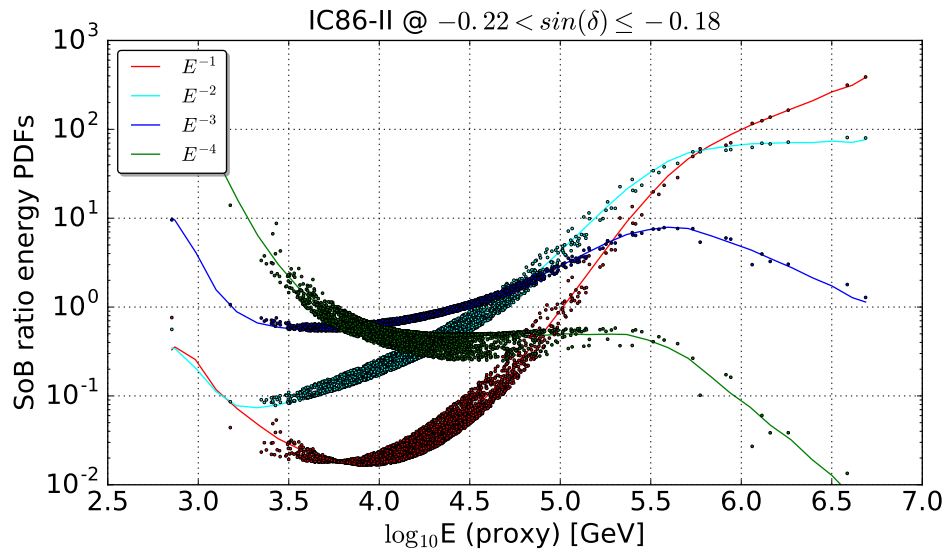
Fig. 6.7.: Same as Figure 6.6 with a Gaussian smoothing kernel. Before proceeding with their ratio, signal and background PDFs are now filtered separately by means of a Gaussian smoothing kernel. After this convolution the resulting histograms are less bumpy, as their resulting ratio.

To evaluate the likelihood in a given point in the sky three quantities are needed for each event: its location, its angular uncertainty and its energy. The precision with which these are known contributes together with the event selection to the performance of the analysis. For the latest likelihood-based energy reconstruction (MuEX, Section 3.4.1), the energy resolution of the energy proxy is ~ 30% in $\log_{10}E$ [140]. Starting from the IC79b sample, the reconstructed direction is obtained using the SplineMPE algorithm (Section 3.4.1). An estimate of the angular uncertainty associated to each reconstruction is obtained using the Paraboloid algorithm (Section 3.4.1), that fits a 2D paraboloid to the likelihood space in the region of the minimum. The quadratic mean of the semimajor and semiminor axes of the 1σ ellipse is used as the angular uncertainty associated to each event. This quantity is commonly called "paraboloid sigma" and represents the uncertainty associated to the reconstructed direction of each event detected by IceCube. This method of estimating the angular uncertainties underestimates however the error for bright events. It is possible to correct for this effect by calibrating the error using the pull distribution. The pull variable is defined as the ratio of the angular distance between the true and reconstructed directions over the angular uncertainty. As an example, the median of the pull distribution for the IC40 dataset is shown in Figure 6.8 to the left. The systematic energy dependent underestimation of the error is observed, and to correct for this effect the paraboloid sigma needs to be calibrated. The 50% containment radius for a bivariate normal distribution is r = 1.1774σ. Hence, if the paraboloid sigma is correctly representing the angular resolution, the median of its pull distribution should be 1.1774. The calibration is done using a spline fit, and the corrected pull distribution is shown in Figure 6.8 to the right, where the white dots indicate the median of the pull aligned at 1.1774.

6.2 Hypothesis Testing and Test Statistic

The goal of a statistical test is to make a statement about how well the observed data stand in agreement with a given hypothesis. The hypothesis under consideration is traditionally called the *null hypothesis*, or $\mathcal{H}_0$, and the *alternative hypothesis* is $\mathcal{H}_1$. In our case the null $\mathcal{H}_0$ and the alternative $\mathcal{H}_1$ hypothesis are:

$\mathcal{H}_0$: all the events in the sample are background events: atmospheric neutrinos in the upgoing region and mostly atmospheric muons with some contamination from atmospheric neutrinos in the downgoing region, following the background term $\mathcal{B}$ in Equation 6.5.
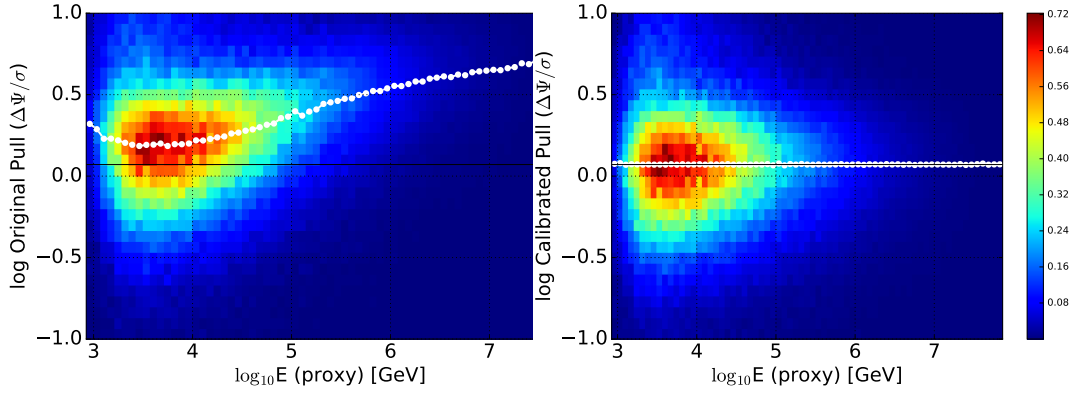
(a) Uncalibrated pull distribution for the IC40 sample.

(b) Calibrated pull distribution for the IC40 sample.

Fig. 6.8.: 2D histograms of the uncalibrated (6.8a) and calibrated (6.8b) pull variable as a function of $\log_{10}$ of the energy for the IC40 sample. For each energy bin, white dots represent the median value of the pulls in that bin. The calibration is done considering the 50% containment and therefore the median should align at 1.1774 in logarithmic scale (solid black line).

$\mathcal{H}_1$: together with background events there is a contribution of n_s astrophysical neutrino events (Equation 6.1), that follow a particular spatial and energy distribution.

Note that in our case the alternative hypothesis $\mathcal{H}_1$ depends on n_s and reduces to the null hypothesis when $n_s = 0$:

$$\mathcal{H}_1(n_s = 0) = \mathcal{H}_0 = \mathcal{B}$$

We measure the usefulness of a statistical test by means of type-I and type-II errors:

Type-I Error *Loss*: $\mathcal{H}_0$ is rejected when $\mathcal{H}_0$ is true. This quantity, described by α, tells you how probable it is that one is claiming a false discovery. α is related to the *null hypothesis*.

Type-II Error *Contamination*: accepting $\mathcal{H}_0$ when $\mathcal{H}_0$ is false. Described by β, this quantity is related to the *alternative hypothesis*.

A schematic representation for α and β for two generic distributions is reported in Figure 6.9, together with a table that summarizes the role of these two variables. Usually instead of speaking of type-I and type-II errors, we speak about significance, confidence levels and power of the test. The probability α is often called the significance level, and represents how often we are rejecting an hypothesis ($\mathcal{H}_0$) this being true. The confidence level (CL) has not been unambiguously defined, and can sometimes refer to $1 - \alpha$ (i.e. how often we avoid making errors of type-I), or can

		$\mathcal{H}0$ true	$\mathcal{H}1$ true
TS $\notin w$ (critical region)	ACCEPT $\mathcal{H}0$	Acceptance good Prob = 1-α	Contamination Error of the II-type Prob = β
TS $\in w$ (critical region)	REJECT $\mathcal{H}0$	Loss Error of the I-type Prob = α	Rejection good Prob = 1-β
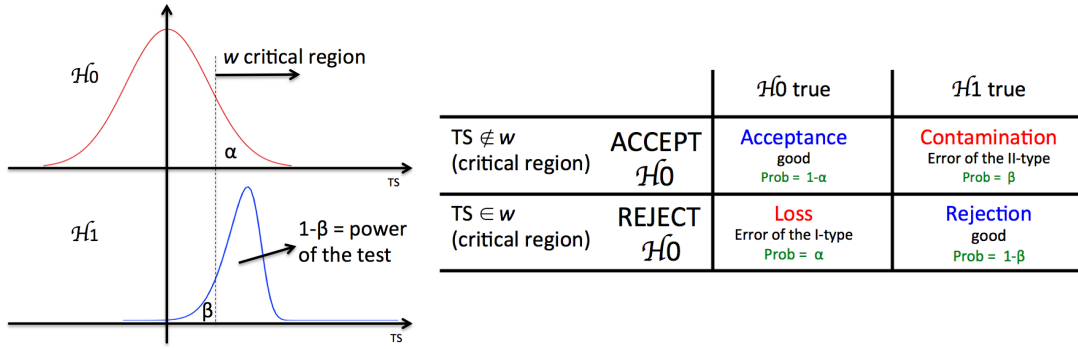
Fig. 6.9.: Hypothesis testing: using the data we have, we would like to accept or reject a given hypothesis $\mathcal{H}_0$ assuming the alternative one $\mathcal{H}_1$. This is done using the TS value, or *test statistic*. If the outcome is $\in w$ then $\mathcal{H}_0$ is rejected with a probability given by α with respect to the null hypothesis and a given power $1-\beta$ with respect to the alternative hypothesis.

refer to type-II errors and the $\mathcal{H}_1$ distribution. The term β represents the probability of accepting $\mathcal{H}_0$ when instead the true hypothesis is an alternative one $\mathcal{H}_1$, and the *power* of the test is defined as $1-\beta$. Ideally we would like to set α and β as small as possible. A trade-off exists between CL and power, and reducing the probability of false discovery necessarily reduces the power to discover any signal present in the data.

6.2.1 Test Statistic

Now that we have been briefly introduced to hypothesis testing, we would like to know how to check whether our data are in agreement with the background only hypothesis or not. To do so, we construct a function called *test statistic* (TS). The maximum likelihood method, among the preferred ones for parameter estimation in statistics, comes in handy when performing statistical tests to the samples in use and defining TS variables. Hence, the TS is defined as the ratio between the likelihood value of the alternative hypothesis $\mathcal{H}_1$ evaluated at the best fit parameters $(\hat{n}_s, \hat{\gamma})$ and the null hypothesis with $n_s = 0$:

$$TS = 2\log\left[\frac{\mathcal{L}(\hat{n}_s, \hat{\gamma})}{\mathcal{L}(n_s = 0)}\right] . \tag{6.8}$$

Therefore, considering the expression of the likelihood in Equation 6.6 and dividing it $\mathcal{B}_i$, the test statistic becomes the value of:

$$2\log\left[\frac{\mathcal{L}(\hat{n}_s, \hat{\gamma})}{\mathcal{L}(n_s = 0)}\right] = 2\log\left[\frac{\hat{n}_s}{N}\left(\frac{\mathcal{S}_i(\hat{\gamma})}{\mathcal{B}_i} - 1\right) + 1\right] \tag{6.9}$$

evaluated at its minimum.

If the background assumption is correct, according to the Wilks theorem [156] a test statistic defined as in Equation 6.8 will distribute as a χ^2 with degrees of freedom
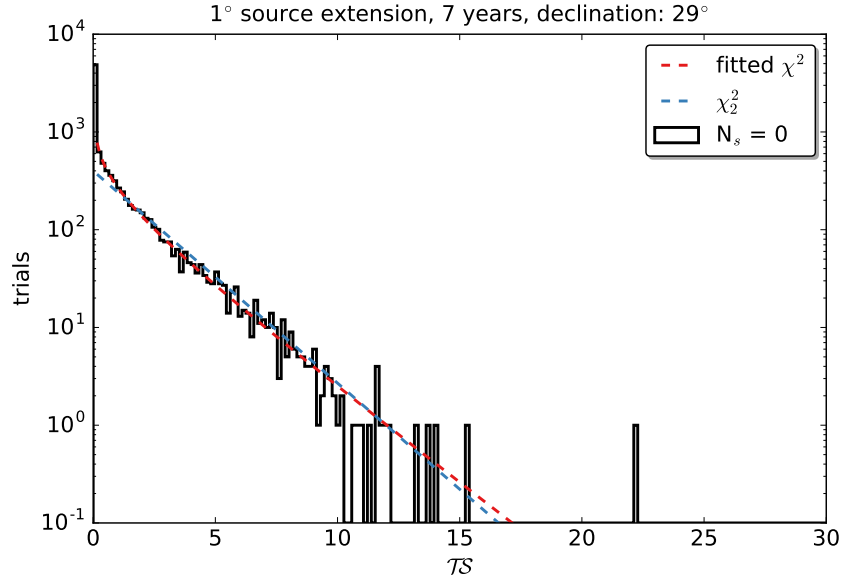
Fig. 6.10.: Background test statistic distribution for a $1°$ extension source located at $\delta = 29°$.

equal to the number of parameters we maximize for. In our case, considering the energy with the parameter γ and the number of signal events n_s, the background TS distribution follows roughly a χ^2 of two degrees of freedom. The distribution is shown in Figure 6.10, where the curve is obtained by performing 10^5 pseudo-experiments, scrambling the events in right ascension at each iteration. In principle n_s can assume both positive and negative values, but we force negative fluctuations to pile up at $n_s = 0$. The theoretical expectation is to have the background fluctuating 50% of the time above 0 (*overfluctuations*) and 50% of the time the TS will pile up at 0 (*underfluctuations*). The distribution of overfluctuations should then fit as a χ^2 of 2 degrees of freedom with a scale factor $\eta = 0.5$. The TS distribution for such a randomized set represents the probability a given observation occurs by random chance with a given frequency. The χ^2 approximation is convenient when running 10^7 background trials is too computationally intense. However, to account for the possible divergences of the actual distribution from the theoretical one, we fit the background distribution at each declination and calculate the ratio of overfluctuations over the total number of trials. These distributions are then used to determine the significance of the outcome in a fully frequentist approach, and also to calculate the significance skymaps.

6.3 Background TS Distributions and Signal-subtracted Likelihood

Background TS distributions carry a wealth of information, and their behavior has to be carefully checked throughout all the declination points as important sanity check. It was indeed while looking at these background TS distribution that a serious issue was detected. Distributions reported in Figure 6.11 are background TS distributions at $\delta = 68°$ for source extensions of $3°$, $4°$ and $5°$. When increasing the extension of the source and scanning declinations closer to the poles, the background is less and less able to fluctuate, producing the pile-up at TS=0. The cause of this behaviour is the failure of the scrambling method as tool for background estimation because of the extension of the signal. The same issue was already found and addressed first in dark matter analyses like the Galactic Center [157], and the new likelihood formalism that solves it is often referred as *signal-subtracted likelihood*. The reason why the background is not able to fluctuate arises from the contamination of signal present in the data, given that we use the actual data to construct the background PDFs. Since the extension considered is not negligible as it is the case for the point source analysis, this contamination does not get washed away in the scramble procedure. Not only the extension cannot be disregarded, but also the number of events is much higher than in the point source case. In analogy with a cut and count experiment, at higher declinations and higher extensions, if there is a fluctuation inside the *on* region, there are not enough patches in the sky for the *off* region to wash away the fluctuation when scrambling. Whenever there is an excess in the region under evaluation, this excess will be part of the background estimate done using the same data only scrambled, limiting background positive fluctuations. Features that becomes more and more difficult as the extension in the $\mathcal{H}_1$ hypothesis increases, until it is impossible for the background to fluctuate, as seen in subfigure c) in Figure 6.11. The solution is obtained by removing the signal contamination by creating a new PDF, the so called *scrambled signal*. Recalling the expression of the standard point source likelihood:

$$\mathcal{L}(n_s, \gamma) = \left[\frac{n_s}{N} \mathcal{S}_i + \left(1 - \frac{n_s}{N} \right) \mathcal{B}_i \right] \tag{6.10}$$

the background term $\mathcal{B}_i$ should represent a pure background contribution. However, we estimate our background using scrambled data, which is contaminated by a signal component. This *scrambled background* $\tilde{\mathcal{D}}_i$ can be described as the sum of two components, the pure background without any signal contamination $\mathcal{B}_i$, and the term expressing the contamination of the scrambled signal $\tilde{\mathcal{S}}_i$:

$$\tilde{\mathcal{D}}_i = \frac{n_s}{N} \tilde{\mathcal{S}}_i + \left(1 - \frac{n_s}{N} \right) \mathcal{B}_i \,. \tag{6.11}$$
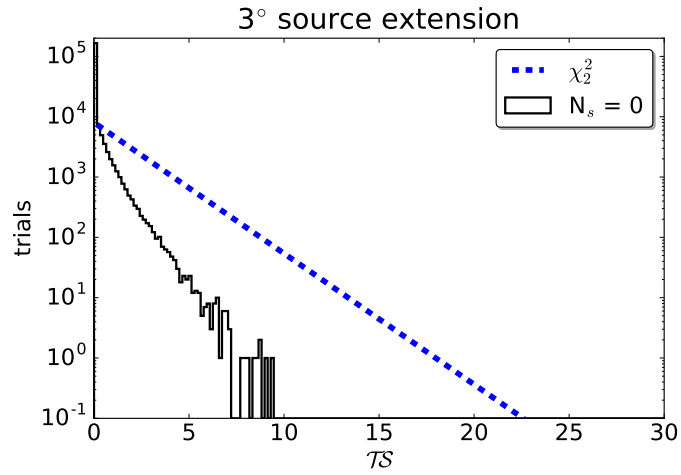
(a)
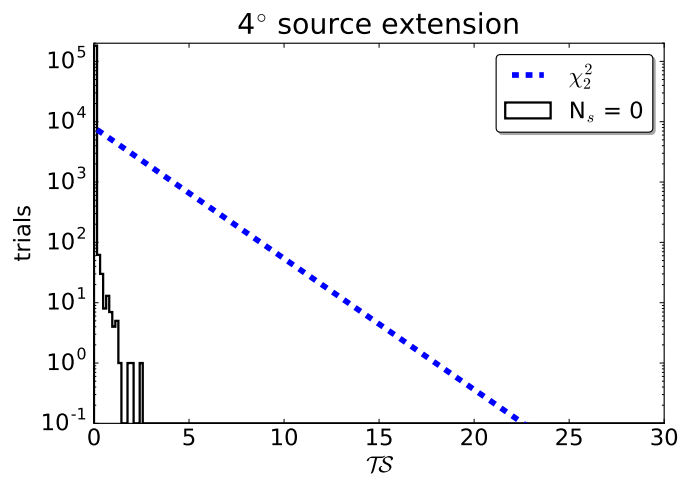
(b)
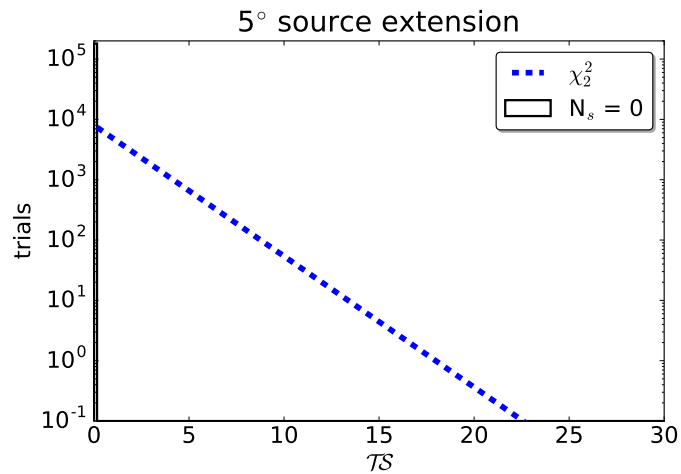
(c)

Fig. 6.11.: $200\,000$ background TS distributions for $3°$, $4°$ and $5°$ source extensions at $68°$ declination for 7 years of IceCube data. The higher the extension, the more difficult is for the scrambled background to reproduce overfluctuations. Believed to be caused by a problem in the energy or spatial PDF binning, it is instead a symptom of a more serious problem, that is the failure of the scrambling method in the presence of extended signal. This problem was solved by moving to the so called *signal-subtracted likelihood*.

When expressing $\mathcal{B}_i$ as a function of $\tilde{\mathcal{D}}_i$ and $\tilde{\mathcal{S}}_i$ and plug the expression into the likelihood formula 6.10, we obtain the expression for the signal-subtracted likelihood:

$$\mathcal{L}_{ss} = \frac{n_s}{N} \left(\mathcal{S}_i - \tilde{\mathcal{S}}_i \right) + \tilde{\mathcal{D}}_i \,. \tag{6.12}$$

With this new formulation, the expression for the final likelihood that is being minimized to evaluate the test statistic parameter is given by:

$$2\log \left[\frac{\mathcal{L}_{ss}(\hat{n}_s, \hat{\gamma})}{\mathcal{L}_{ss}(n_s = 0)} \right] = 2\log \left[\frac{n_s}{N} \left(\frac{\mathcal{S}_i}{\tilde{\mathcal{D}}_i} - \frac{\tilde{\mathcal{S}}_i}{\tilde{\mathcal{D}}_i} \right) + 1 \right] \tag{6.13}$$

to be compared to its analogous expression for the standard point source case (Equation 6.9). All these PDFs have an energy and spatial term. To recall briefly:

- $\mathcal{S}_i$ is the standard signal PDF. The energy PDF is assumed to be a power law distribution with spectral index γ, while the spatial PDF is the 2D Gaussian describing a source with a given extension.

- $\tilde{\mathcal{D}}_i$ is the background term obtained from scrambled data and thus contaminated by a scrambled signal component. Energy and spatial PDFs are evaluated from data.

- $\tilde{\mathcal{S}}_i$ is the scrambled signal PDF needed to implement the *signal-subtracted likelihood*. This PDF accounts for the signal contamination in the scrambling technique and can be understood as the projection in declination of the signal PDF. Since we have modeled the signal as a 2D Gaussian with extension, the resulting spatial PDF of the scrambled signal is represented by a normal distribution divided by the cosine of the declination. In Figure 6.12 an example of the spatial probability density function for the scrambled signal component resulting from a 5° source is shown. The energy PDF is analogous to the signal one, a power law distribution with spectral index γ.

After the implementation of the signal-subtracted likelihood, background positive fluctuations start occurring again approximately 50% of the time. Hence, the resulting background TS distributions approximate correctly a χ^2 distribution, as reported in Figure 6.13.

6.4 Extended Source Injector

To calculate the performance curves described in the next session, namely the sensitivity and the discovery potential, the simulation of events from an extended source topology is required. This signal injection has not only to represent the spatial
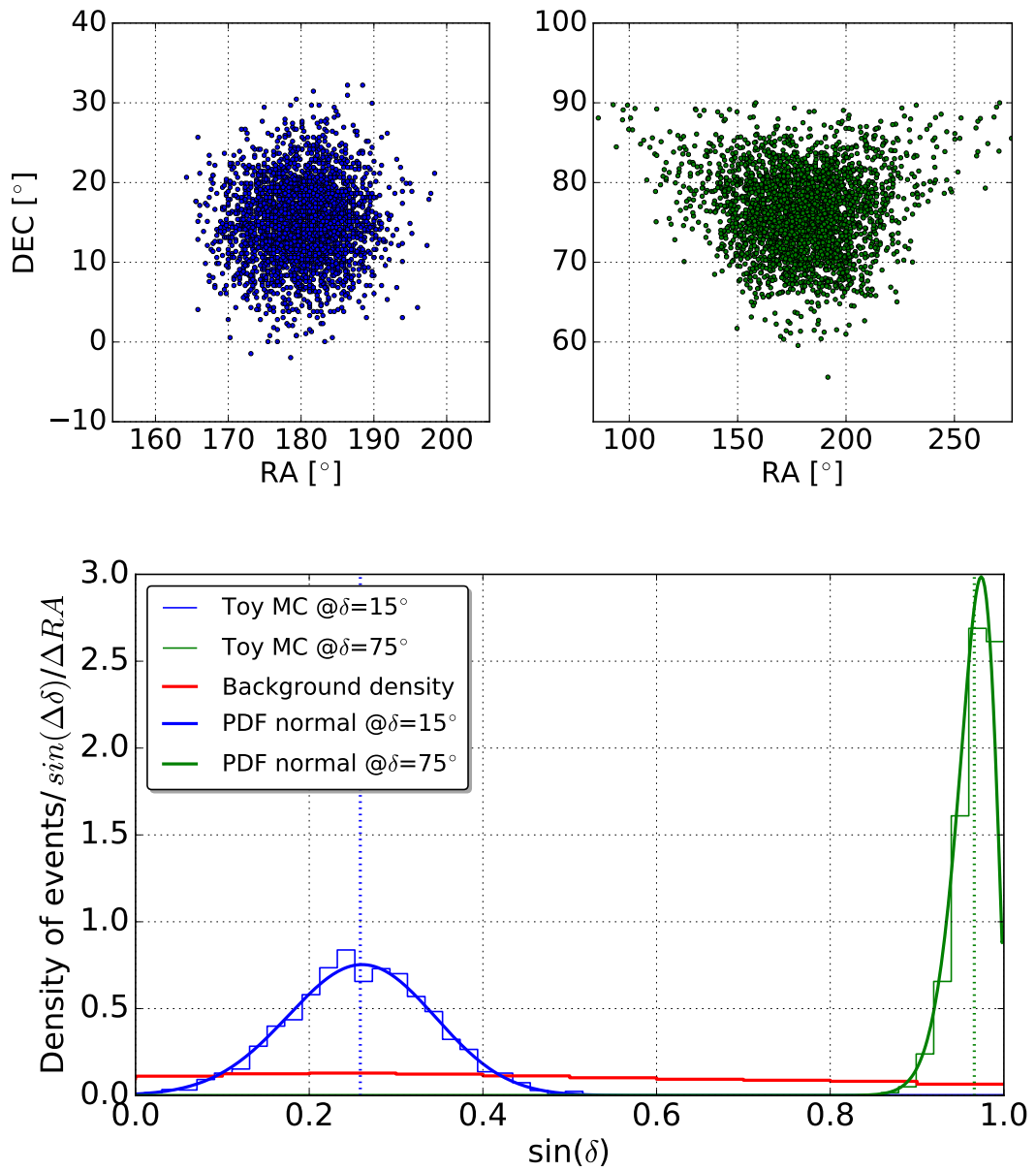
Fig. 6.12.: Example of two spatial scrambled-signal PDFs for two 5° sources located at 180° RA, 15° DEC (blue) and at 180° RA, 75° DEC (green). On top, 3000 events distributed according to the two sources. The closer to the pole the source location, the more elongated its shape. When these events are projected in declination their distributions are the blue and green histograms, labeled Toy MC. These distributions are well described by the normal curves, thick solid blue and green lines, which represent the actual PDF used for the scrambled signal. This is compared to the background density function in red.
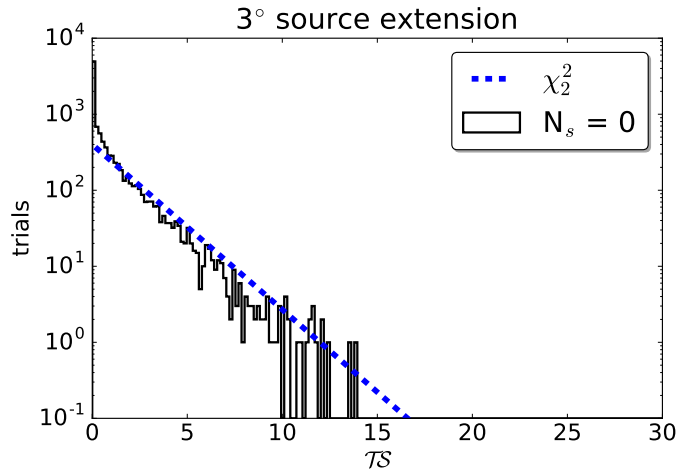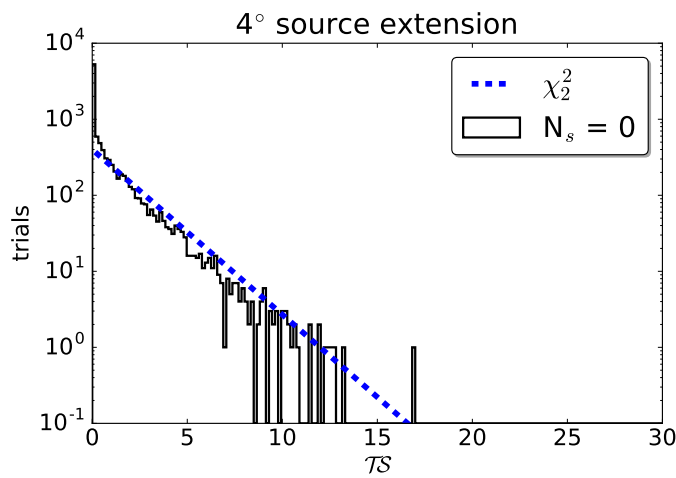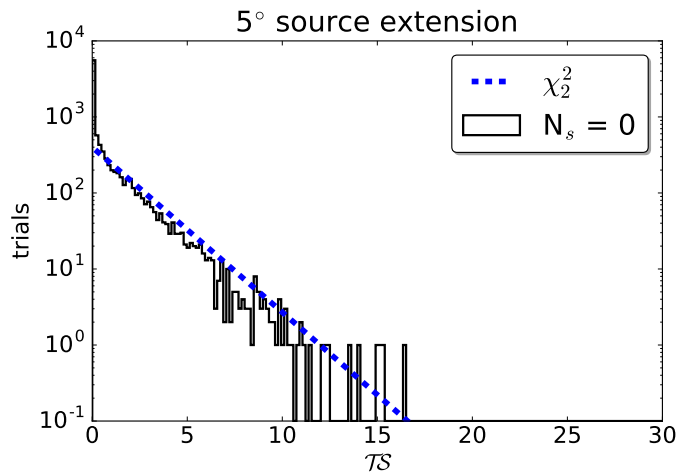
Fig. 6.13.: $10\,000$ background TS distributions for $3°$, $4°$ and $5°$ source extensions at $68°$ declination for 7 years of IceCube data using the *signal-subtracted likelihood*. The contribution of an hypothetical extended source within its declination band is not negligible, and to account for this effect a small correction to the likelihood needs to be implemented, namely the introduction of a third PDF called *scrambled signal*. Once this correction is performed, the correct background behavior is restored.
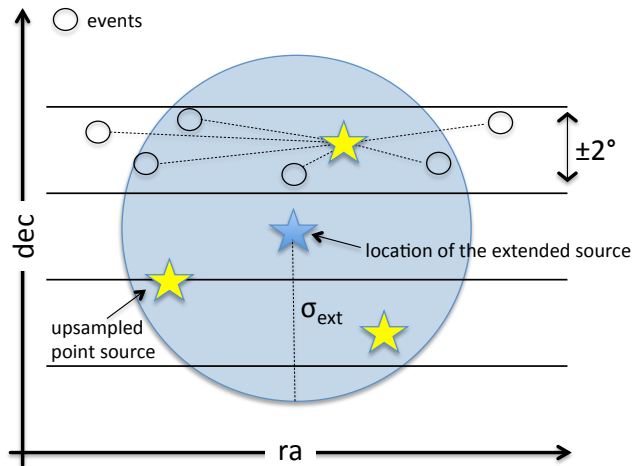
Fig. 6.14.: Schematic representation of the upsampling procedure. A given number (*upsampling*) of point sources are sampled according to a Kent distribution. Signal events are then injected from these locations following a standard point source procedure.

distribution of events coming from an extended source, but it must also respect the energy response of the detector as a function of declination. This task becomes particularly important in the declination regions where the detector acceptance varies most, as it can be seen right below the horizon in the southern sky in Figure 6.3a, for the IC86-II dataset energy distribution. To overcome this potential problem, the simulation of an extended source is performed by sampling events from several injected point sources that mimic the source extension, as illustrated in Figure 6.14. The number of point sources parameter is called *upsampling*. Several possible values for the *upsampling* have been considered, setting the final value to 20. For our purposes this value has been found to be a good compromise between the CPU time performance of the code, a good description of the source and a stability of the performance results. To parametrize the extended source we use the Kent distribution, which for small values of sigma ($< 8°$) can roughly be considered as a Gaussian normalized on a sphere. Once the locations of the upsampled point sources have been determined according to this distribution, a band of $\pm 2°$ centered on these locations is selected and the true direction of MonteCarlo events is rotated on top of each source. The true information is then removed and only the reconstructed one remains to mimic real detector data. These events are then injected to simulate the signal coming from the extended source. In Figure 6.15, yellow stars indicate 20 upsampled locations, while few injected events are represented by blue dots. The bigger the source extension the more important role played by the upsampling technique, which allows one to handle the events' energies correctly, especially in the region of the sky close to the horizon where the energy distribution varies considerably over few degrees.
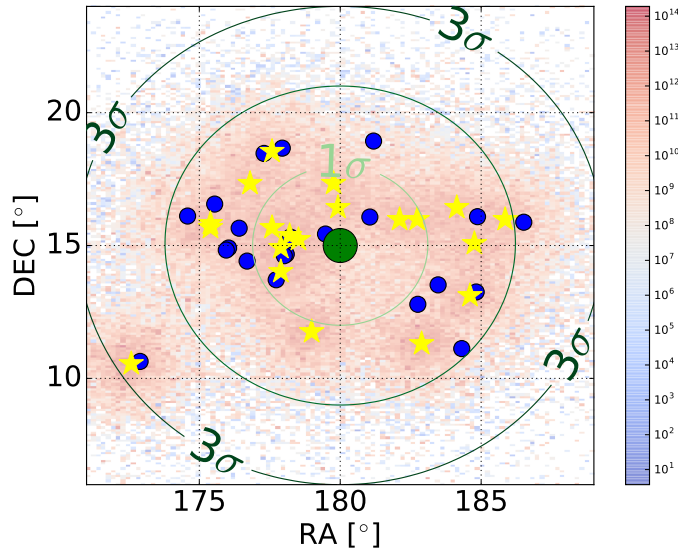
Fig. 6.15.: Extended injector working principle. An extended source located at 180°RA, 15°DEC is simulated using 20 upsampled sources represented by yellow stars, while the blue dots indicate injected random events. The z axis indicates the density of the MC events around the upsampled sources.

6.5 Sensitivity and Discovery Potential

Most of IceCube analysis are optimized in a blind way. In our case, we do not prevent ourselves from looking at the data, but the analysis is conducted using a random right ascension value instead of the real one. By doing this way any possible signal in the data remains hidden. Once all the steps are approved by the working group, and after a two week collaboration review period, it is possible to look at the unblinded data. Before doing so, it is custom to produce two performance curves, called *sensitivity* and *discovery potential*.

To understand the meaning of these values we need to go back to the hypothesis testing paragraph, and recall that values for alpha and beta are conventions. Sensitivity represents the median upper limit (α=0.5) at 90% confidence level, where the confidence level being $1 - \beta$ and referring to the alternative hypothesis. 90% of the times the signal hypothesis considered $\mathcal{H}_1$ will have a TS equal or higher than the measured one, while the background would do so only 50% of the times. Sensitivity curves for the five different source extension considered are shown in Figure 6.16. It can be seen that the higher the source extension, the higher the flux required to claim a source is a candidate of neutrino emission.

The threshold necessary to claim a discovery in IceCube is on the other hand customary set at α=5σ level with respect to the background distribution with a 50% chance to the signal distribution (β). This value is called the discovery potential: it
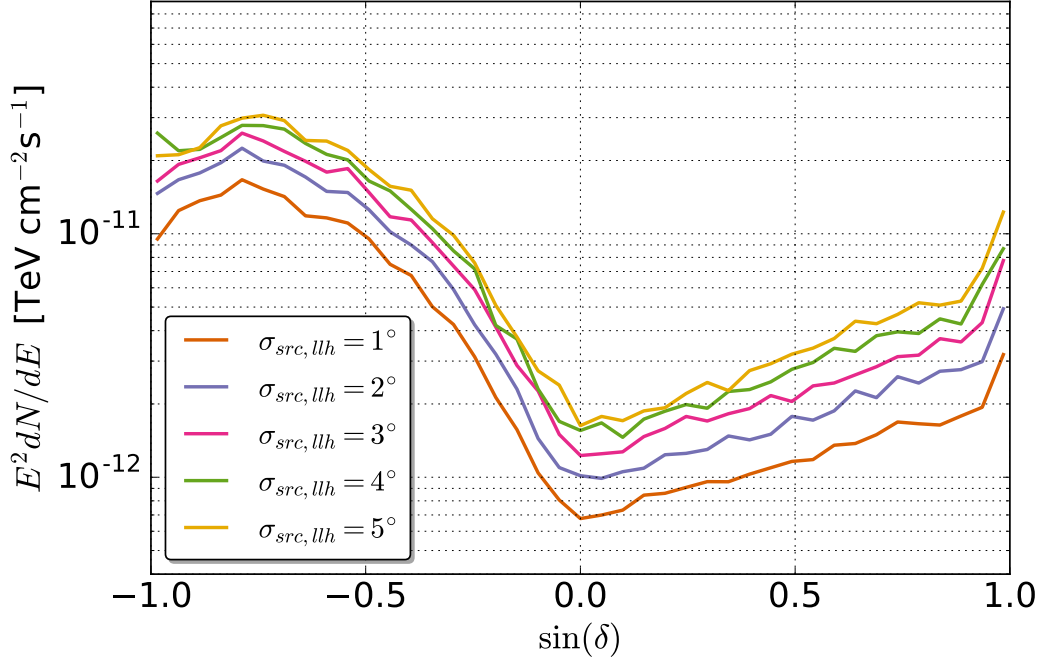
Fig. 6.16.: Sensitivity at 90% confidence level for the five extensions considered. The best case scenario is assumed, that is when the source extension in the injector matches exactly the extension of the likelihood scan.

represents the neutrino flux at a given declination for a given spectral index required to claim a 5σ discovery, but knowing that only 50% of the times this flux will be detected. A 3σ level result is conventionally considered an evidence. Discovery potential curves for the five extension considered are shown in Figure 6.17. Also in this case, the higher the source extension, the higher the flux required to claim a discovery. The difference in the background rates for the northern and southern hemispheres affects the shape of the two figures of merit of the analysis, and the southern sky performance is penalized by the higher background rates.
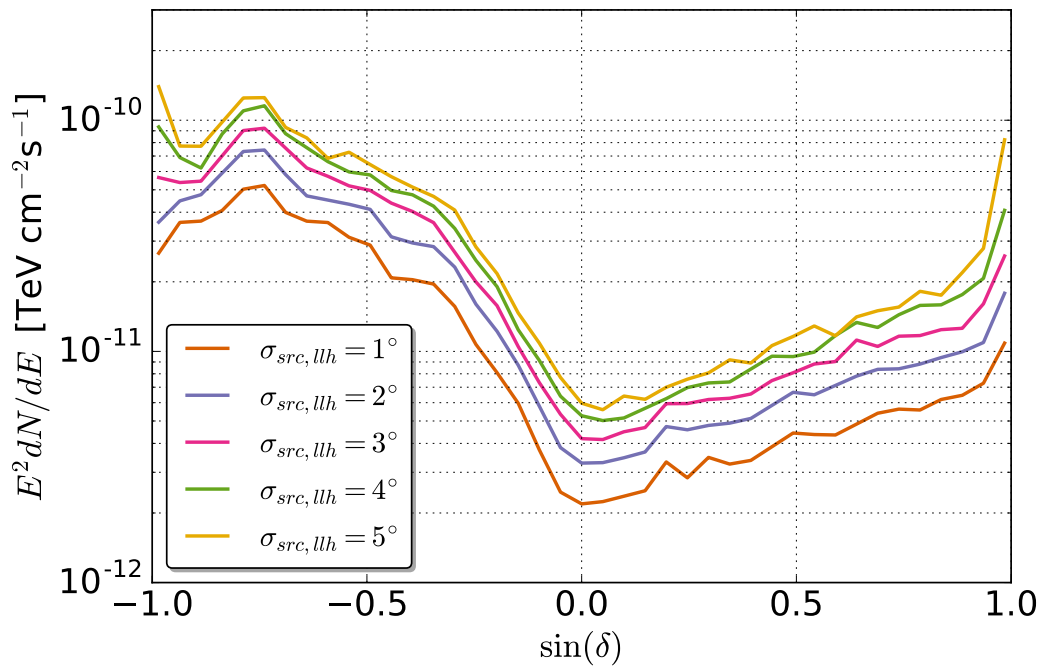
Fig. 6.17.: Discovery potential at 50% confidence level for the five extensions considered. The best case scenario is assumed, that is when the source extension in the injector matches exactly the extension of the likelihood scan.

Results

<div style="text-align: right; font-size: large;">7</div>

The final goal of the analysis presented in the previous Chapter is to perform five all-sky scans for possible extended sources of neutrinos that have a Gaussian shape and an extension σ_{src} ranging from $1°$ to $5°$. The analysis has been conducted using seven years of IceCube data from three years of operation in partial levels of completion (IC-40, IC-59 and IC-79) and the first four years of the completed 86 string detector (IC86-I, IC86-II, IC86-III and IC86-IV). Data have been collected from May 2008 to May 2015, for a total of 713752 events after event selection for through-going muon neutrinos (see [61] for more details on the event selection) in 2426.2 days of livetime. The previous extended source analysis was limited to four years, using samples from IC40 to IC86-I, and the results are shown in [158]. The two hypothesis that are tested are the background only hypothesis (null hypothesis) and the signal plus background hypothesis (alternative hypothesis), and at each location in the sky a test statistic parameter TS is used to discriminate between the two. The TS is defined as the logarithm of a maximum likelihood ratio, namely as

$$TS = 2\log\left[\frac{\mathcal{L}(\hat{n}_s, \hat{\gamma})}{\mathcal{L}(n_s = 0)}\right] .$$

Recalling the formulation for the likelihood and substituting in the formula above we obtain that the test statistic is the value of:

$$2\log\left[\frac{\mathcal{L}(\hat{n}_s, \hat{\gamma})}{\mathcal{L}(n_s = 0)}\right] = 2\log\left[\frac{\hat{n}_s}{N}\left(\frac{\mathcal{S}_i(\hat{\gamma})}{\mathcal{B}_i} - 1\right) + 1\right]$$

evaluated at its minimum.

Following a fully frequentist approach, the significance of the outcome for each TS calculated is compared to the possibility the same outcome is given by background. Five pre-trial significance skymaps have been produced for each source extension from $1°$ to $5°$, and the corresponding post-trial p-value calculated for the most significant hotspot in each map. Under the null hypothesis, the p-value is defined as the probability of obtaining a result equal or higher than the one observed. No hypothesis test yielded significant evidence of clustering. The significance is defined as $s = -\log_{10} p$, and therefore, the smaller the p-value p the higher the significance.

To produce a significance skymap, the starting point is an HEALPix map [159] that contains $196\,608$ pixels, with an angular resolution of $0.46°$. The likelihood is minimised and the test statistic evaluated at the center of each pixel. The resulting TS value is compared to the background distribution at that point. Background TS distributions have been calculated beforehand for 41 declination points, and the two parameters needed to describe them, that is η, the scale factor of the distribution given by the ratio of the number of trials with $TS > 0$ (overfluctuations) and the total number of trials, and n_{dof}, the number of degrees of freedom of the fitted χ^2 distribution have been stored and splined to cover all the possible declinations needed in the map evaluation. The comparison of the obtained TS value with the background distribution results in the so called pre-trial p-value, that needs to be corrected for the fact that about 2×10^5 minimizations are perfomed. This effect, also know in the high energy particle physics community as the *look elsewhere effect*, consists in the fact that a significant hotspot might arise from background fluctuations if a sufficiently high number of trials is performed. In our situation nearby pixels are not independent, and the number of trials is not simply equal to the number of pixels. To properly account for trials, post-trial p-values are obtained in a fully frequentist approach by scrambling the datasets hundreds of time and building pre-trial p-value distributions for each extension (Figure 7.6). For each map, the observed p-value is then compared to the distribution to obtain the post-trial. Additionally, a conservative factor of five can be applied to the hottest among the five maps to account for the fact that the maps are not independent.

All-sky scans for source extensions of $1°$, $2°$, $3°$, $4°$ and $5°$ are shown in Figures 7.1, 7.2, 7.3, 7.4 and 7.5, respectively. The location of the hottest spot is marked by a black box on the sky. Post-trial distributions are shown in Figure 7.6. Results of the significance maps are grouped in Table 10.2. All the results are consistent with the background-only hypothesis. The most significant among the maps is the $1°$ extension with a post-trial p-value of 0.1. This result is however not significant, especially if considering a conservative trial factor of 5 to account for the fact that the maps are not independent. This is also the reason why hotspot locations for the $2°$ and $3°$ extensions and also for the $4°$ and $5°$ ones are the same. However, these locations have been checked and do not correspond to any know cataloged astrophysical object.

Being significance a statistical concept, one might wonder how a skymap would actually look like if we would plot instead the directions of the IceCube events in the data samples used in the analysis. The answer is however unfortunate, as the map would look completely black. Nevertheless, to help the reader imagining event directions on top of the statistical significance, Figure 7.7 shows in the background the $1°$ extension hotspot with superimposed the IceCube events within a window

Extension [°]	RA [°]	DEC [°]	$\hat{n}_s$	$\hat{\gamma}$	p-value (pre-trial)	p-value (post-trial)
1°	249.32	63.28	73.32	1.85	8.20×10^{-7}	0.10
2°	169.44	27.04	102.92	2.19	9.04×10^{-6}	0.30
3°	169.37	27.68	119.18	2.16	7.31×10^{-5}	0.58
4°	229.82	-66.64	140.05	1.63	2.23×10^{-4}	0.78
5°	231.56	-66.44	160.83	1.68	1.99×10^{-4}	0.60

Tab. 7.1.: Summary of the results from the extended all-sky survey. The coordinates of the most significant spots located for each source extension hypothesis are given together with the respective p-values.
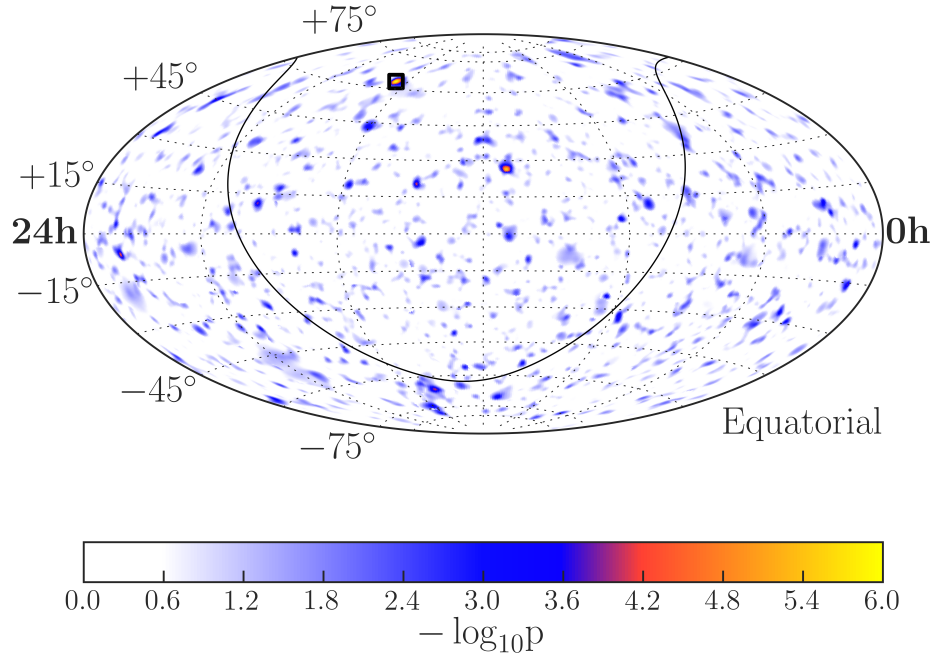
Fig. 7.1.: Pre-trial significance skymap for a 1° source extension and 7 years of through-going muons. The solid black line represents the galactic plane. The hottest spot is highlighted with a black box.
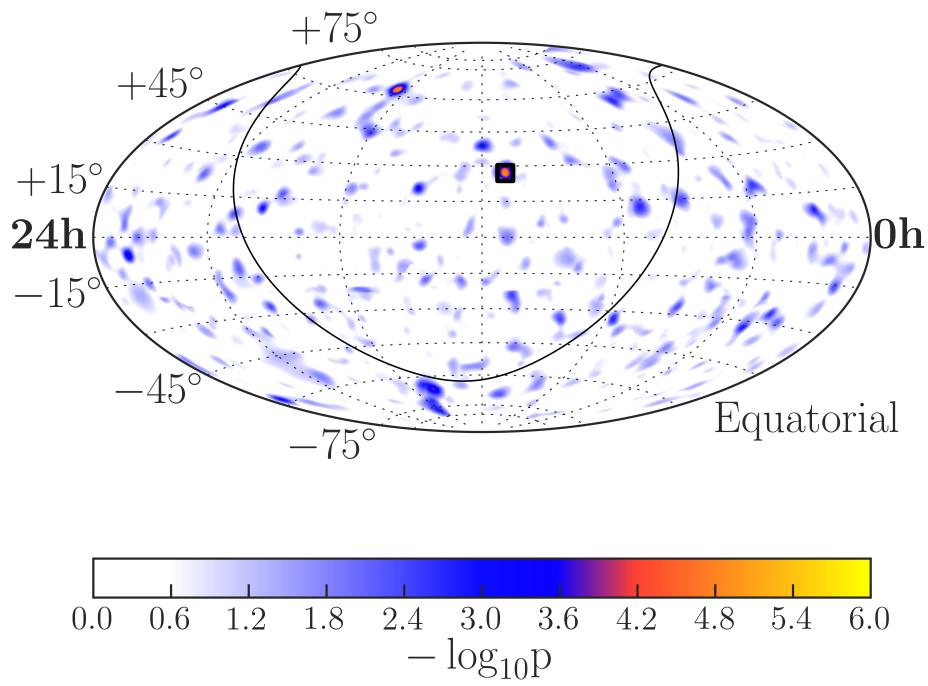
Fig. 7.2.: Pre-trial significance skymap for a 2° source extension.
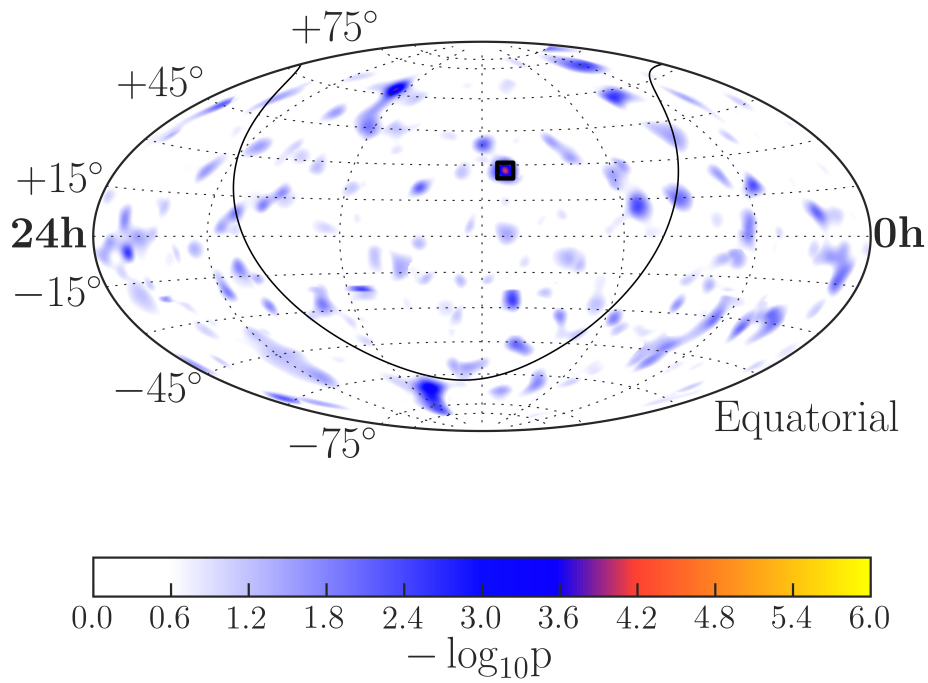
Fig. 7.3.: Pre-trial significance skymap for a 3° source extension.
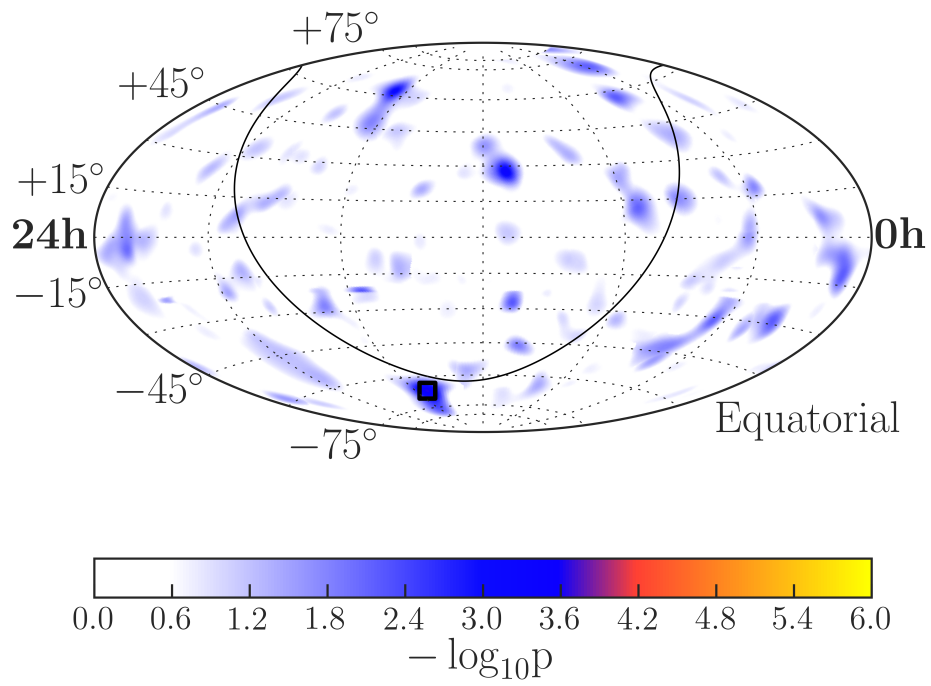
Fig. 7.4.: Pre-trial significance skymap for a 4° source extension.
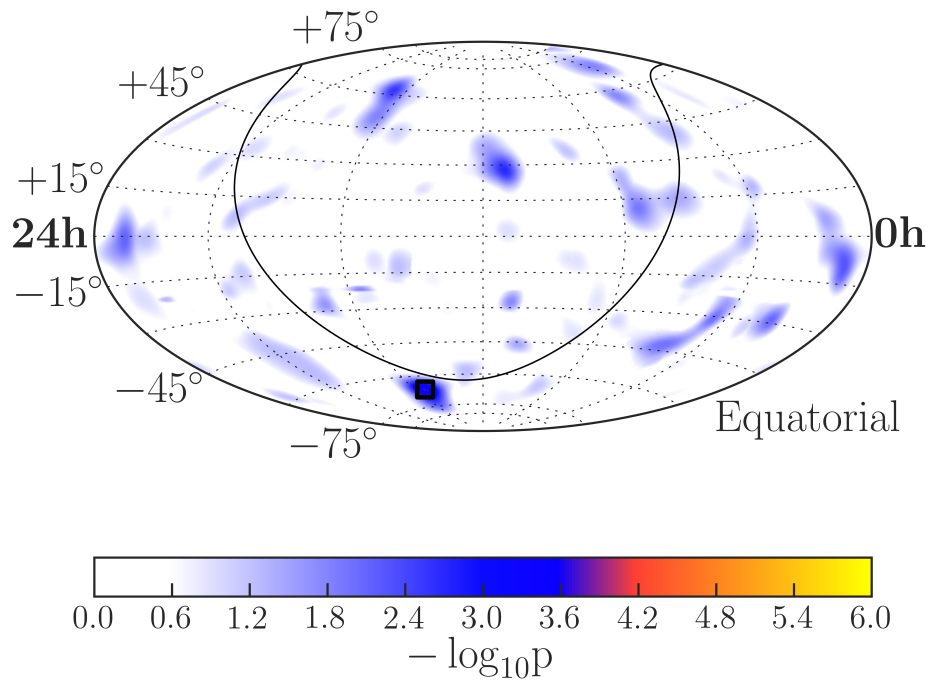
Fig. 7.5.: Pre-trial significance skymap for a 5° source extension.

(a) 1° map. Post-trial p-value 0.10

(b) 2° map. Post-trial p-value 0.30

(c) 3° map. Post-trial p-value 0.58

(d) 4° map. Post-trial p-value 0.78

(e) 5° map. Post-trial p-value 0.60
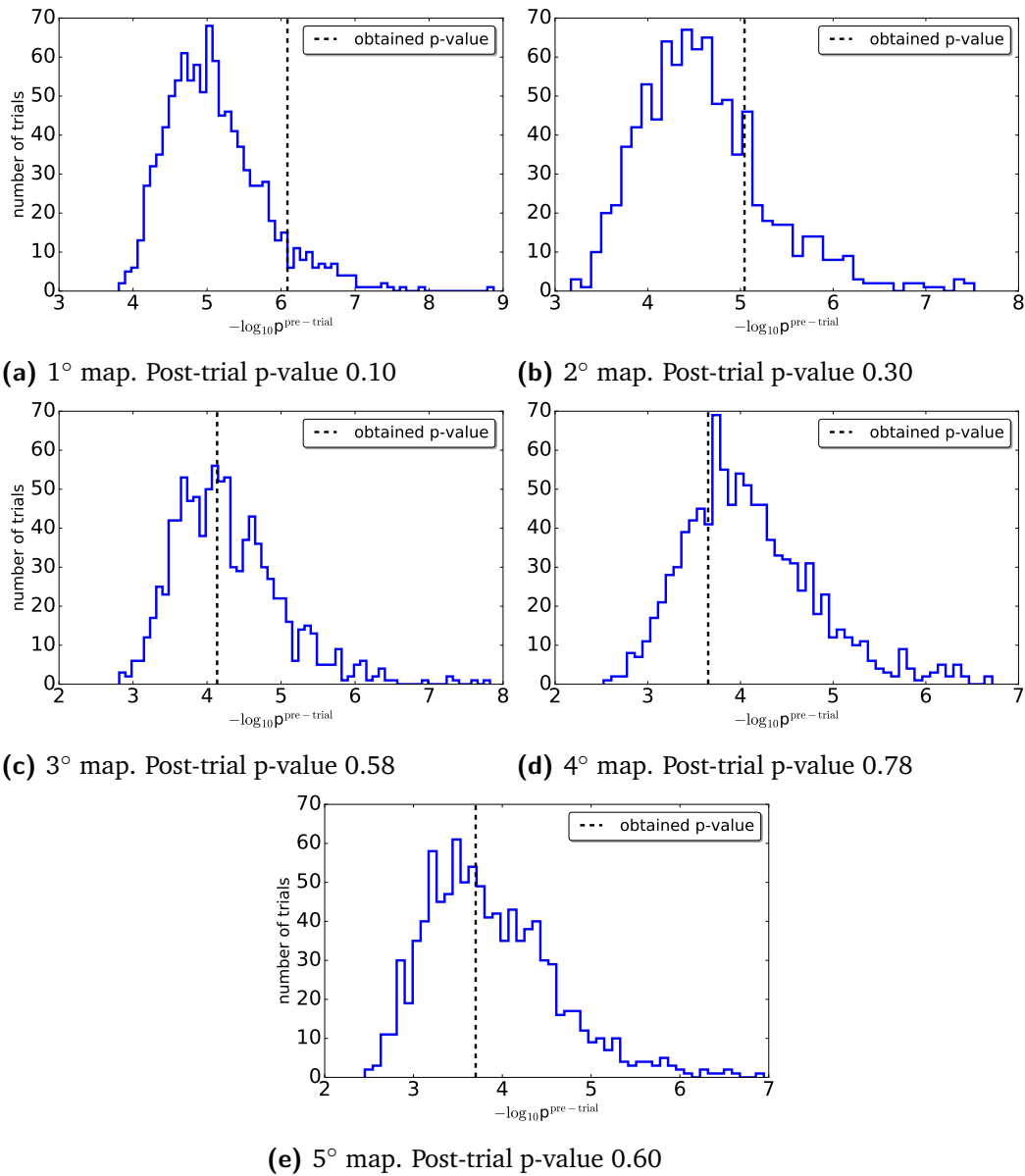
Fig. 7.6.: Distribution of $-\log_{10}$ of the pre-trial p-values for the background scrambled map hotspots for each extension. This distribution is needed to calculate the post-trial p-value of the observation, that is evaluating how many times a background map would produce by chance a hotspot with significance equal or higher than the one observed. The dashed line in each plot marks the observed p-value of the hottest spot of the corresponding scan.
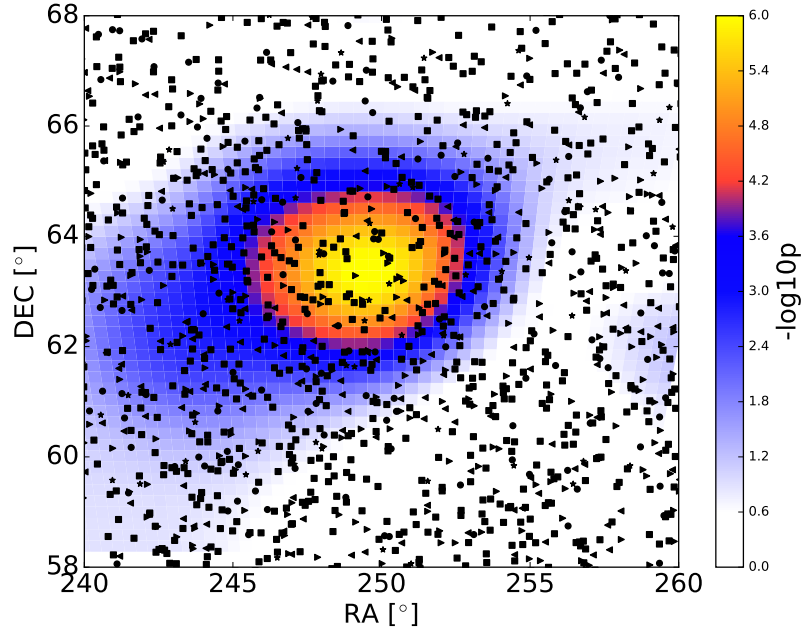
Fig. 7.7.: Scan of a window of $20° \times 10°$ around the location of the hotspot of the $1°$ extension. Black markers indicate IceCube events belonging to different samples.

of $20° \times 10°$. Different markers correspond to different samples (IC40, IC59, IC79, IC86-I and IC86-II-III-IV).

7.1 Systematic Uncertainties

The search for extended sources is robust against systematic uncertainties. Background estimations are obtained by scrambling detector data in right ascension. Hence, the resulting p-values are neither affected by possible systematic uncertainties from the atmospheric muon and neutrino background simulations nor from the modeled detector response. Important factors that enter the calculations of systematic errors are the understanding of the ice optical properties as scattering and absorption, the absolute calibration of the DOMs, i.e. optical efficiency of Cherenkov light yield and detection by the DOM, and different neutrino cross section models. Systematic uncertainties affect the event expectation from a given neutrino flux, as the $d\Phi/dE_\nu \propto E^{-2}$ considered in the analysis. Upper limits and sensitivity calculations rely on the injection of simulated signal events, and are therefore affected by systematics. The contribution of the systematic uncertainty in sensitivity and discovery potential fluxes is estimated by repeating the calculations using Monte Carlo simulation with varied ice properties and DOM efficiencies. The optical efficiency is the parameter that impacts mostly the flux calculations. A $\pm10\%$ variation results in a flux uncertainty of 7.5%. Increasing the absorption or scattering of photons in ice by 10% introduces a 5.6% flux variation. Uncertainties in the photo-nuclear

cross-sections result in a similar flux uncertainty of 5.9%. Adding these values in quadrature yields a total systematic uncertainty of 11% on $\nu_\mu + \bar{\nu}_\mu$ fluxes [61].

Summary of Part II

In this second part of this work we have presented the search for extended sources with 7 years of IceCube data. The motivations for such a search are manifold. In 2013 IceCube announced the detection of an astrophysical neutrino flux, which has now been established with a significance exceeding 7σ. The sample that made this discovery possible, known as the High Energy Starting Event or HESE sample after the event selection adopted, shows however no clustering in space nor association with any source catalog. Analogously, results published in early 2017 [61] from the seven years point source search, which uses a through-going muon dataset, are consistent with the background-only hypothesis. The search for the sources of these neutrinos should therefore embrace also extended topologies.

Extended sources have already been detected both in the γ-sky and cosmic-ray sky, and this analysis might be sensitive not only to sources that are extended in nature, as for example supernova remnants, but might also benefit from the fact that several point sources, whose fluxes are too dim to be detected separately, happen to be closely located in space. In addition, it has been shown that, if an extended source is present in the sky but we keep looking at it using statistical tools suited for point sources we might be blind to it. Despite the high trial factor, the choice of selecting the entire sky and not targeting only a specific region of the sky (as for example the Galactic Plane), is motivated by the fact that there are possible extended sources that have an extragalactic origin, as for example clusters of galaxies. In addition, a dedicated Galactic Plane analysis is about to be published soon by the IceCube Collaboration.

A novel likelihood method has been implemented, subtracting background contributions that mimic the signal and restoring the expected background behavior. With this new likelihood, sensitivity and discovery potential performances have been calculated, and five significance skymaps have been produced, testing extensions from $1°$ to $5°$. The post trial p-value has been calculated for each map's hottest spot, and results are summarized on Table 10.2. No statistically significant evidence for a source with any of the extensions considered was found.

Since no significant clustering has been found, it is possible to set upper limits on muon neutrino and antineutrino fluxes for specific points in the sky. However, the lack of neutrino flux predictions from extended sources does not allow us to constrain any model. Moreover, we do not see any benefit in setting upper limits on locations of the sky that do not present any known source, as it is the case for the hotspots locations. The main improvement to this analysis would therefore be finding models of neutrino flux predictions from extended γ-ray sources, in order to constrain them or possibly rule out some scenarios. Moreover, it will be interesting to construct *a priori* a list of know extended γ-ray sources, choosing those few that have extensions greater than $1°$.

Part III

Feasibility Study of a New Communication
System for the IceCube-Gen2 Project

Overview of Part III

The third part of this work is dedicated to present the feasibility study of a new communication system for the IceCube-Gen2 upgrade. The IceCube-Gen2 detector, a considerable expansion of the current IceCube detector, is being proposed to advance the state of the art in multi-messenger astronomy. In Chapter 8 the detector baseline is presented. This detector, able to deliver a substantial increase in the astrophysical neutrino sample for all flavors, would support a rich physics program, including a search for point sources, a detailed spectral and flavor characterization of the astrophysical neutrinos, searches for cosmogenic neutrinos, studies of cosmic rays, and searches for signatures of beyond-the-standard-model neutrino physics. The upgrade would need not only new hardware to be deployed in ice, but also an overhaul of the communication system. In Chapter 9 the current communication system in IceCube is presented, showing the entities involved in the process. In Chapter 10 a feasibility study for a new communication protocol has been performed, targeting the simplest form of digital modulation, that is Binary Phase Shift Keying. A printed circuit board has been manufactured to simulate 3.5 km of IceCube cable. The modulated signal has been produced using an Arbitrary Waveform Generator, and, after being filtered waveforms were retrieved and analyzed on the laptop. All the simulation work was carried out in Python.

The IceCube-Gen2 Project

<div style="text-align: right">**8**</div>

We have seen already that soon after the 1956 observation of the neutrino by Reines and Cowan, it became clear it represented the ideal astronomical messenger. In addition of being stable, having neutral electric change and approximately no mass, neutrino weak interactions allow the particle to travel astronomical distances almost undisturbed, carrying essential information on the environment of production and acceleration. The same extremely feeble interactions with matter are however the reason why huge particle detectors are required to collect a statistically significant number of events, and the concept of a cubic-kilometer detector was already introduced in the 1960s [4, 160].

Four decades later, the IceCube Neutrino Observatory has fulfilled one of its major scientific goals with the discovery of an astrophysical neutrino flux. Several independent analyses conducted over multiple years of IceCube data have revealed approximately 100 astrophysical neutrino events, implying that a significant fraction of the energy in the non-thermal universe is generated in hadronic processes. However, the event sample size available is still not sufficient to find any significant directional point source clustering nor a clear association with any known astrophysical source class so far. Also the extended source search fails in finding any evidence of clustering in space. To overcome these difficulties the IceCube-Gen2 facility update is being promoted. IceCube-Gen2 is a considerable expansion of the current detector which includes, among others, the instrumentation of a 10 km^3 volume and a surface veto. With its unprecedented sensitivity and improved angular resolution, this instrument will explore extreme energies (PeV-scale) and will collect high-statistics samples of astrophysical neutrinos of all flavors, enabling detailed spectral studies, significant point source detections and new discoveries, together with a broad spectrum of research goals as cosmic ray studies and searches for signatures from physics beyond the standard model [5].

Since 2014, a collaboration-wide effort is ongoing to establish the best characteristics of the detector upgrade. Performance studies involve all scales of the project: not only new optical modules are proposed, but also new signaling and time synchronization methods are examined and an improved hot water drilling system is under investigation. In the following chapter we describe the general baseline detector.

The IceCube Gen2 Facility
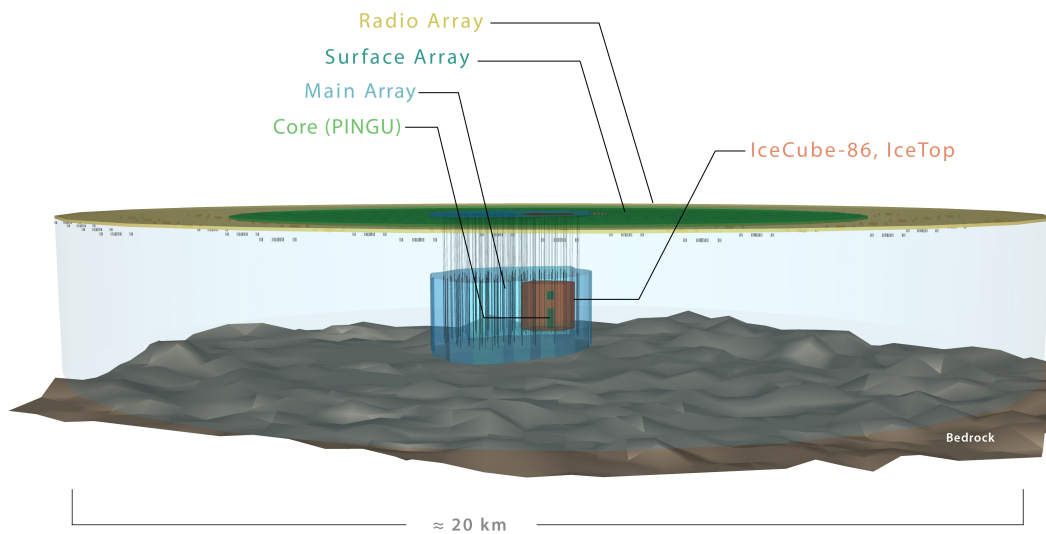
Fig. 8.1.: A conceptual drawing of the IceCube-Gen2 Facility.

Funding may strongly affect both the time scale and the specifics of each point, but the salient point for each sub-detector should remain consistent.

8.1 Gen2 Baseline detector

A conceptual drawing of the IceCube-Gen2 Facility is shown in Figure 8.1. Despite specific points of design being likely to evolve quite a bit, the multiple sub-detector division should not undergo major changes.

PINGU The Precision IceCube Next Generation Upgrade (PINGU) is a proposed low-energy in-fill extension to the IceCube DeepCore detector. Its science goal is to measure the neutrino mass hierarchy by reconstructing neutrino angles and energies below 10 GeV. Given the strong competition with other experiments such as Hyper-Kamiokande [161], INO [162], JUNO [163] or ORCA [164], PINGU is a time-critical deployment and must start data taking in 6-8 years. The current baseline detector foresees the deployment of 26 strings instead of 40, with 192 digital optical modules each. The energy threshold is below 5 GeV.

High Energy Array (HEA) HEA is a PeV scale neutrino detector, and will use optical sensors evolved from the IceCube one. HEA will take advantage of the very long absorption lenghts found in the glacial ice near the IceCube detector, instrumenting a volume of ~ 10 km^3 with lower string densities. This results in a higher energy threshold, targeting neutrinos above ~ 50 TeV with the highest efficiency [5]. The proposed baseline detector extends IceCube by 120 strings.

Cosmic Ray Array (CRA) Veto array for HEA as well as exploration of cosmic-ray physics. In addition to in-ice veto strategies used in several analyses including the first observation of astrophysical neutrinos, cosmic-ray showers can be directly vetoed on the surface. The addition of this cost-effective atmospheric veto will allow all-sky neutrino studies without having to restrict samples to smaller detector volumes or cut on neutrino energies to overcome the atmospheric muon background [5].

Radio Array (RA) Built following the Askaryan Radio Array (ARA) design [99] or perhaps as a much denser array of radio frequency (RF) detectors.

Both PINGU and HEA need new hardware to be deployed in ice, but the choice of the new digital optical module is far from being made. Two scenarios are left open. In the first one the choice of the new optical module falls on the prototype that is heavily based on the current IceCube DOM, called P-DOM. Despite the high number of channels required for HEA, the P-DOM design is certainly the lowest risk option, and the fastest in terms of deployment, an aspect that is potentially crucial for PINGU. On the other hand several ongoing R&D projects propose brand new prototypes of better photodetectors. The M-DOM, D-Egg and WOM target a different problem each, as for example the small photocatode area, increased in the MDOM, or the directionality of the light collection. New sensor designs are depicted in Figure 8.2. On the communications point of view, no choice has been made so far, having focused all the efforts on the hardware aspect first. However, it has been realized from the beginning that any future facility upgrade will need an overhaul of the existing communication system: the increased density of channels will require the system to handle multiple channels per communication pair, to limit costs and cabling deployment. Cost containment will drive also the cable choice, and the need of using a cheaper cable than the current one reflects on the robustness of the new signaling method against noise. The asymmetry in the current communication scheme, described in more detail later in the text, is a feature that is currently not exploited, but can be used as an asset in the future protocol. Initial communications protocols will likely be similar or identical to Gen1 DOMs, mainly to allow initial testing with DOR1 cards of the new P-DOM mainboards, recently produced in few specimens. It is possible however that more sophisticated phase-shift keying (PSK)
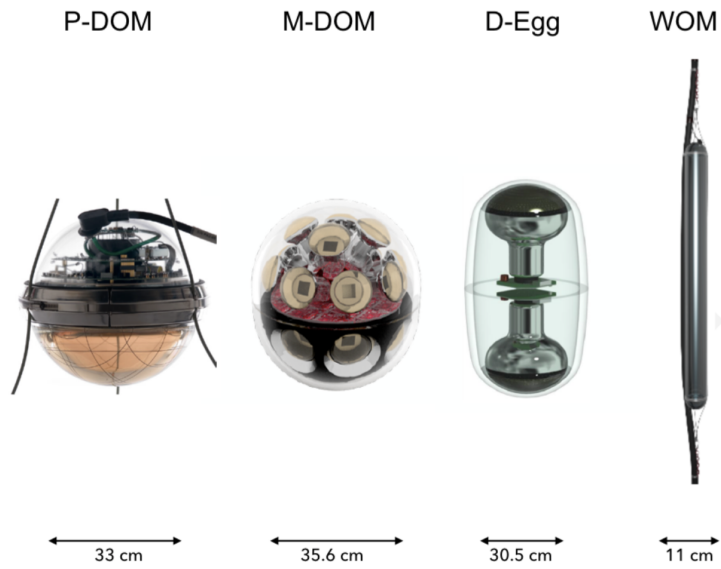
Fig. 8.2.: Ongoing R&D efforts for the new digital optical modules for Gen2 [165].

digital modulation techniques could be further investigated as alternatives to the standard scheme. A preliminary study of the simplest form of digital modulation, called Binary Phase Shift Keying, is presented in this work.

Current IceCube Communications Design

<div style="text-align: right">

9

</div>

Before moving to the specific case of communications in IceCube, it is easier to start with an analogy related to the daily life experience: communications among people. In fact, whether it being between people or computers, a communication process can be broken down into three key aspects. The first important aspect are the subjects that need to communicate, let's assume two persons. The second one is the medium they use to communicate: if they decide to talk, the air serves as medium, if they write each other using a piece of paper, paper becomes their medium. Regardless of the subject of the conversation, the last aspect is the convention they decide to adopt. Whether people agree to use English or French, hieroglyphics, drawings or sign language, it is essential that all the players agree on having the same communication scheme. This is just a simple analogy to grasp the idea behind communications.

Moving to the specific case of IceCube we identify these three key aspect into the following:

Entities involved: the DOM (Digital Optical Module) and the DOR (DOM Readout interface) are the two principal entities involved in the communication process;

Transmission medium: communications in IceCube run over twisted copper pairs;

Protocol: IceCube currently uses a Non-Return-to-Zero-like (NRZ-like) bipolar signaling, and the protocol is a custom packet-based scheme.

In this chapter a brief overview of the IceCube communication system is presented, focusing separately on each of the three aspects mentioned above. We refer to the recently published paper *Instrumentation and Online Systems*, taken as reference, for further reading [121].
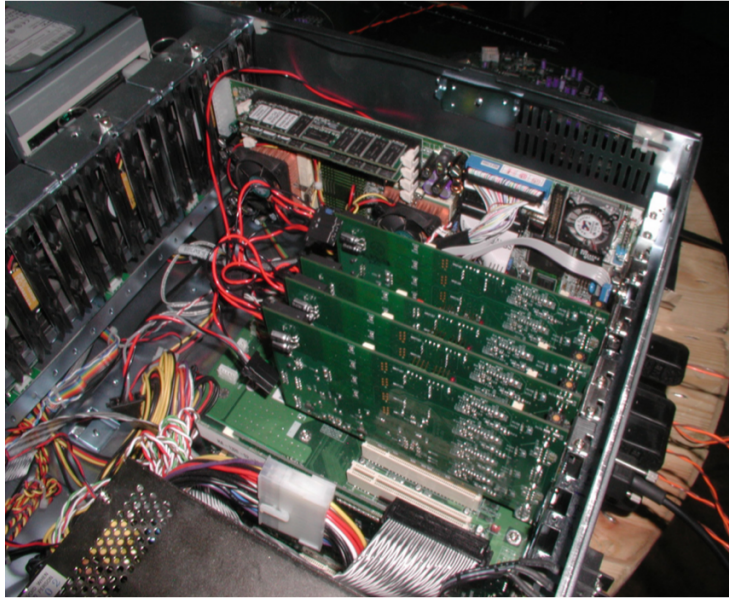
Fig. 9.1.: Picture of a DOM HUB. Each DOR Card (8/DOM-Hub) serves 8 DOMs.

9.1 Entities involved: The DOR and DOM

The DOM Readout card (DOR) is the interface between a DOM and the IceCube surface Data Acquisition system (DAQ). It provides several critical functions in the DAQ chain, among which:

- Power management for the DOM;

- Communications to and from the DOM;

- Major State control of the DOM;

- Data collection and buffering;

- Message dispatch to selected DOMs;

DOR cards connect DOMs to the computers, called DOMHubs, which receives DOM signals in the IceCube Laboratory, the counting house located on the surface of the ice. Each DOMHub stores up to 8 DOR cards, Figure 9.1. The DOR card serves four wire pairs, or two "quads". For the in-ice detector, one twisted pair serves two DOMs, and one DOR card serves thus eight DOMs. On the other hand, one twisted pair serves a single IceTop DOM, due to the higher rates recorded. Therefore, each DOMHub services a single in-ice string or 8 IceTop stations. Figure 9.1 is a picture taken during assembly, and shows a DOMHub with DOR cards being installed. The
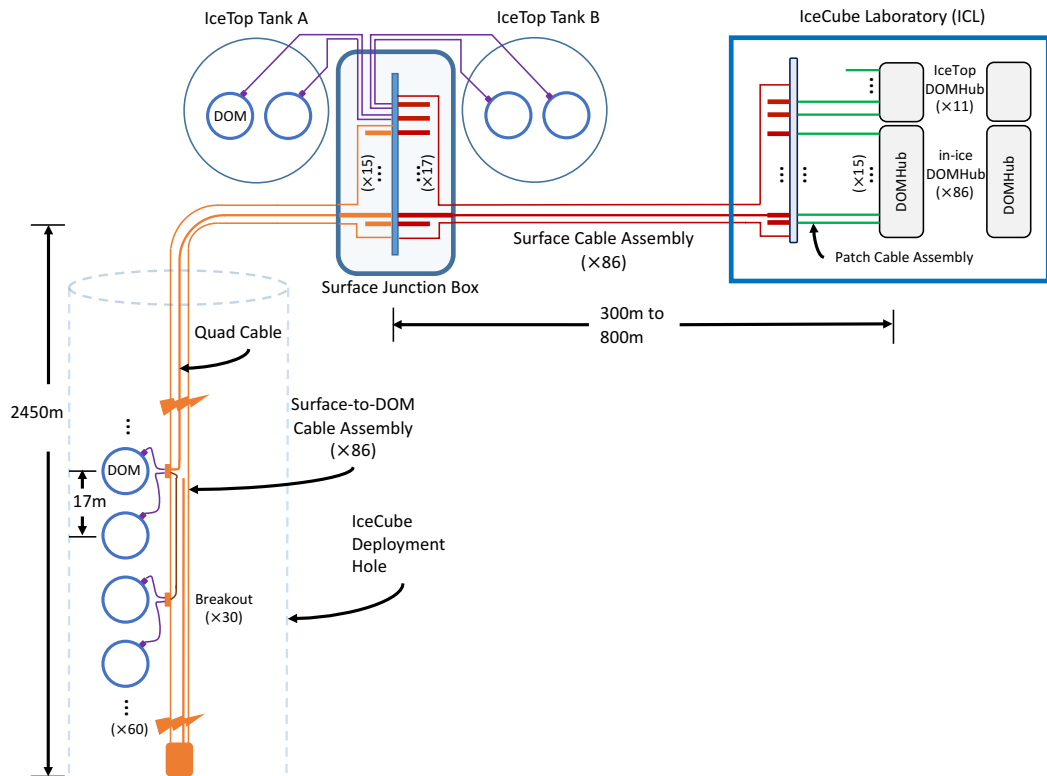
Fig. 9.2.: Schematic of the cable system parts [121].

communications interface to the cable is essentially an Analog to Digital Converter (ADC) and a Digital to Analog Converted (DAC).

9.2 Transmission medium: IceCube Cable System

The cable system in IceCube serves the double purpose of carrying power and communications to the DOMs. We can split the system into a few parts: the in-ice cable, IceTop cables, the surface junction box (SJB), the surface cables and the patch cables (Figure 9.2). The in-ice cable, 2505 m long, is deployed into the ice along with 60 DOMs that are attached to connectors at 30 breakouts. An adjacent pair of DOMs is connected to a distinct twisted wire pair. The connection between the DOMHub and the DOM MB inside the pressurized sphere is accomplished through twisted quad pairs with 145 ohm characteristic impedance. Two DOMs are connected to each twisted pair. Two wire pairs are combined into four-conductor quad cables meeting stringent electrical performance requirements; the quad arrangement provides enhanced cross-talk immunity and improved mechanical stability during freeze-in compared to a twisted pair. The 60 DOMs on each cable require a total of 15 quads. An additional 5 quads in the in-ice cable provide for special instrumentation

Labels on figure (left side, top to bottom): conductor, insulation, filler, quad, quad sheath, water block, strength member, filler

Labels on figure (right side, top to bottom): outer wrapping, sheath, copper shield, strength member, sheath, drain wires
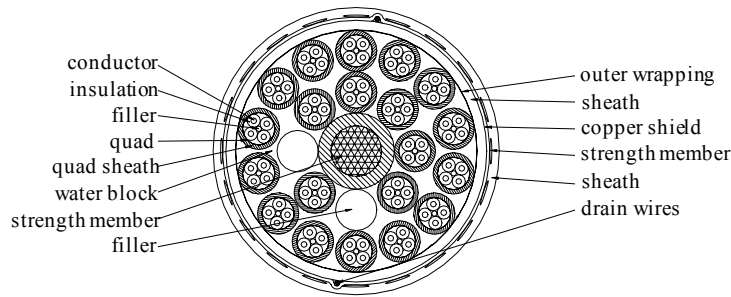
Fig. 9.3.: In-ice cable cross section [121].

connections, a spare quad, and local coincidence cable links used for bidirectional signaling between neighboring DOMs, resulting in a 20 quad configuration plus two polyethylene fillers to maintain structural symmetry, Figure 9.3. DOMs can be divided into A and B types. The "T" labels indicate A type DOMs, where an electrical termination of 145 Ω is installed, and B DOMs are unterminated. From the point of view of communications, the termination used has to match the cable impedance in order to avoid reflections. This is why terminated DOMs are located below the unterminated ones in a DOM pair, as shown in the schematic on Figure 9.4. In-ice cables terminate at the SJB, located between IceTop tanks just below the snow surface. The SJB is a stainless steel enclosure that houses the in-ice cable and surface cable connections. Finally surface cables, located at about 1 m depth in the snow, bring all the cables to the IceCube Computing Laboratory, ICL. Surface cables vary from 300 m to approximately 800 m in length depending on the hole location with respect to ICL. The surface cables are pulled up two cable towers into the ICL and terminate at patch panels where the individual quads are separated and connected to patch cables that finally terminate at the DOMHub.

9.3 Protocol: NRZ-like custom packet-based

Digital communication between the DOR card and DOM occurs via copper twisted pairs. The information collected by the PMTs is translated into a series of 0s and 1s, i.e. is *digitized*, in the DOM MB. Which protocol do the DOR card and DOM adopt? The current standard is of the type UART, Universal Asynchronous Receiver and Transmitter: the data custom packet is composed of one start bit, eight data bits and one stop bit. Signaling is DC-free, that is the mean value of the voltage is zero, and is of the Non Return to Zero (NRZ) type. In a NRZ signaling scheme a logic 1 bit is sent as a high value and a logic 0 bit is sent as a low value of voltage. IceCube's encoding is NRZ-like because the 0 bit corresponds to the quiet line while the 1 bit to a symmetric bipolar pulse. The communication signals decoder is therefore based on the detection of the falling edge of the pulse. When the falling edge is longer than a given threshold, a logic one is detected (Figure 9.5). This

To surface

To next DOM above

Communication
& Power Pair #0

Communication
& Power Pair #1

Local Coincidence
Pairs

T

17m

T

To next DOM below
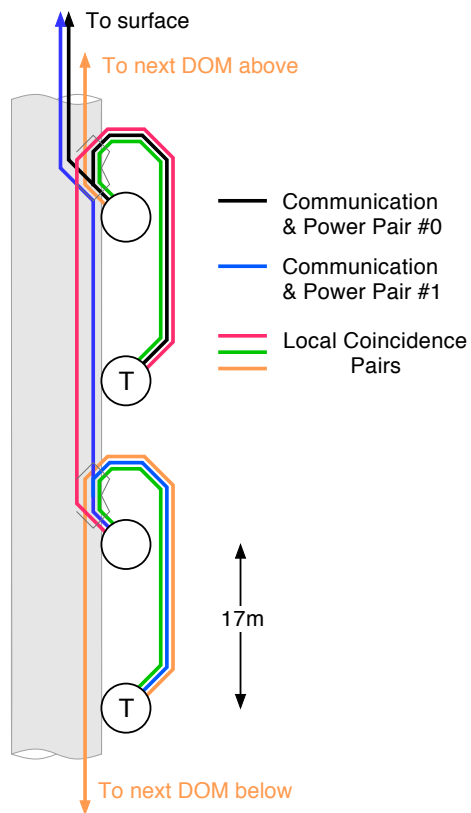
Fig. 9.4.: Schematic of cable connections for a set of four DOMs serviced by two wire pairs
from the surface that carry power and communications [121].

method is simple, but very robust due to the low noise environment of cables. The optimal functioning relies thus on extremely expensive cabling. The protocol is a custom packet-based scheme. Each packet is assigned a sequence number, and all received packets are acknowledged if the sequence number is correct. Each packet also contains a cyclic redundancy checksum to detect transmission errors. Out-of-sequence packets received are ignored, and non-acknowledged packets are retransmitted. The total bandwidth or number of transmitted bits per second of the communication channel is 720 kbps. The theoretical value is 1 Mbps, but we only realize 72% of the bandwidth efficiency because communications from the DOM can happen only when allowed by the DOR. When the DOR requests data from each DOM in turn, only one DOM per pair can transmit at a time, since the current protocol does not support multiple DOMs talking at the same time. The in-ice configuration has two DOMs per pair, while only one IceTop DOM per pair for increased bandwidth (IceTop hit rates can exceed 3 kHz). Communication is paused once per second to perform a timing calibration, dubbed Reciprocal Active Pulsing Calibration (RAPCal) Timing Protocol, used to synchronize clocks within approximately one ns.
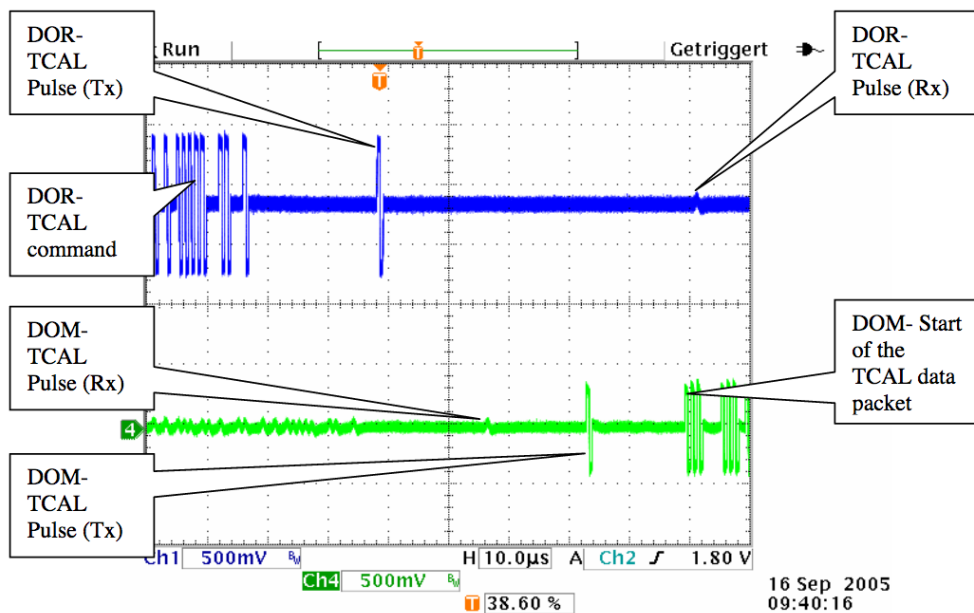
Fig. 9.5.: DOM Readout Interface (DOR)-DOM Time Calibration (TCAL) communications: example of bipolar pulses valid for bit 1 and quiet line valid for bit 0 [166]. Tx means transmitter and Rx means receiver. On Channel 1 in blue the DOR card, while on Channel 2 the DOM. The DOR card starts sending the TCAL communications on the left (DOR-TCAL Pulse (Tx) and DOR-TCAL command) towards the DOM. Immediately below, on Channel 2, the DOM receives these pulses (DOM-TCAL Pulse (Rx)), which, after having traveled through the cable, arrive distorted and reduced in amplitude. For the timing calibration procedure to work properly, the DOM has also to transmit to the surface, and this is seen on the right on Channel 2 (DOM-TCAL Pulse (Rx)). The bipolar pulse sent from the DOM is then received on the DOR side (DOR-TCAL Pulse (Rx)). The communication on the DOM side continues with the "Start of the TCAL command", but its reception from the DOR side is not shown.

Binary Phase Shift Keying Studies

10

While IceCube DOMs are diplexed on a copper pair, the design for the Gen2 facility envisions multiplexing of four or perhaps even eight DOMs per pair, to reduce the amount of down-hole cabling. The network topology remains however 1-to-N, with a single DOR-side communication endpoint talking to N DOM-side endpoints. An additional important characteristic of the system that was not exploited in the IceCube communication architecture is the very large asymmetry in the required bandwidth: the bulk of the bandwidth can be allocated to the direction of the PMT data towards the ICL storage, i.e. *uphole*, while the reverse direction traffic, i.e. *downhole*, is likely to consist of configuration messages and acknowledgments to received transmission. Although not essential, full-duplex communication, that is the transmission of data in both directions simultaneously, is a feature the next generation communication scheme should aim at. Alternatively, the current half-duplex configuration should increase the signaling rate.

Phase Shift Keying (PSK) is a popular technique used in digital data transmission systems, used for example for internet cable connections and for WiFi. The idea behind phase shift keying is very simple: at the transmitter side, a carrier (a sine wave for example) is modulated by the symbol stream, and the phase is modified every time the symbol changes. At the receiver side, the phase is recovered to retrieve the digital information. Binary PSK is the simplest technique, where one bit is one symbol. Most likely it is not the communication scheme the future upgrade will adopt, but sets the basis to study fancier techniques as Quadrature Amplitude Modulation, where the amplitude is modulated simultaneously on two different carriers in quadrature with each other, allowing immediately twice the transmission rate. A feasibility study on BPSK as modulation technique for the IceCube-Gen2 facility is presented here. A printed circuit board was built to simulate 3.5 km of the current IceCube cable, thus our medium. An Arbitrary Waveform Generator together with ArbeExpress, a software that generates waves that can then be uploaded into the wave generator, were used for the transmitter side. All the simulation work was carried out in Python.

Fig. 10.1.: Filter box.

Fig. 10.2.: Inside of a filter box. The same filter schematic is copied in two rows and eight columns, with the passive trough hole components clearly visible.

10.1 From Filter Box to Filter Board

In order to prove the feasibility of a communication method it is unavoidable to simulate the medium, that is the channel over which the communication is performed. In this case the channel is represented by an IceCube cable. It is given however that IceCube cables are very expensive, and having one in the laboratory only for testing purposes was unaffordable. This is why, already at the times when IceCube was under construction, several passive filters have been designed in order to simulate the behavior of a real IceCube cable but with low cost components such as resistors and capacitors. Several "Filter Boxes" have been constructed and one of them was at the laboratory at IIHE in Brussels. These filter boxes are currently being used at South Pole for the IceTop surface array. IceTop DOMs need an excess of roughly 1 km in order for time synchronization to work properly, otherwise if the cable is too short internal reflections prevent the procedure from working.
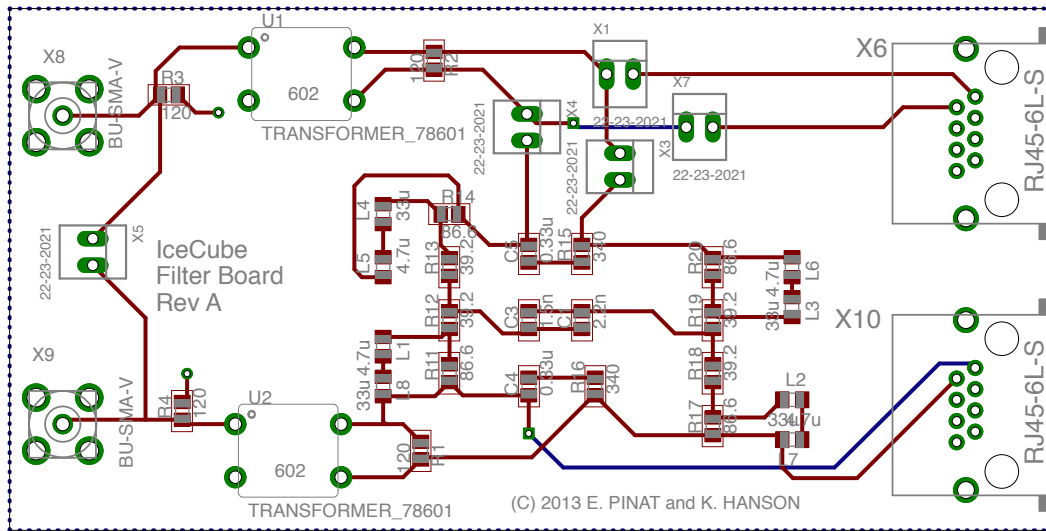
Fig. 10.3.: Final layout of the filter board.

The filter box is shown in Figure 10.1, and its inside in Figure 10.2. It contains 16 passive filters, that serve a total of 32 DOMs. As it might be evinced from the picture, the filter box is pretty big and not really convenient for testing purposes. Moreover, besides dimensions and weight, the connectors are designed to talk to the DOR system, and are not easy to use in the laboratory. Being driven by these reasons, starting from the filter design we decided to rearrange it and proceed designing the schematic and the layout of a two-layer printed circuit board. The layout is shown in Figure10.3, while Figure 10.4 is a picture of the final assembled board. This board was laid out with Eagle, fabricated by Eurocircuits and then assembled in the laboratory and served us as simulating device of 3.5 km IceCube cable, which is the longest distance a signal has to travel in case of real data communication. The simulated quantities have been the amplitude and phase distortions, while the time delay of the cable has not been taken into account.

10.1.1 Phase and amplitude measurements

By knowing the behavior of the phase and amplitude response of a filter as a function of the frequency, it is possible to move to the time domain by using the Fourier transform. One has therefore all the information needed to simulate the filter without the need of a real device. Amplitude and phase measurements have been performed, both with the filter box and the filter board. Also a simulation of the circuits has been performed using the LTSpice tool. Thanks to these measurements few problems have been noticed: due to the wrong grounding a phase inversion of 180° has to be taken into account and the presence of the transformers is responsible for and additional 8 dB amplitude decrease. In Figure 10.5 the two amplitude curves
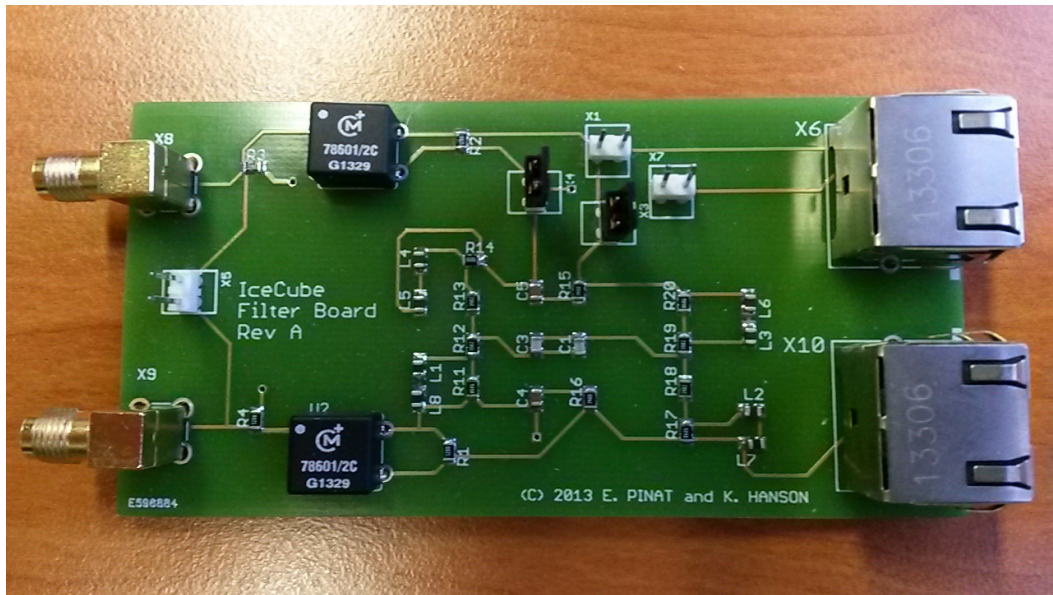
Fig. 10.4.: Filter board.

show the effect of the transformers, while the phase measurements have already been corrected for the wrong grounding.

10.2 Binary Phase Shift Keying (BPSK)

In this section the analysis steps are described. First of all an introduction about the modulation technique is given. Then the demodulation part and the sampling technique for recovering the information back is illustrated as well. Finally the Bit Error Rate (BER) is calculated.

The aim of this analysis is prove the feasibility of BPSK as modulation technique over 3.5 km of simulated IceCube cable for a signal with the following settings:

$$\text{carrier frequency } f_c = 1 \text{ MHz}$$
$$\text{modulating frequency } f_m = 50 \text{ kHz (100 kHz symbol rate)}$$
$$\text{sampling frequency } f_s = 20 \text{ MHz}$$
$$\text{Nyquist frequency } f_N = 10 \text{ MHz}$$

100 kHz symbol rate (100 kBaud) is compatible to the current signaling rate in IceCube, but not realistic with respect to the Gen2 facility for which a rate of at least 1 MBaud is required. This was however a good starting point for the study, and higher signaling rates have been considered at the end when discussing about error rates. The lower limit for the sampling frequency, being equal to 20 MHz in this part
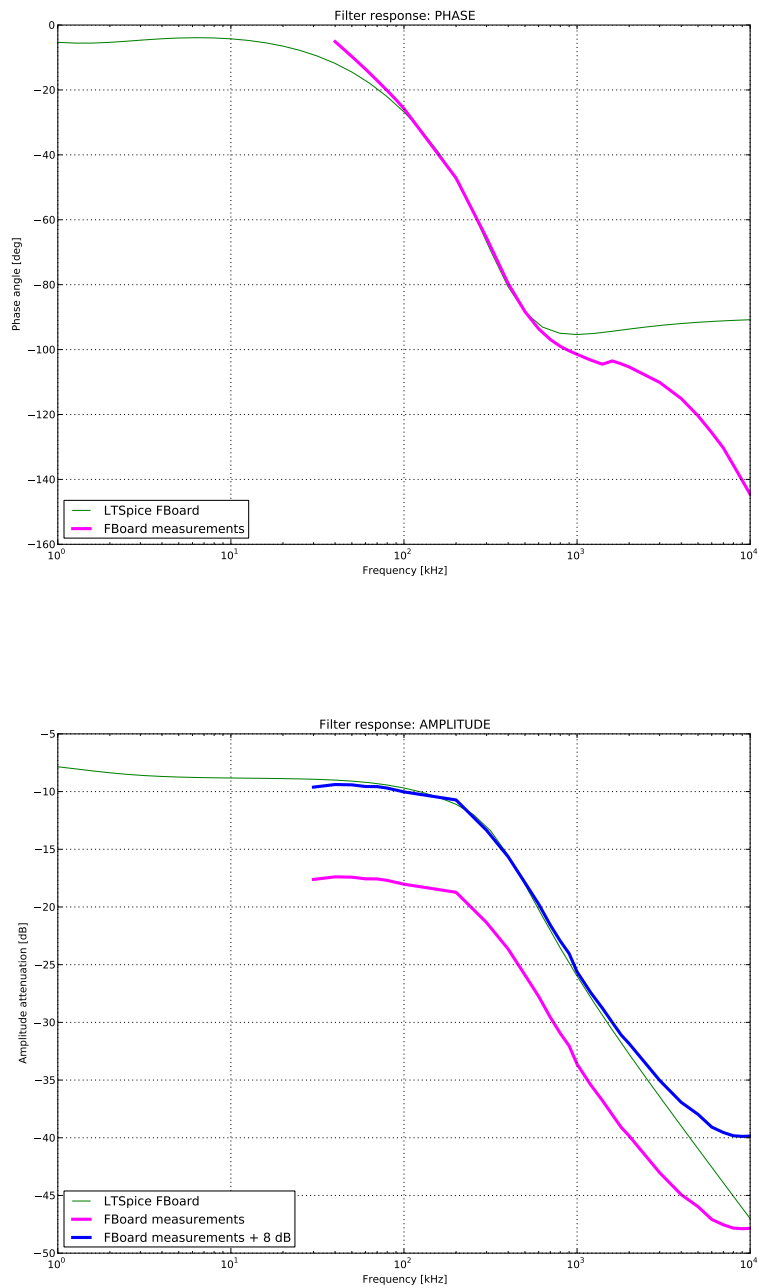
Fig. 10.5.: Phase and amplitude response for the filter board, compared to the simulated circuit in LTSpice.

of the study, is given by the sampling theorem, that states that a continuous signal can be properly sampled only if it does not contain components above one-half of the sampling rate. In this case, the minimal sampling frequency is 2 MHz, having a carrier at a 1 MHz frequency.

10.2.1 Instrumental set up

The instrumental set up was the following: the arbitrary waveform generator (AWG) was connected to the filter board via SMA connectors and LEMO cables. The output of the filter board was then sent to an oscilloscope. The scope is capable to store all the waveforms displayed on a .csv file, that was then used for the demodulation and bit recovery procedure with Python. The AWG is able to generate modulated waves up to a modulating frequency of 50 kHz, that is 100 kHz bit rate. To overcome this limitation, modulated waves of higher symbol frequency have been created first with Python and then converted in a usable format with Arbexpress software.

10.2.2 Modulation

Binary Phase Shift Keying is the simplest technique of digital modulation. In BPSK, the phase of a constant amplitude sinusoidal carrier $s(t)$ is switched between two values according to the two possibile messages to be sent, the binary values 0 and 1. In Figure 10.6 the working principle is shown. Here the carrier is a sine wave, but the cosine would work as well. The phase difference between the two states is $180°$. In this example the carrier wave is a sine wave of frequency f_c, whereas the modulating wave is a square wave of frequency f_m. The transmitted wave is the following:

$$s(t) = \begin{cases} \sin(2\pi f_c t) & \text{for bit } 1 \\ \sin(2\pi f_c t + \pi) & \text{for bit } 0 \end{cases} \tag{10.1}$$

Given the identity

$$\sin(2\pi f_c t + \pi) = -\sin(2\pi f_c t)$$

we can interpret the change in phase as a change in amplitude, and this trick is more helpful for understanding the BPSK constellation diagram, Figure 10.7. A BPSK signal can be represented as vectors on a polar plot, where the vector length corresponds to the signal amplitude and the direction correspond to the phase. Such a representation is referred to as the symbol constellation. The x-axis, I, represents the "in-phase" component of the waveform, that is in this example the sine part,
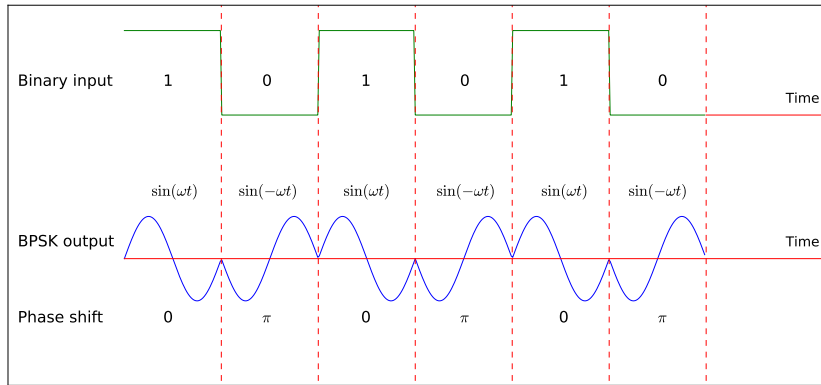
Fig. 10.6.: BPSK working principle.
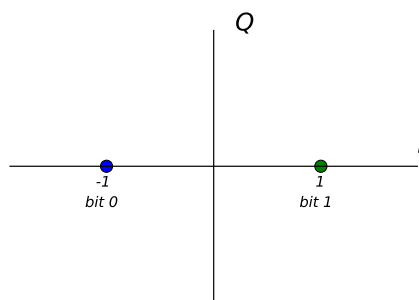
Fig. 10.7.: BPSK constellation diagram.
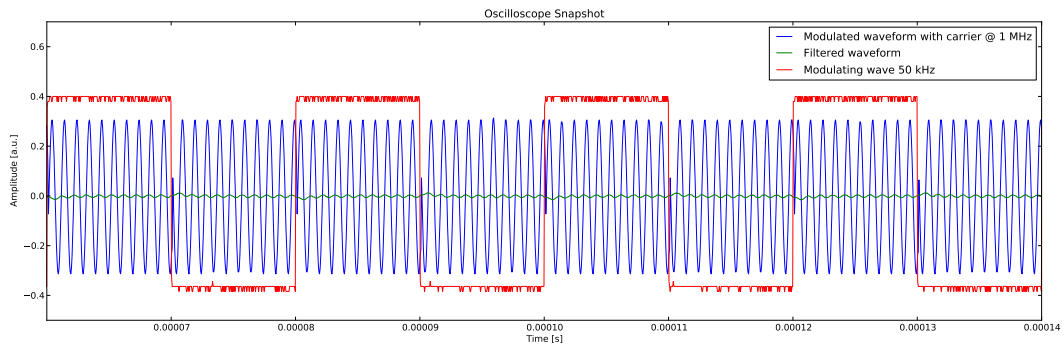
Fig. 10.8.: Oscilloscope data snapshot. Red represents the "information" signal - the modulating waveform; blue is the phase-modulated carrier, green is the filtered wave, i.e., after passing through 3.5 km of IceCube cable.

whereas the y-axis, Q, represents the "quadrature" component of the waveform, that is the cosine. In this diagram there is no component on the y-axis. The modulation frequency chosen is $f_m = 50$ kHz, and this corresponds to a signaling rate of 100 kbit (or kBaud, since one symbol is one bit), which is below the requested rate for IceCube communications (current rate: 1 Mbit - 1 MBaud). The signal coming from the AWG is both sent to the scope, blue wave in Figure 10.8, and also plugged into the filter board. The filtered signal is sent to the scope, green wave in Figure 10.8. For simplicity a simple clock wave has been considered as modulating waveform for this study, red curve in Figure 10.8, i.e. the bit stream is a series of binary numbers that looks like "......010101010101010101.....". Once all these waves are present on the scope it is possible to store their value on a csv file and transfer them for the analysis with an IPython notebook.

10.2.3 Demodulation and bit recovery

The signal that is coming out of the filter board needs to be demodulated in order to be able to recover the initial bit stream, ie. the information that had to be sent. The demodulation process can be mainly divided into two steps: the *beating* procedure and the filtering step. The *beating* procedure consists in multiplying the modulated waveform with a plain sine wave of the same frequency as the carrier, f_c. This procedure allows to separate two components of different frequencies, one of which is proportional to twice the carrier frequency. The simple trigonometric math is

showed in Equation 10.2. The modulation frequency f_m term, which governs the bit rate, is contained in the more generic $\phi(t)$ term.

$$
\begin{aligned}
\sin(2\pi f_c t + \phi(t)) \cdot \sin(2\pi f_c t) &= \\
&= [\sin(2\pi f_c t)\cos(\phi(t)) + \cos(2\pi f_c t)\sin(\phi(t))] \cdot \sin(2\pi f_c t) \\
&= \sin^2(2\pi f_c t)\cos(\phi(t)) + \cos(2\pi f_c t)\sin(2\pi f_c t)\sin(\phi(t)) \\
&= \left[\frac{1 - \cos(2\pi f_c t)}{2}\right]\cos(\phi(t)) + \frac{1}{2}\sin(2\pi f_c t)\sin(\phi(t)) \\
&= \frac{1}{2}\cos(\phi(t)) - \frac{1}{2}\cos(2\pi\, 2f_c\, t)\cos(\phi(t)) + \frac{1}{2}\sin(2\pi\, 2f_c\, t)\sin(\phi(t)).
\end{aligned}
\tag{10.2}
$$

After this multiplication step the signal is sent to a Low Pass Filter (LPF) that will remove the contributions of the second and third term in Equation 10.2. Figure 10.9 shows the result of the beating procedure.
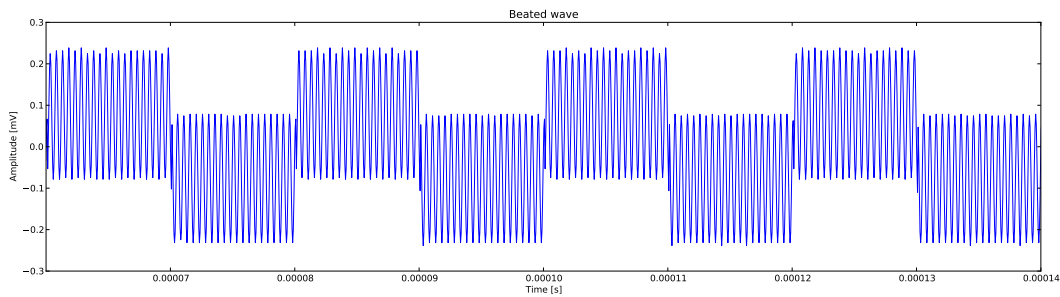
Fig. 10.9.: Beated wave.

After the beating, the LPF procedure is implemented on Python thanks to the signal processing part of *scipy.signal* package. The filter that has been used is a fourth order Butterworth low-pass filter.

As already mentioned, the carrier frequency used for this study has a frequency of 1 MHz and the modulation frequency is 50 kHz. The SciPy function needs as a second argument the cut-off frequency expressed in units of Nyquist frequency. The sampling frequency is 20 MHz, that corresponds to a Nyquist frequency of 10 MHz. Hence, having decided to cut at 200 kHz, this gives a value of 0.02 for the cut-off frequency term. In principle, assuming a perfect filter, given one frequency for the carrier, the modulated frequency could go up to roughly twice the carrier frequency and we will still be able to communicate. However the filter is not a perfect brickwall and there has to be enough separation between the modulation frequency and twice the carrier frequency in order to be able to maintain the communication liable (i.e. don not cut off the modulation) without using an extremely steep higher order filter. The final demodulated wave is represented in Figure 10.10.

The bit recovery procedure is performed by sampling the demodulated wave at the right point and compare the obtained value with a threshold one set accordingly
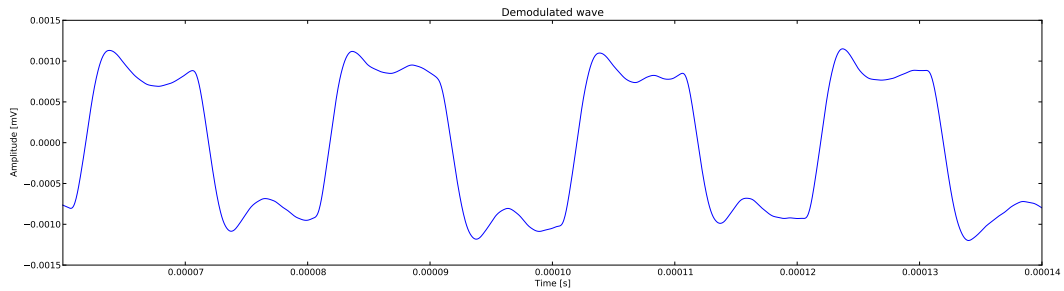
Fig. 10.10.: Demodulated wave ready for the bit recovery.

to the amplitude of the demodulated wave. In this study, the threshold value has been set to 0.0005 mV, and the amplitude of the wave in Figure 10.10 is just above this threshold. The downsampling frequency, that is the frequency at which the demodulated wave needs to be sampled to recovery the information, is given by the ratio between the sampling frequency (20 MHz) and the symbol rate (100 kHz). This is valid only for signals that are in phase with each other, therefore the downsampling procedure is very simple in the case of simulations, but needs a complex procedure of "hand shaking" and phase synchronization in a real communication between the DOR card and the DOM. In Figure 10.11 the downsampling point is shown as a green arrow on top of the demodulated wave (blue) and the original modulating one (red). The detection efficiency will be discussed in the following section discussing the Bit Error Rate.
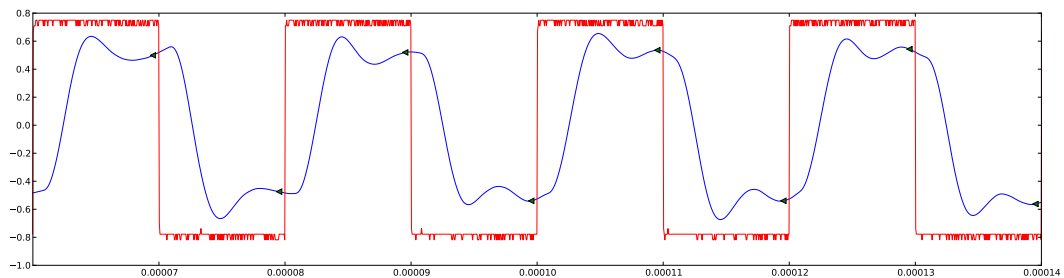
Fig. 10.11.: Downsampling for bit recovery.

10.2.4 Bit Error Rate

The Bit Error Rate (BER) represents the bit detection efficiency: it is the number of bits wrongly detected divided by total number of bits transmitted. Bit detection in this study is performed by a sampling process followed by a discrimination check: once the threshold is set (in our case 0.005 mV) the corresponding bit is determined according to the position of the waveform at the sample time. Provided the waveform is above the threshold, a bit is therefore detected. The presence of noise might however alter the waveform, and induce errors in the bit decoding process. In Figure 10.12 the BER is shown as a function of the Signal to Noise Ratio (SNR). Statistical errors on BER are binomial. If SNR > 1, values found are around

10^{-5}. They can be easily canceled with the proper Forward Error Correction code, but this topic will not be discussed here.
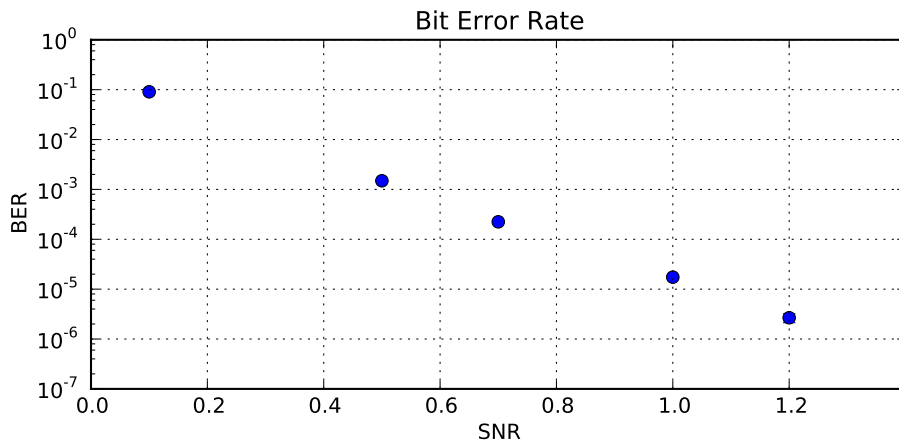
Fig. 10.12.: Bit Error Rate vs. Signal Noise Ratio.

An Additive white Gaussian noise (AWGN) has been considered in order to probe different SNR values.

10.3 Higher frequencies

As already mentioned, the symbol rate performance has initially been affected by the limitations of the waveform generator, that could not produce a BPSK modulated wave with a bit rate above 100 kHz. To overcome these difficulties and confirm the validity of the technique at higher frequencies (at least up to the required signal rate of 1 Mb/s) it has been decided to use the Arbexpress tool. After having generated the required waveform with Python, this software allows a conversion of the waveform data to the right format used by the waveform generator, which generates the signal accordingly. By playing this trick it has been possible to perform a modulation-filtering-demodulation-bit recovery process for carriers frequencies of 500 kHz, 1 MHz and 2.5 MHz. No formal BER measurements have been performed for these frequencies, but only a basic verification of the bit recovery. What has been tested is the recovery of a simple message of 10 bits. For these tests, the sampling frequency has been set to 2 GHz. The downsampling value in Table 10.1 is given by the ratio of the sampling frequency divided by the symbol rate. In Table 10.1 all the combinations considered are reported. For these combinations, despite no formal BER measurement, a simple test has been performed by checking the ability to successfully recover a string of bits.

f_c	f_m	Symbol rate	Cut off f	Downsampling
2 MHz	500 kHz	1 MBaud	1 MHz	2×10^3
2 MHz	1 MHz	2 MBaud	1 MHz	1×10^3
3 MHz	1 MHz	2 MBaud	1 MHz	1×10^3
4 MHz	2.5 MHz	5 MBaud	1 MHz	4×10^2
5 MHz	2.5 MHz	5 MBaud	1 MHz	4×10^2
6 MHz	2.5 MHz	5 MBaud	1 MHz	4×10^2
10 MHz	2.5 MHz	5 MBaud	1 MHz	4×10^2

Tab. 10.1.: Table listing all the various frequency combinations examined.

Summary of Part III

The IceCube Gen2 facility will need new hardware to be deployed in ice. Together with the optical modules, also the communication system must undergo a big change, and new communication techniques are under investigation. Binary Phase-shift Keying (BPSK) could be a valuable alternative to bipolar signaling. The study presented in the second part of this work aimed to prove the feasibility of Binary Phase Shift Keying as signaling method for the future IceCube Gen2 upgrade. After having manufacture a printed circuit board (PCB) to simulate 3.5 km of IceCube cable, namely the amplitude attenuation and phase distortion, the signal chain "modulation-transmission-recovery" has been performed for few signal rates, up to 5 Mb/s. The transmitted waveform, also called *carrier,* is a sine wave produced using a waveform generator, and is modulated according to a square wave which encodes the binary information: 1 is the high level, while 0 is the lower level. When the information is being encoded, at each bit change corresponds a phase change in the carrier of $180°$. This modulated wave is then transmitted through the PCB, undergoing amplitude and phase shifts corresponding to the effect of the cable. The outgoing signal however still carries the original information, that needs to be recovered following a specific procedure. The signal is first *beated*, then filtered and finally downsampled. These steps have been simulated using Python. For a specific signal configuration the bit error rate (BER) quantity has been calculated, representing the number of errors in the bit recovery as a function of the noise present in the system. The noise considered in our simulation has been simulated as well within Python, but in a real environment one must consider procedures to cope with it and control errors in data transmission. These topics however have not been treated, since we have limited ourselves to simulation.

Part IV

Conclusions and Outlook

Conclusions and Outlook

A search for extended sources has been performed using 7 years of through-going muons from May 2008 to May 2015, for a total of $713\,752$ events in 2426.2 days of livetime. Data have been taken with different detector configurations, from the 40-string layout to the final 86 completed one. This search is sensitive to TeV-PeV neutrino sources in the northern hemisphere, and to PeV-EeV sources in the southern hemisphere, due to an energy constraint imposed by the need to overcome the atmospheric muon background. Given the source extension is not known a priori, five extensions from $1°$ to $5°$ have been considered. A novel likelihood method has been implemented, that accounts and corrects for the signal contamination in the background obtained by scrambling technique. Five different significance skymaps have been produced, and a p-value has been calculated for the hottest spot of each map. All the five maps are consistent with the background-only hypothesis, as summarized in Table 10.2.

The sources of the high-energy astrophysical neutrinos and the high-energy cosmic rays remain an enigma. IceCube, running in a stable 86-string configuration since 2011, continues its efforts, constantly trying to improve background rejection and event reconstruction, and finding novel events selections to improve the detector sensitivity, especially in the southern sky. An in-depth exploration of the astrophysical

Extension [°]	RA [°]	DEC [°]	$\hat{n}_s$	$\hat{\gamma}$	p-value (pre-trial)	p-value (post-trial)
1°	249.32	63.28	73.32	1.85	8.20×10^{-7}	0.10
2°	169.44	27.04	102.92	2.19	9.04×10^{-6}	0.30
3°	169.37	27.68	119.18	2.16	7.31×10^{-5}	0.58
4°	229.82	-66.64	140.05	1.63	2.23×10^{-4}	0.78
5°	231.56	-66.44	160.83	1.68	1.99×10^{-4}	0.60

Tab. 10.2.: Summary of the results from the extended all-sky survey. The coordinates of the most significant spots located for each source extension hypothesis are given together with the respective p-values.

neutrino sector might however require a next-generation IceCube detector. Such a detector, named IceCube-Gen2, would deliver statistically significant samples of very high energy astrophysical neutrinos in the PeV-EeV range, and yield hundreds of neutrinos of all flavors at energies above 100 TeV within few years of operation. Precision measurements of the diffuse energy spectrum would benefit from cascades, while astrophysical neutrino sources could be finally identified using track-like signatures of muon neutrinos.

The IceCube-Gen2 facility will need new hardware to be deployed in ice. Together with the optical modules, also the communication system must undergo a big change, and new communication techniques are under investigation. The need to increase the number of detector channels per communication pair requires an overhaul of the existing communication system. In addition, improving the robustness of the communication system, increasing the time accuracy and reducing timing systematic offsets are among the technical goals to achieve. BPSK could be a valuable alternative to bipolar signaling. The study presented in the second part of this work aimed to prove the feasibility of Binary Phase Shift Keying as signaling method for the future IceCube Gen2 upgrade. The BPSK technique has been tested for a signal rate up to 5 Mbps. Event though the complete chain from modulation until Bit Error Rate evaluation has been performed only for a signal rate below the requested one, the simple bit recovery test was successfully tested also for higher frequencies. This technique has several advantages with respect to the current signaling method. Multiple DOMs are allowed to talk simultaneously, and if the I/Q modulation is considered (i.e. moving from BPSK to Quadrature Amplitude Modulation) it is possible to double the signaling using one carrier. As a final cosideration, time synchronization has not been discussed here, but the current procedure puts all the communications on hold once every second. BPSK would allow the use of the carrier for time synchronization purposes as well, without the need of a dedicated procedure.

Outlook

Since no significant clustering has been found, it is possible to set upper limits on muon neutrino and antineutrino fluxes for specific points in the Sky. However, the lack of neutrino flux predictions from extended sources does not allow us to constrain any model. Moreover, we do not see any benefit in setting upper limits on locations of the Sky that do not present any known source, as it is the case for the hotspots locations. The main improvement to this analysis would therefore be finding models of neutrino flux predictions from extended γ-ray sources, in order to constrain them or possibly rule out some scenarios. It would also be very interesting

to construct *a priori* a list of know extended γ-ray sources, choosing those few that have extensions greater than $1°$.

On the technical point of view, the unbinned maximum likelihood method applied to this extended source search is very computationally expensive. A significance skymap cannot be produced in one single operation, but, due to cluster timing constraints, has to be split in several declination bands, for a total of 70 hours processing time per map. Furthermore, the post-trial significance of each of the five results has to be calculated with respect to the distribution obtained from background scrambled maps, and this distribution requires roughly one week of computing resources for one single extension. With the addition of more years of IceCube data, and hoping to finally encounter a highly significant hotspot, the post-trial calculation would become more and more prohibitive, if not impracticable. Any future analyzer might therefore consider to move back to a binned method for computational reasons.

Appendix

Binning in $\sin(\delta)$ and energy for the spatial and energy PDFs for the IC86-II data sample in Figure 6.2.

- sinDec= [-1.,-0.983,-0.965,-0.948,-0.93,-0.867,-0.804,-0.741,-0.0678,-0.615, -0.552,-0.489,-0.426,-0.363,-0.3,-0.261,-0.222,-0.183,-0.144,-0.106,-0.067, -0.028,0.011,0.05,0.103,0.156,0.208,0.261,0.314,0.367,0.419,0.472,0.525,0.578, 0.631,0.683,0.736,0.789,0.842,0.894,0.947,1.]

- energy = [1.,1.113,1.227,1.34,1.453,1.567,1.68,1.793,1.907,2.02,2.133,2.247, 2.247,2.36,2.473,2.587,2.7,2.813,2.927,3.04,3.153,3.267,3.38,3.493,3.607,3.72, 3.833,3.947,4.06,4.173,4.287,4.4,4.513,4.627,4.74,4.853,4.967,5.08,5.193,5.307, 5.42,5.533,5.647,5.76,5.873,5.987,6.1,6.213,6.327,6.44,6.553,6.667,6.78,6.893, 7.007,7.12,7.233,7.347,7.46,7.573,7.687,7.8,7.913,8.027,8.14,8.253,8.367,8.48, 8.593,8.707,8.82,8.933,9.047,9.16,9.273,9.387,9.5]

Bibliography

[1] E. Pinat and K. Hanson. *Binary Phase Shift Keying Simulation Study*. IceCube Internal Report. Number 201411001. (2014) (cit. on p. 2).

[2] E. Pinat and K. Hanson. *DAQ and Trigger Issues: Capital and Furthermore releases*. IceCube Internal Report. Number 201310002. (2013) (cit. on p. 3).

[3] M. G. Aartsen et al. "Evidence for High-Energy Extraterrestrial Neutrinos at the Ice-Cube Detector". In: *Science* 342.6161 (2013). eprint: `http://science.sciencemag.org/content/342/6161/1242856.full.pdf` (cit. on p. 9).

[4] M. A. Markov and I. M. Zheleznykh. "On high energy neutrino physics in cosmic rays". In: *Nuclear Physics* 27.3 (1961), pp. 385 –394 (cit. on pp. 9, 10, 117).

[5] M. G. Aartsen et al. "IceCube-Gen2: A Vision for the Future of Neutrino Astronomy in Antarctica". In: *ArXiv e-prints* (2014). arXiv: `1412.5106` `[astro-ph.HE]` (cit. on pp. 9, 117, 119).

[6] F. Reines and C. L. Cowan. "The Neutrino". In: *Nature* 178 (1956), pp. 446–449 (cit. on p. 10).

[7] K. Greisen. "Cosmic Ray Showers". In: *Annual Review of Nuclear Science* 10.1 (1960), pp. 63–108. eprint: `https://doi.org/10.1146/annurev.ns.10.120160.000431` (cit. on p. 10).

[8] V. Aynutdinov et al. "The BAIKAL neutrino experiment: Physics results and perspectives". In: *Nuclear Instruments and Methods* A602 (2009), pp. 14–20. arXiv: `0811.1109` `[astro-ph]` (cit. on p. 11).

[9] M. Ageron et al. "ANTARES: The first undersea neutrino telescope". In: *Nuclear Instruments and Methods in Physics Research A* 656 (2011), pp. 11–38. arXiv: `1104.1607` `[astro-ph.IM]` (cit. on p. 11).

[10] ANTARES Collaboration. "A Deep Sea Telescope for High Energy Neutrinos". In: *ArXiv Astrophysics e-prints* (1999). eprint: `astro-ph/9907432` (cit. on p. 11).

[11] E. Migneco. "Status of the NEMO project". In: *Third NO-VE International Workshop on Neutrino Oscillations in Venice : Fifty years after the neutrino esperimental discovery : Venezia, February 7-10, 2006, Istituto Veneto di Scienze, Lettere ed Arti, Campo Santo Stefano*. (2006), pp. 489–504 (cit. on p. 11).

[12] G. Aggouras et al. "Recent results from NESTOR". In: *Nuclear Instruments and Methods in Physics Research Section A: Accelerators, Spectrometers, Detectors and Associated Equipment* 567.2 (2006), pp. 452 –456 (cit. on p. 11).

[13] P. Desiati and K. Bland. "Neutrino astronomy at the South Pole: status of the AMANDA experiment". In: *Results and perspectives in particle physics. Proceedings, 17th Rencontres de Physique de la Vallee d'Aoste, La Thuile, Italy, March 9-15, 2003*. 2003, pp. 45–62. arXiv: `astro-ph/0306536 [astro-ph]` (cit. on p. 12).

[14] B. P. Abbott et al. "Observation of Gravitational Waves from a Binary Black Hole Merger". In: *Physical Review Letters* 116 (2016), p. 061102 (cit. on p. 12).

[15] M. G. Aartsen et al. "The IceCube Realtime Alert System". In: *ArXiv e-prints* (2016). arXiv: `1612.06028 [astro-ph.HE]` (cit. on p. 13).

[16] M.W.E. Smith et al. "The Astrophysical Multimessenger Observatory Network (AMON)". In: *Astroparticle Physics* 45 (2013), pp. 56 –70 (cit. on p. 13).

[17] M. Bertolotti. *Celestial Messengers: Cosmic Rays The Story of a Scientific Adventure*. Astronomers' Universe. Springer, 2013 (cit. on p. 14).

[18] D. Fick and D. Hoffmann. "Werner Kolhörster (1887-1945): The German pioneer of cosmic ray physics". In: *Astroparticle Physics* 53 (2014). Centenary of cosmic ray discovery, pp. 50 –54 (cit. on p. 14).

[19] A. Letessier-Selvon and T. Stanev. "Ultrahigh energy cosmic rays". In: *Reviews of Modern Physics* 83 (2011), pp. 907–942 (cit. on pp. 15, 16).

[20] R. Sparvoli. "Direct measurements of cosmic rays". In: *Il Nuovo Cimento* (2008) (cit. on p. 14).

[21] M. Pohl. "AMS tracking in-orbit performance". In: *PoS* VERTEX2015 (2015), p. 22. arXiv: `1508.07759 [physics.ins-det]` (cit. on p. 14).

[22] O. Adriani et al. "The PAMELA Mission: Heralding a new era in precision cosmic ray physics". In: *Physics Reports* 544.4 (2014), pp. 323–370 (cit. on p. 14).

[23] A. Aab et al. "The Pierre Auger Cosmic Ray Observatory". In: *Nuclear Instruments and Methods* A798 (2015), pp. 172–213. arXiv: `1502.01323 [astro-ph.IM]` (cit. on p. 14).

[24] K. S. Cheng et al. "Proceedings of the XIV International Symposium on Very High Energy Cosmic Ray Interactions Telescope Array Experiment". In: *Nuclear Physics B - Proceedings Supplements* 175 (2008), pp. 221 –226 (cit. on p. 14).

[25] J. R. Hörandel et al. "The end of the galactic cosmic-ray energy spectrum - a phenomenological view". In: *Journal of Physics: Conference Series* 47.1 (2006), p. 132 (cit. on p. 16).

[26] E. G. Berezhko and H. J. Volk. "Kinetic theory of cosmic ray and gamma-ray production in supernova remnants expanding into wind bubbles". In: *Astronomy and Astrophysics* 357 (2000), p. 283. arXiv: `astro-ph/0002411 [astro-ph]` (cit. on p. 16).

[27] A. R. Bell et al. "Cosmic ray acceleration and escape from supernova remnants". In: *Monthly Notices of the RAS* 431 (2013), p. 415. arXiv: `1301.7264 [astro-ph.HE]` (cit. on p. 16).

[28] A. M. Hillas. "Can diffusive shock acceleration in supernova remnants account for high-energy galactic cosmic rays?" In: *Journal of Physics G: Nuclear and Particle Physics* 31.5 (2005), R95 (cit. on p. 16).

[29] J. R. Horandel. "Cosmic rays from the knee to the second knee: 10^4 to 10^{18} eV". In: *Modern Physics Letters* A22 (2007), pp. 1533–1552. arXiv: `astro-ph/0611387` `[astro-ph]` (cit. on p. 17).

[30] A. M. Hillas. "The cosmic-ray knee and ensuing spectrum seen as a consequence of Bell's self-magnetized SNR shock acceleration process". In: *Journal of Physics: Conference Series* 47.1 (2006), p. 168 (cit. on p. 17).

[31] I. Valino. "The flux of ultra-high energy cosmic rays after ten years of operation of the Pierre Auger Observatory". In: *PoS* ICRC2015 (2016), p. 271 (cit. on p. 17).

[32] R. U. Abbasi et al. "First observation of the Greisen-Zatsepin-Kuzmin suppression". In: *Physical Review Letters* 100 (2008), p. 101101. arXiv: `astro-ph/0703099` `[astro-ph]` (cit. on p. 17).

[33] T. Abu-Zayyad et al. "The Cosmic-Ray Energy Spectrum Observed with the Surface Detector of the Telescope Array Experiment". In: *The Astrophysical Journal, Letters* 768, L1 (2013). arXiv: `1205.5067` `[astro-ph.HE]` (cit. on p. 17).

[34] K. Greisen. "End to the Cosmic-Ray Spectrum?" In: *Physical Review Letters* 16 (1966), pp. 748–750 (cit. on p. 17).

[35] G. T. Zatsepin and V. A. Kuz'min. "Upper Limit of the Spectrum of Cosmic Rays". In: *Soviet Journal of Experimental and Theoretical Physics Letters* 4 (1966), p. 78 (cit. on p. 17).

[36] R. Aloisio et al. "Ultra High Energy Cosmic Rays: The disappointing model". In: *Astroparticle Physics* 34 (2011), pp. 620–626. arXiv: `0907.5194` `[astro-ph.HE]` (cit. on pp. 17, 18, 32).

[37] K. Kampert and P. Tinyakov. "Cosmic rays from the ankle to the cutoff". In: *Comptes Rendus Physique* 15 (2014), pp. 318–328. arXiv: `1405.0575` `[astro-ph.HE]` (cit. on pp. 17, 18).

[38] M. G. Aartsen et al. "Constraints on Ultrahigh-Energy Cosmic-Ray Sources from a Search for Neutrinos above 10 PeV with IceCube". In: *Physical Review Letters* 117.24 (2016), p. 241101. arXiv: `1607.05886` `[astro-ph.HE]` (cit. on p. 18).

[39] M. Bustamante et al. "High-energy cosmic-ray acceleration". In: *2009 Latin American School of High-Energy Physics*. CERN, 2010. eprint: `https://cds.cern.ch/record/1249755/files/p533.pdf` (cit. on p. 18).

[40] E. Fermi. "On the Origin of the Cosmic Radiation". In: *Physical Review* 75 (1949), pp. 1169–1174 (cit. on p. 18).

[41] A. M. Hillas. "The Origin of Ultra-High-Energy Cosmic Rays". In: *Annual Review of Astronomy and Astrophysics* 22 (1984), pp. 425–444 (cit. on p. 19).

[42] F. Halzen. "Multi-Messenger Astronomy:. Cosmic Rays, Gamma-Rays and Neutrinos". In: *Texas in Tuscany. XXI Symposium on Relativistic Astrophysics*. Ed. by R. Bandiera, R. Maiolino, and F. Mannucci. (2003), pp. 117–131. eprint: `astro-ph/0302489` (cit. on p. 20).

[43] J. A. Carpio and A. M. Gago. "Impact of Galactic magnetic field modeling on searches of point sources via ultrahigh energy cosmic ray-neutrino correlations". In: *Physical Review* D93.2 (2016), p. 023004. arXiv: `1507.02781` `[astro-ph.HE]` (cit. on p. 20).

[44] W. B. Atwood et al. "The Large Area Telescope on the Fermi Gamma-Ray Space Telescope Mission". In: *Astrophysical Journal* 697 (2009), pp. 1071–1102. arXiv: `0902.1089 [astro-ph.IM]` (cit. on p. 20).

[45] T. C. Weekes et al. "VERITAS: The Very energetic radiation imaging telescope array system". In: *Astroparticle Physics* 17 (2002), pp. 221–243. arXiv: `astro-ph/0108478 [astro-ph]` (cit. on p. 20).

[46] J. A. Hinton. "The Status of the H.E.S.S. project". In: *New Astronomy Reviews* 48 (2004), pp. 331–337. arXiv: `astro-ph/0403052 [astro-ph]` (cit. on p. 20).

[47] D. Petry et al. "The MAGIC Telescope - prospects for GRB research". In: *Astronomy and Astrophysics, Supplement* 138 (1999), pp. 601–602. eprint: `astro-ph/9904178` (cit. on p. 20).

[48] C. Merino. *Lectures on Particle Physics, Astrophysics and Cosmology*. Springer, (2015) (cit. on p. 21).

[49] M. Ackermann et al. "Detection of the Characteristic Pion-Decay Signature in Supernova Remnants". In: *Science* 339 (2013), pp. 807–811. arXiv: `1302.3307 [astro-ph.HE]` (cit. on pp. 21, 22, 24).

[50] P. Blasi. "The Origin of Galactic Cosmic Rays". In: *Astronomy and Astrophysics Review* 21 (2013), p. 70. arXiv: `1311.7346 [astro-ph.HE]` (cit. on p. 22).

[51] J. N. Bahcall and E. Waxman. "High-energy astrophysical neutrinos: The Upper bound is robust". In: *Physical Review* D64 (2001), p. 023002. arXiv: `hep-ph/9902383 [hep-ph]` (cit. on pp. 23, 31).

[52] F. W. Stecker. "Diffuse fluxes of cosmic high-energy neutrinos". In: *Astrophysical Journal* 228 (1979), pp. 919–927 (cit. on p. 23).

[53] J. K. Becker. "High-energy neutrinos in the context of multimessenger physics". In: *Physics Reports* 458 (2008), pp. 173–246. arXiv: `0710.1557 [astro-ph]` (cit. on p. 24).

[54] S. P. Wakely and D. Horan. "TeVCat: An online catalog for Very High Energy Gamma-Ray Astronomy". In: *International Cosmic Ray Conference* 3 (2008), pp. 1341–1344 (cit. on pp. 24, 31).

[55] J. Becker Tjus et al. "Gamma-ray emitting supernova remnants as the origin of Galactic cosmic rays?" In: *Astroparticle Physics* 81 (2016), pp. 1–11. arXiv: `1510.07801 [astro-ph.HE]` (cit. on p. 25).

[56] J. A. Hinton et al. "A New Era in Gamma-Ray Astronomy with the Cherenkov Telescope Array". In: *Astroparticle Physics* 43 (2013). Seeing the High-Energy Universe with the Cherenkov Telescope Array - The Science Explored with the {CTA}, pp. 1 –2 (cit. on p. 25).

[57] H. Abdalla et al. "H.E.S.S. observations of RX J1713.7-3946 with improved angular and spectral resolution; evidence for gamma-ray emission extending beyond the X-ray emitting shell". In: *ArXiv e-prints* (2016). arXiv: `1609.08671 [astro-ph.HE]` (cit. on p. 25).

[58] R. Enomoto et al. "The acceleration of cosmic-ray protons in the supernova remnant RX J1713.7-3946". In: *Nature* 416.6883 (2002), pp. 823–826 (cit. on p. 25).

[59] J. Alvarez-Muniz and F. Halzen. "Possible high-energy neutrinos from the cosmic accelerator RX J1713.7-3946". In: *Astrophysical Journal* 576 (2002), pp. L33–L36. arXiv: `astro-ph/0205408 [astro-ph]` (cit. on p. 25).

[60] I. Di Palma et al. "Revised predictions of neutrino fluxes from Pulsar Wind Nebulae". In: *Astrophysical Journal* 836.2 (2017), p. 159. arXiv: `1605.01205 [astro-ph.HE]` (cit. on p. 25).

[61] M. G. Aartsen et al. "All-sky Search for Time-integrated Neutrino Emission from Astrophysical Sources with 7 yr of IceCube Data". In: *The Astrophysical Journal* 835, 151 (2017), p. 151. arXiv: `1609.04981 [astro-ph.HE]` (cit. on pp. 25–27, 75, 77, 79, 103, 110, 111).

[62] A. Kappes et al. "Potential Neutrino Signals from Galactic Gamma-Ray Sources". In: *Astrophysical Journal* 656 (2007). [Erratum: Astrophysical Journal661,1348(2007)], pp. 870–896. arXiv: `astro-ph/0607286 [astro-ph]` (cit. on p. 26).

[63] S. Chaty. "Microquasars and jets". In: *Proceedings, 40th Rencontres de Moriond on Very High Energy Phenomena in the Universe: La Thuile, Italy, March 12-19, 2005*. 2005, pp. 321–328. arXiv: `astro-ph/0506008 [astro-ph]` (cit. on p. 26).

[64] F. Aharonian et al. "Discovery of very high energy gamma-rays associated with an x-ray binary". In: *Science* 309 (2005), pp. 746–749. arXiv: `astro-ph/0508298 [astro-ph]` (cit. on p. 26).

[65] D. F. Torres et al. "Neutrinos from Microquasars". In: *Chinese Journal of Astronomy and Astrophysics* 5.S1 (2005), p. 183 (cit. on p. 26).

[66] A. Levinson and E. Waxman. "Probing microquasars with TeV neutrinos". In: *Physical Review Letters* 87 (2001), p. 171101. arXiv: `hep-ph/0106102 [hep-ph]` (cit. on p. 26).

[67] F. Aharonian et al. "Microquasar LS 5039: A TeV gamma-ray emitter and a potential TeV neutrino source". In: *Journal of Physics Conference Series*. Ed. by A. Bottino, E. Coccia, J. Morales, and J. Puimedónv. Vol. 39. Journal of Physics Conference Series. (2006), pp. 408–415. eprint: `astro-ph/0508658` (cit. on p. 26).

[68] S. Adrián-Martínez et al. "A Search for Time Dependent Neutrino Emission from Microquasars with the ANTARES Telescope". In: *Journal of High Energy Astrophysics* 3-4 (2014), pp. 9–17. arXiv: `1402.1600 [astro-ph.HE]` (cit. on p. 26).

[69] C. Distefano et al. "Neutrino flux predictions for known galactic microquasars". In: *Astrophysical Journal* 575 (2002), pp. 378–383. arXiv: `astro-ph/0202200 [astro-ph]` (cit. on pp. 26, 27).

[70] L. A. Anchordoqui et al. "Estimating the contribution of Galactic sources to the diffuse neutrino flux". In: *Physical Review D* D90.12 (2014), p. 123010. arXiv: `1410.0348 [astro-ph.HE]` (cit. on p. 27).

[71] R. Genzel et al. "The Galactic Center massive black hole and nuclear star cluster". In: *Reviews of Modern Physics* 82 (2010), pp. 3121–3195. arXiv: `1006.0064` (cit. on p. 27).

[72] F. Aharonian et al. "Very high-energy gamma rays from the direction of Sagittarius A*". In: *Astronomy and Astrophysics* 425 (2004), pp. L13–L17. arXiv: `astro-ph/0408145 [astro-ph]` (cit. on p. 27).

[73] F. Aharonian et al. "Very high energy gamma rays from the composite SNR G0.9+0.1". In: *Astronomy and Astrophysics* 432 (2005), pp. L25–L29. arXiv: `astro-ph/0501265` `[astro-ph]` (cit. on p. 27).

[74] F. Aharonian et al. "Discovery of very-high-energy gamma-rays from the galactic centre ridge". In: *Nature* 439 (2006), pp. 695–698. arXiv: `astro-ph/0603021` `[astro-ph]` (cit. on p. 28).

[75] D. I. Jones et al. "The Milky Way Heart: Investigating molecular gas and gamma-ray morphologies in the Central Molecular Zone". In: *ArXiv e-prints* (2011). arXiv: `1104.0161` `[astro-ph.HE]` (cit. on p. 28).

[76] A. Abramowski et al. "Acceleration of petaelectronvolt protons in the Galactic Centre". In: *Nature* 531 (2016), p. 476. arXiv: `1603.07730` `[astro-ph.HE]` (cit. on p. 28).

[77] S. Celli et al. "Neutrinos and γ-rays from the Galactic Center Region after H.E.S.S. multi-TeV measurements". In: *European Physical Journal* C77.2 (2017), p. 66. arXiv: `1604.08791` `[astro-ph.HE]` (cit. on p. 28).

[78] M. Su et al. "Giant Gamma-ray Bubbles from Fermi-LAT: Active Galactic Nucleus Activity or Bipolar Galactic Wind?" In: *Astrophysical Journal* 724 (2010), pp. 1044–1082. arXiv: `1005.5480` `[astro-ph.HE]` (cit. on p. 29).

[79] T. Linden et al. "High-energy tail of the Galactic Center gamma-ray excess". In: *Physical Review* D94.10 (2016), p. 103013. arXiv: `1604.01026` `[astro-ph.HE]` (cit. on p. 29).

[80] J. Petrović et al. "Millisecond pulsars and the Galactic Center gamma-ray excess: the importance of luminosity function and secondary emission". In: *Journal of Cosmology and Astroparticle Physics* 1502.02 (2015), p. 023. arXiv: `1411.2980` `[astro-ph.HE]` (cit. on p. 29).

[81] R. Bartels et al. "Strong support for the millisecond pulsar origin of the Galactic center GeV excess". In: *Physical Review Letters* 116.5 (2016), p. 051102. arXiv: `1506.05104` `[astro-ph.HE]` (cit. on p. 29).

[82] M. G. Aartsen et al. "Observation of High-Energy Astrophysical Neutrinos in Three Years of IceCube Data". In: *Physical Review Letters* 113.10, 101101 (2014), p. 101101. arXiv: `1405.5303` `[astro-ph.HE]` (cit. on pp. 29, 30).

[83] M. G. Aartsen et al. "The IceCube Neutrino Observatory - Contributions to ICRC 2015 Part II: Atmospheric and Astrophysical Diffuse Neutrino Searches of All Flavors". In: *ArXiv e-prints* (2015). arXiv: `1510.05223` `[astro-ph.HE]` (cit. on p. 29).

[84] C. Lunardini et al. "Neutrino events at IceCube and the Fermi bubbles". In: *Proceedings, 59th Annual Conference of the South African Institute of Physics (SAIP2014): Johannesburg, South Africa, July 7-11, 2014*, pp. 347–353. arXiv: `1412.6240` `[astro-ph.HE]` (cit. on p. 29).

[85] D. Gruber et al. "The Fermi GBM Gamma-Ray Burst Spectral Catalog: Four Years Of Data". In: *Astrophysical Journal Suppl.* 211 (2014), p. 12. arXiv: `1401.5069` `[astro-ph.HE]` (cit. on p. 29).

[86] A. Aab et al. "Depth of maximum of air-shower profiles at the Pierre Auger Observatory. I. Measurements at energies above $10^{17.8}$ eV". In: *Physical Review* D90.12 (2014), p. 122005. arXiv: `1409.4809` `[astro-ph.HE]` (cit. on p. 30).

[87] A. Dar. "Neutrinos And Cosmic Rays From Gamma Ray Bursts". In: *ArXiv e-prints* (2012). arXiv: 1205.3479 [astro-ph.HE] (cit. on p. 30).

[88] A. Achterberg et al. "Search for Neutrino-induced Cascades from Gamma-Ray Bursts with AMANDA". In: *The Astrophysical Journal* 664.1 (2007), p. 397 (cit. on p. 30).

[89] M. G. Aartsen et al. "Search for Prompt Neutrino Emission from Gamma-Ray Bursts with IceCube". In: *The Astrophysical Journal* 805.1 (2015), p. L5. arXiv: 1412.6510 [astro-ph.HE] (cit. on p. 30).

[90] R. Abbasi et al. "An absence of neutrinos associated with cosmic-ray acceleration in γ-ray bursts". In: *Naure* 484 (2012), pp. 351–354. arXiv: 1204.4219 [astro-ph.HE] (cit. on p. 30).

[91] E. Presani. "Search for neutrinos from Gamma-Ray Bursts with ANTARES". In: *AIP Conference Procceedings* 1358 (2011), pp. 361–364. arXiv: 1104.4033 [astro-ph.HE] (cit. on p. 30).

[92] J. Schmid. "Search for High Energy GRB Neutrino Emission with ANTARES". In: *Proceedings, 48th Rencontres de Moriond on Very High Energy Phenomena in the Universe: La Thuile, Italy, March 9-16, 2013*. 2013, pp. 327–330. arXiv: 1311.4069 [astro-ph.HE] (cit. on p. 30).

[93] S. Adrián-Martínez et al. "Stacked search for time shifted high energy neutrinos from gamma ray bursts with the ANTARES neutrino telescope". In: *European Physical Journal* C77.1 (2017), p. 20. arXiv: 1608.08840 [astro-ph.HE] (cit. on p. 31).

[94] P. Padovani and E. Resconi. "Are both BL Lacs and pulsar wind nebulae the astrophysical counterparts of IceCube neutrino events?" In: *Monthly Notices of the RAS* 443.1 (2014), pp. 474–484. arXiv: 1406.0376 [astro-ph.HE] (cit. on p. 31).

[95] M. G. Aartsen et al. "The contribution of Fermi-2LAC blazars to the diffuse TeV-PeV neutrino flux". In: *The Astrophysical Journal* 835.1 (2017), p. 45. arXiv: 1611.03874 [astro-ph.HE] (cit. on p. 31).

[96] D. Elmegreen et al. "Smooth and Starburst Tidal Tails in the GEMS and GOODS Fields". In: *Astrophysical Journal* 663 (2007), pp. 734–751. arXiv: 0704.0911 [astro-ph] (cit. on p. 31).

[97] A. Loeb and E. Waxman. "The Cumulative background of high energy neutrinos from starburst galaxies". In: *Journal of Cosmology and Astroparticle Physics* 0605 (2006), p. 003. arXiv: astro-ph/0601695 [astro-ph] (cit. on p. 31).

[98] V. S. Beresinsky and G. T. Zatsepin. "Cosmic rays at ultra high energies (neutrino?)" In: *Physics Letters B* 28.6 (1969), pp. 423 –424 (cit. on p. 32).

[99] P. Allison et al. "Performance of two Askaryan Radio Array stations and first results in the search for ultrahigh energy neutrinos". In: *Physical Review D* D93.8 (2016), p. 082003. arXiv: 1507.08991 [astro-ph.HE] (cit. on pp. 32, 119).

[100] S. Carrigan et al. "The H.E.S.S. Galactic Plane Survey - maps, source catalog and source population". In: *Proceedings, 33rd International Cosmic Ray Conference (ICRC2013): Rio de Janeiro, Brazil, July 2-9, 2013*. 2013, p. 0741. arXiv: 1307.4690 [astro-ph.HE] (cit. on p. 32).

[101] A. Neronov and D. V. Semikoz. "Origin of TeV Galactic Cosmic Rays". In: *Physical Review* D85 (2012), p. 083008. arXiv: 1201.1660 [astro-ph.HE] (cit. on p. 32).

[102] A. A. Abdo et al. "TeV Gamma-Ray Sources from a Survey of the Galactic Plane with Milagro". In: *Astrophysical Journal* 664 (2007), pp. L91–L94. arXiv: `0705.0707` `[astro-ph]` (cit. on pp. 32, 33).

[103] A. A. Abdo et al. "Milagro Observations of Multi-TeV Emission from Galactic Sources in the Fermi Bright Source List". In: *Astrophysical Journall* 700 (2009), pp. L127–L131. arXiv: `0904.1018` `[astro-ph.HE]` (cit. on p. 33).

[104] B. M. Baughman and J. Wood. "TeV Gamma-Ray Emission Observed from Geminga with HAWC". In: *PoS* ICRC2015 (2015). arXiv: `1508.03497` `[astro-ph.HE]` (cit. on p. 33).

[105] A. Aab et al. "Searches for Anisotropies in the Arrival Directions of the Highest Energy Cosmic Rays Detected by the Pierre Auger Observatory". In: *Astrophysical Journal* 804.1 (2015), p. 15. arXiv: `1411.6111` `[astro-ph.HE]` (cit. on p. 34).

[106] R. U. Abbasi et al. "Indications of Intermediate-Scale Anisotropy of Cosmic Rays with Energy Greater Than 57 EeV in the Northern Sky Measured with the Surface Detector of the Telescope Array Experiment". In: *Astrophysical Journal* 790 (2014), p. L21. arXiv: `1404.5890` `[astro-ph.HE]` (cit. on pp. 34, 73).

[107] M. Brüggemann et al. "The Kascade-Grande experiment". In: *Neutrinos and Explosive Events in the Universe*. Dordrecht: Springer Netherlands, 2005, pp. 377–382 (cit. on p. 34).

[108] R. Gandhi et al. "Ultrahigh-energy neutrino interactions". In: *Astroparticle Physics* 5 (1996), pp. 81–110. arXiv: `hep-ph/9512364` `[hep-ph]` (cit. on pp. 35, 36).

[109] B. Voigt. "Sensitivity of the IceCube Detector for Ultra-High Energy Electron-Neutrino Events". PhD thesis. Humboldt-Universität zu Berlin, (2008) (cit. on p. 36).

[110] J. A. Formaggio and G. P. Zeller. "From eV to EeV: Neutrino Cross Sections Across Energy Scales". In: *Reviews of Modern Physics* 84 (2012), p. 1307. arXiv: `1305.7513` `[hep-ex]` (cit. on p. 37).

[111] I. Tamm. "Radiation emitted by uniformly moving electrons". In: *Journal of Physics (USSR)* 1 (1939), p. 439 (cit. on p. 39).

[112] D. Chirkin and W. Rhode. "Propagating leptons through matter with Muon Monte Carlo (MMC)". In: *ArXiv High Energy Physics - Phenomenology e-prints* (2004). eprint: `hep-ph/0407075` (cit. on pp. 40, 81).

[113] C. Kopper. "Performance Studies for the KM3NeT Neutrino Telescope". PhD thesis. Friedrich-Alexander-Universität Erlangen-Nürnberg, (2010) (cit. on pp. 41, 45).

[114] D. E. Groom et al. "Muon Stopping Power and Range Tables 10 MeV - 100 TeV". In: *Atomic Data and Nuclear Data Tables, Vol. 76, No. 2,* (2001) (cit. on p. 40).

[115] J. Feintzeig. "Searches for Point-like Sources of Astrophysical Neutrinos with the IceCube Neutrino Observatory". PhD thesis. University of Wisconsin, Madison, (2014) (cit. on pp. 45, 77).

[116] J. G. Learned and K. Mannheim. "HIGH-ENERGY NEUTRINO ASTROPHYSICS". In: *Annual Review of Nuclear and Particle Science* 50.1 (2000), pp. 679–749. eprint: `http://dx.doi.org/10.1146/annurev.nucl.50.1.679` (cit. on p. 44).

[117] R. Abbasi et al. "The Design and Performance of IceCube DeepCore". In: *Astroparticle Physics* 35 (2012), pp. 615–624. arXiv: `1109.6096` `[astro-ph.IM]` (cit. on p. 47).

[118] R. Abbasi et al. "IceTop: The surface component of IceCube. The IceCube Collaboration". In: *Nuclear Instruments and Methods in Physics Research A* 700 (2013), pp. 188–220. arXiv: `1207.6326` `[astro-ph.IM]` (cit. on p. 47).

[119] A. Achterberg et al. "First Year Performance of The IceCube Neutrino Telescope". In: *Astroparticle Physics* 26 (2006), pp. 155–173. arXiv: `astro-ph/0604450` `[astro-ph]` (cit. on p. 49).

[120] R. Abbasi et al. "Calibration and characterization of the IceCube photomultiplier tube". In: *Nuclear Instruments and Methods in Physics Research A* 618 (2010), pp. 139–152. arXiv: `1002.2442` `[astro-ph.IM]` (cit. on p. 49).

[121] M. G. Aartsen et al. "The IceCube Neutrino Observatory: instrumentation and online systems". In: *Journal of Instrumentation* 12 (2017), P03012. arXiv: `1612.05093` `[astro-ph.IM]` (cit. on pp. 49, 53, 58, 121, 123–125).

[122] M. G. Aartsen et al. "Measurement of South Pole ice transparency with the IceCube LED calibration system". In: *Nuclear Instruments and Methods* A711 (2013), pp. 73–89. arXiv: `1301.5361` `[astro-ph.IM]` (cit. on pp. 50–53, 63).

[123] G. Mie. "Beiträge zur Optik trüber Medien, speziell kolloidaler Metallösungen". In: *Annalen der Physik* 330 (1908), pp. 377–445 (cit. on p. 50).

[124] M. G. Aartsen et al. "The IceCube Neutrino Observatory Part VI: Ice Properties, Reconstruction and Future Developments". In: *Proceedings, 33rd International Cosmic Ray Conference (ICRC2013): Rio de Janeiro, Brazil, July 2-9, 2013*. 2013. arXiv: `1309.7010` `[astro-ph.HE]` (cit. on p. 51).

[125] P. B. Price. "Kinetics of conversion of air bubbles to air hydrate crystals in Antarctic ice". In: *Science* 267 (1995), p. 1802. arXiv: `astro-ph/9501073` `[astro-ph]` (cit. on p. 52).

[126] M. G. Aartsen et al. "South Pole glacial climate reconstruction from multi-borehole laser particulate stratigraphy". In: *Journal of Glaciology* 59 (2013), pp. 1117–1128 (cit. on p. 52).

[127] E. Andres et al. "Observation of high-energy neutrinos using Cherenkov detectors embedded deep in Antarctic ice". In: *Nature* 410 (2001), pp. 441–443 (cit. on p. 52).

[128] R. Abbasi et al. "The IceCube Data Acquisition System: Signal Capture, Digitization, and Timestamping". In: *Nuclear Instruments and Methods* A601 (2009), pp. 294–316. arXiv: `0810.4930` `[physics.ins-det]` (cit. on pp. 54, 55).

[129] J. L. Kelley and IceCube Collaboration. "Event triggering in the IceCube data acquisition system". In: *AIP Conference Proceedings* 1630.1 (2014), pp. 154–157. eprint: `http://aip.scitation.org/doi/pdf/10.1063/1.4902795` (cit. on pp. 57, 58).

[130] M. G. Aartsen et al. "Search for non-relativistic Magnetic Monopoles with IceCube". In: *European Physical Journal* C74.7 (2014), p. 2938. arXiv: `1402.3460` `[astro-ph.CO]` (cit. on p. 58).

[131] T. DeYoung. "IceTray: A software framework for IceCube". In: *Computing in high energy physics and nuclear physics. Proceedings, Conference, CHEP'04, Interlaken, Switzerland, September 27-October 1, 2004*. 2005, pp. 463–466 (cit. on p. 58).

[132] J. Ahrens et al. "Muon track reconstruction and data selection techniques in AMANDA". In: *Nuclear Instruments and Methods* A524 (2004), pp. 169–194. arXiv: `astro-ph/0407044` [astro-ph] (cit. on pp. 61, 62).

[133] M. G. Aartsen et al. "Improvement in fast particle track reconstruction with robust statistics". In: *Nuclear Instruments and Methods in Physics Research A* 736 (2014), pp. 143–149. arXiv: `1308.5501` [astro-ph.IM] (cit. on p. 61).

[134] M. Danninger. "Searches for Dark Matter with IceCube and DeepCore: New constraints on theories predicting dark matter particles". PhD thesis. Stockholm University, (2013) (cit. on p. 62).

[135] N. van Eijndhoven et al. "Implementation of a Gauss convoluted Pandel PDF for track reconstruction in Neutrino Telescopes". In: *Astroparticle Physics* 28 (2007), pp. 456–462. arXiv: `0704.1706` [astro-ph] (cit. on p. 62).

[136] D. Chirkin. "Photon tracking with GPUs in IceCube". In: *Nuclear Instruments and Methods* A725 (2013), pp. 141–143 (cit. on p. 63).

[137] N. Whitehorn et al. "Penalized Splines for Smooth Representation of High-dimensional Monte Carlo Datasets". In: *Computer Physics Communications* 184 (2013), pp. 2214–2220. arXiv: `1301.2184` [physics.data-an] (cit. on p. 63).

[138] K. Schatto. "Stacked searches for high-energy neutrinos from blazars with IceCube". PhD thesis. Johannes Gutenber Universit at Mainz, (2014) (cit. on pp. 63, 76, 77, 79).

[139] T. Neunhoffer. "Estimating the angular resolution of tracks in neutrino telescopes based on a likelihood analysis". In: *Astroparticle Physics* 25 (2006), pp. 220–225. arXiv: `astro-ph/0403367` [astro-ph] (cit. on pp. 63, 84).

[140] M. G. Aartsen et al. "Energy Reconstruction Methods in the IceCube Neutrino Telescope". In: *Journal of Instrumentation* 9 (2014), P03009. arXiv: `1311.4767` [physics.ins-det] (cit. on pp. 64, 90).

[141] U. F. Katz and C. Spiering. "High-Energy Neutrino Astrophysics: Status and Perspectives". In: *Progress in Particle and Nuclear Physics* 67 (2012), pp. 651–704. arXiv: `1111.0507` [astro-ph.HE] (cit. on p. 65).

[142] F. Aharonian. "HESS VHE Gamma-Ray Sources Without Identified Counterparts". In: *Astronomy and Astrophysics* 477 (2008), pp. 353–363. arXiv: `0712.1173` [astro-ph] (cit. on p. 73).

[143] D. Kang et al. "Search for gamma-ray point sources with KASCADE". In: *34th International Cosmic Ray Conference (ICRC2015)*. Vol. 34. International Cosmic Ray Conference. 2015, p. 812 (cit. on p. 73).

[144] R. Abbasi et al. "First Neutrino Point-Source Results from the 22 String Icecube Detector". In: *Astrophysical Journall* 701 (2009), pp. L47–L51. arXiv: `0905.2253` [astro-ph.HE] (cit. on p. 75).

[145] B. P. Roe et al. "Boosted decision trees, an alternative to artificial neural networks". In: *Nuclear Instruments and Methods* A543.2-3 (2005), pp. 577–584. arXiv: `physics/0408124` [physics] (cit. on p. 76).

[146] R. Abbasi et al. "Time-Integrated Searches for Point-like Sources of Neutrinos with the 40-String IceCube Detector". In: *Astrophysical Journal* 732 (2011), p. 18. arXiv: `1012.2137` [astro-ph.HE] (cit. on pp. 77, 79).

[147] M. G. Aartsen et al. "Search for Time-independent Neutrino Emission from Astrophysical Sources with 3 yr of IceCube Data". In: *Astrophysical Journal* 779 (2013), p. 132. arXiv: 1307.6669 [astro-ph.HE] (cit. on p. 77).

[148] R. others Abbasi. "Searches for High-energy Neutrino Emission in the Galaxy with the Combined ICECUBE-AMANDA Detector". In: *Astrophysical Journal* 763, 33 (2013), p. 33. arXiv: 1210.3273 [astro-ph.HE] (cit. on p. 79).

[149] R. Abbasi et al. "Neutrino Analysis of the 2010 September Crab Nebula Flare and Time-integrated Constraints on Neutrino Emission from the Crab Using IceCube". In: *Astrophysical Journal* 745, 45 (2012), p. 45. arXiv: 1106.3484 [astro-ph.HE] (cit. on p. 79).

[150] M. G. Aartsen et al. "Lowering IceCube's Energy Threshold for Point Source Searches in the Southern Sky". In: *Astrophysical Journal* 824, L28 (2016), p. L28. arXiv: 1605.00163 [astro-ph.HE] (cit. on p. 80).

[151] A. Ishihara and K. Hoshina. *Neutrino-generator*. Internal documentation (cit. on p. 80).

[152] A. Gazizov and M. P. Kowalski. "ANIS: High energy neutrino generator for neutrino telescopes". In: *Computer Physics Communications* 172 (2005), pp. 203–213. arXiv: astro-ph/0406439 [astro-ph] (cit. on p. 80).

[153] D. Heck et al. *CORSIKA: a Monte Carlo code to simulate extensive air showers.* (1998) (cit. on p. 81).

[154] J. Braun et al. "Methods for point source analysis in high energy neutrino telescopes". In: *Astroparticle Physics* 29 (2008), pp. 299–305. arXiv: 0801.1604 [astro-ph] (cit. on p. 83).

[155] J. Morales and J. Nocedal. "Remark on 'Algorithm 778: L-BFGS-B: Fortran Subroutines for Large-scale Bound Constrained Optimization'". In: *ACM Transactions on Mathematical Software* 38.1 (2011), 7:1–7:4 (cit. on p. 87).

[156] S. S. Wilks. "The Large-Sample Distribution of the Likelihood Ratio for Testing Composite Hypotheses". In: *The Annals of Mathematical Statistics* 9.1 (1938), pp. 60–62 (cit. on p. 92).

[157] M. G. Aartsen et al. "Search for Dark Matter Annihilation in the Galactic Center with IceCube-79". In: *European Physical Journal* C75.10 (2015), p. 492. arXiv: 1505.07259 [astro-ph.HE] (cit. on p. 94).

[158] M. G. Aartsen et al. "Searches for Extended and Point-like Neutrino Sources with Four Years of IceCube Data". In: *The Astrophysical Journal* 796, 109 (2014), p. 109. arXiv: 1406.6757 [astro-ph.HE] (cit. on p. 103).

[159] K. M. Górski et al. "HEALPix: A Framework for High-Resolution Discretization and Fast Analysis of Data Distributed on the Sphere". In: *The Astrophysical Journal* 622 (2005), pp. 759–771. eprint: astro-ph/0409513 (cit. on p. 104).

[160] F. Halzen and S. R. Klein. "Astronomy and astrophysics with neutrinos". In: *Physics today* 61.5 (2008), p. 29 (cit. on p. 117).

[161] K. Abe et al. "A Long Baseline Neutrino Oscillation Experiment Using J-PARC Neutrino Beam and Hyper-Kamiokande". In: *ArXiv e-prints* (2014). arXiv: 1412.4673 [physics.ins-det] (cit. on p. 118).

[162] The ICAL Collaboration et al. "Physics Potential of the ICAL detector at the India-based Neutrino Observatory (INO)". In: *ArXiv e-prints* (2015). arXiv: `1505.07380 [physics.ins-det]` (cit. on p. 118).

[163] M. Grassi. "JUNO: a General Purpose Experiment for Neutrino Physics". In: *ArXiv e-prints* (2016). arXiv: `1605.09118 [physics.ins-det]` (cit. on p. 118).

[164] X. Qian and P. Vogel. "Neutrino Mass Hierarchy". In: *Progress in Particle and Nuclear Physics* 83 (2015), pp. 1–30. arXiv: `1505.01891 [hep-ex]` (cit. on p. 118).

[165] S. Toscano. "Neutrino astronomy at the South Pole: Latest results from the IceCube neutrino observatory and its future development". In: *Nuclear Instruments and Methods in Physics Research Section A: Accelerators, Spectrometers, Detectors and Associated Equipment* (2017), pp. – (cit. on p. 120).

[166] K. H. Sulanke. *DOR-API Description*. Internal documentation. 2007 (cit. on p. 127).